Computational Modeling and Analysis of Electrophysiology and Hemodynamics During Atrial Fibrillation

Plappert, Felix

2025

Document Version:
Other version

Computational Modeling and Analysis of Electrophysiology and Hemodynamics During Atrial Fibrillation

Felix Plappert

LUND
UNIVERSITY

Doctoral Dissertation

by due permission of the Faculty of Engineering, Lund University, Sweden.

To be defended in E:1406, Ole Römers väg 3, Lund

April 8, 2025, at 9:00

Faculty opponent

Associate Professor Virginie Le Rolle

Organization: LUND UNIVERSITY Department of Biomedical Engineering P.O. Box 118, SE-221 00 Lund, Sweden	Document name: DOCTORAL DISSERTATION
	Date of issue: April 2025
	Sponsoring organization: Swedish Research Council (grant VR 2019–04272) Crafoord Foundation (grant 20200605)
Author: Felix Plappert	

Title and subtitle:
Computational Modeling and Analysis of Electrophysiology and Hemodynamics During Atrial Fibrillation

Abstract:

Atrial fibrillation (AF) is the most common arrhythmia globally and is characterized by uncoordinated atrial activation and ineffective atrial contraction. Atrial fibrillation is associated with an impaired quality of life and an increased risk of stroke, heart failure, and death. Changes in the autonomic nervous system (ANS) control of cardiac function are a known pathophysiological mechanism in AF, but methods for estimating autonomic activity during AF are lacking. Moreover, although AF is primarily an electrophysiological disease, its detrimental effects are mainly due to its hemodynamic consequences and are challenging to predict. Computational modeling offers a mechanistic framework that holds the potential to address both of these issues. Hence, this thesis aimed to (1) develop and use a computational model of the AV node to study patient-specific ANS modulation on AV nodal conduction properties during AF based on electrocardiogram (ECG) recordings and (2) develop and use a computational model to study patient-specific hemodynamics during AF based on ECG recordings and hemodynamic measurements. In addition, although f-wave characteristics derived from ECG are indicators of atrial remodeling, their prognostic value has not been explored in early-stage AF. The third aim of this thesis was to (3) study the prognostic value of f-wave characteristics in ECG recordings from implantable loop recorders at the earliest stages of AF.

To address the first aim, an AV node model from a previously published formulation was extended to incorporate ANS-induced changes in AV nodal refractoriness and conduction delay. *Paper I* demonstrated the necessity of accounting for ANS modulation of the AV node to accurately replicate observed changes in heart rate variability during tilt tests. The AV node model was further refined by incorporating respiration-induced autonomic modulation. The resulting model generated training data for a convolutional neural network (CNN) to estimate respiration-induced autonomic modulation of the AV nodal function from ECG data. *Paper II* showed that the developed CNN could effectively estimate respiration-induced autonomic modulation from ECG data, suggesting its potential for monitoring changes and detecting individual differences. However, further validation with ground-truth ANS data is required. The second aim was addressed by developing a computational model that combines an electrical subsystem, including the refined AV node model, with a mechanical subsystem describing cardiovascular mechanics to predict AF-induced hemodynamic changes. *Paper III* successfully replicated patient-specific arterial and intracardiac pressures using the integrated hemodynamic model, although discrepancies in right ventricular diastolic pressure indicated a need for further model refinement. The third aim was addressed by analyzing f-wave characteristics from ECG recordings of a large cohort of patients with early-stage AF to assess their prognostic value. *Paper IV* revealed that lower f-wave indices (atrial fibrillatory rate, organization index derived from the signal spectral characteristics, and average amplitude of the f-wave envelope) in early-stage AF have potential as prognostic markers for increased total and cardiovascular mortality in patients with AF episodes lasting ≥60 minutes.

In conclusion, the thesis presents several contributions to developing computational models and analytical methods for understanding and managing AF. The development of patient-specific models of AV nodal conduction and hemodynamics, combined with the investigation of prognostic f-wave characteristics, offers potential pathways toward more personalized and effective treatment strategies for AF.

Key words:
Atrial fibrillation, atrioventricular node, computational modeling, autonomic nervous system, RR series characteristics, f-wave characteristics

Classification system and/or index termes (if any):
–

Supplementary bibliographical information: –		Language English
ISSN and key title: –		ISBN 978–91–8104–345–7 (printed) 978–91–8104–346–4 (electronic)
Recipient's notes: –	Number of pages: 189	Price: –
	Security classification: –	

Public defence
April 8, 2025, at 9:00 in E:1406, E-building, LTH, Ole Römers väg 3, 223 63 Lund, Sweden.

Supervisors
Associate Professor Frida Sandberg
Dept. of Biomedical Engineering, Lund University, Lund, Sweden
Doctor Mikael Wallman
Dept. of Systems and Data Analysis, Fraunhofer-Chalmers Centre, Gothenburg, Sweden
Professor Pyotr G. Platonov
Dept. of Cardiology, Clinical Sciences, Lund University, Lund, Sweden

Faculty opponent
Associate Professor Virginie Le Rolle
Univ Rennes, Inserm, LTSI – UMR 1099, Rennes, France

Examination board
Associate Professor Silvia Muceli
Dept. of Electrical Engineering, Chalmers University of Technology, Gothenburg, Sweden
Associate Professor Kristian Soltesz
Dept. of Automatic Control, Lund University, Lund, Sweden
Dr. Kristian Solem
Principal Clinical Scientist, Stryker AB, Lund, Sweden
Deputy member: Professor Tomas Jansson
Dept. of Clinical Sciences, Biomedical Engineering, Lund University, Lund, Sweden

Chairman
Docent Christian Antfolk
Dept. of Biomedical Engineering, Lund University, Lund, Sweden

ISBN: 978–91–8104–345–7 (printed version)
ISBN: 978–91–8104–346–4 (electronic version)
Report No. 1/25
ISRN: LUTEDX/TEEM–1140–SE
Printed by Tryckeriet, E-building, Faculty of Engineering, Lund University, Lund, Sweden

Für Cornelia und Bernd Plappert.

Popular science summary

Atrial fibrillation (AF) is the most common rhythmical disorder that affects how our heart beats. The heart acts as a pump that usually beats in a regular rhythm. In atrial fibrillation, this rhythm becomes chaotic, like a drummer who suddenly starts beating wildly instead of keeping a steady beat. It is predicted that one in three Europeans will develop this heart condition during their lifetime. People with atrial fibrillation have a higher risk of stroke or death, more frequent hospital visits, and can experience a reduced quality of life.

For the heart to pump blood, an electrical stimulation has to initiate a contraction in the heart muscle. In a healthy heart, the electrical activity moves smoothly across the heart's chambers, causing them to contract in a coordinated way. Between heart beats, the electrical activity vanishes until the heart's intrinsic pacemaker starts a new electrical activation for the next heart beat. In atrial fibrillation, the electrical activity instead spreads in a chaotic and uncoordinated way over the upper chambers (called atria) and never vanishes, which reduces the atria's ability to push blood into the bottom chambers (called ventricles). Compared to a healthy heart rhythm, in atrial fibrillation the ventricles are activated at an increased and irregular rate which means the heart can't pump blood through the body as efficiently as it should.

The research presented in this thesis has been aimed to model and analyse the electrophysiology and hemodynamics during atrial fibrillation. First, computer models were created that simulate the electrical and mechanical function of the heart. These computer models were developed based on known physiological mechanisms that allow us to study complex behavior that would be impossible to observe directly. Second, clinical data from patients with atrial fibrillation were analyzed to uncover patterns in ECG recordings that could have prognostic value.

One key physiological mechanism involved the nervous system's role in atrial fibrillation. Our nervous system has two main parts: one that speeds up our heart

rate when we are active (like during exercise) and another that slows it down when we are relaxing. Sometimes, the balance between these two parts gets disrupted, which may trigger atrial fibrillation. By creating a mechanistic model of how the nervous system modulates the electrical conduction between atria and ventricles, we gained new insights into the role of the nervous system in atrial fibrillation.

Another key physiological mechanism involved the blood flow through the body during atrial fibrillation. A computer model the heart and circulation system was developed that can be customized to individual patients with atrial fibrillation. With this model, we can study how blood circulation is affected when the heart rate changes or when the heart rhythm becomes more regular or irregular.

This PhD thesis also includes a study on clinical data from a long-term study using implantable ECG recorders. These devices recorded episodes of atrial fibrillation during the early stages of atrial fibrillation involving patients who previously had no atrial fibrillation. By analysing these recordings, we have found that the analysis of these ECG recordings can help identify high-risk patients at the earliest stages of atrial fibrillation, potentially enabling more targeted interventions.

These discoveries are more than just scientific curiosities. They provide new tools for clinicians and researchers to understand atrial fibrillation better, potentially leading to more personalized treatment of atrial fibrillation. The human heart is incredibly complex, and conditions like atrial fibrillation remain challenging to manage and treat. But research in biomedical engineering can contribute to the understanding and treatment of this common rhythmical disorder.

Abstract

Atrial fibrillation (AF) is the most common arrhythmia globally and is characterized by uncoordinated atrial activation and ineffective atrial contraction. Atrial fibrillation is associated with an impaired quality of life and an increased risk of stroke, heart failure, and death. Changes in the autonomic nervous system (ANS) control of cardiac function are a known pathophysiological mechanism in AF, but methods for estimating autonomic activity during AF are lacking. Moreover, although AF is primarily an electrophysiological disease, its detrimental effects are mainly due to its hemodynamic consequences and are challenging to predict. Computational modeling offers a mechanistic framework that holds the potential to address both of these issues. Hence, this thesis aimed to (1) develop and use a computational model of the AV node to study patient-specific ANS modulation on AV nodal conduction properties during AF based on electrocardiogram (ECG) recordings and (2) develop and use a computational model to study patient-specific hemodynamics during AF based on ECG recordings and hemodynamic measurements. In addition, although f-wave characteristics derived from ECG are indicators of atrial remodeling, their prognostic value has not been explored in early-stage AF. The third aim of this thesis was to (3) study the prognostic value of f-wave characteristics in ECG recordings from implantable loop recorders at the earliest stages of AF.

To address the first aim, an AV node model from a previously published formulation was extended to incorporate ANS-induced changes in AV nodal refractoriness and conduction delay. *Paper I* demonstrated the necessity of accounting for ANS modulation of the AV node to accurately replicate observed changes in heart rate variability during tilt tests. The AV node model was further refined by incorporating respiration-induced autonomic modulation. The resulting model generated training data for a convolutional neural network (CNN) to estimate respiration-induced autonomic modulation of the AV nodal function from ECG data. *Paper II* showed that the developed CNN could effectively estimate respiration-induced autonomic

modulation from ECG data, suggesting its potential for monitoring changes and detecting individual differences. However, further validation with ground-truth ANS data is required. The second aim was addressed by developing a computational model that combines an electrical subsystem, including the refined AV node model, with a mechanical subsystem describing cardiovascular mechanics to predict AF-induced hemodynamic changes. *Paper III* successfully replicated patient-specific arterial and intracardiac pressures using the integrated hemodynamic model, although discrepancies in right ventricular diastolic pressure indicated a need for further model refinement. The third aim was addressed by analyzing f-wave characteristics from ECG recordings of a large cohort of patients with early-stage AF to assess their prognostic value. *Paper IV* revealed that lower f-wave indices (atrial fibrillatory rate, organization index derived from the signal spectral characteristics, and average amplitude of the f-wave envelope) in early-stage AF have potential as prognostic markers for increased total and cardiovascular mortality in patients with AF episodes lasting $\geq$60 minutes.

In conclusion, the thesis presents several contributions to developing computational models and analytical methods for understanding and managing AF. The development of patient-specific models of AV nodal conduction and hemodynamics, combined with the investigation of prognostic f-wave characteristics, offers potential pathways toward more personalized and effective treatment strategies for AF.

List of publications

Included papers

I. **An atrioventricular node model incorporating autonomic tone.**
Felix Plappert, Mikael Wallman, Mostafa Abdollahpur, Pyotr G Platonov, Sten Östenson, Frida Sandberg
Published in: Frontiers in Physiology, vol. 13, 976468, 2022

The author designed and evaluated the extended AV node model to account for autonomic nervous system-induced changes. The author performed the distribution-based sensitivity analysis and analyzed the influence of the AV node model parameters on RR series characteristics. The author processed the clinical data and matched the AV node model parameters to the clinical RR series characteristics. The author analyzed the results and wrote the manuscript.

II. **ECG-based estimation of respiration-induced autonomic modulation of AV nodal conduction during atrial fibrillation.**
Felix Plappert, Gunnar Engström, Pyotr G Platonov, Mikael Wallman, Frida Sandberg
Published in: Frontiers in Physiology, vol. 15, 1281343, 2024

The author extended the AV node model to account for respiration-induced autonomic modulation. The author processed the clinical data and developed a method for extracting ECG-derived respiration signals based on periodic component analysis. The author trained a 1-dimensional convolutional neural network with simulated RR series, respiration signal, and mean atrial arrival rate produced by the extended AV node model to estimate the magnitude of respiratory modulation from ECG recordings during atrial fibrillation. The author analyzed the results and wrote the manuscript.

III. A computational model to study hemodynamics during atrial fibrillation.
Felix Plappert, Pim JA Oomen, Clara E Jones, Emmanouil Charitakis, Lars O Karlsson, Pyotr G Platonov, Mikael Wallman, Frida Sandberg
Manuscript

The author developed a model composed of an electrical subsystem generating atrial and ventricular activation times characteristic for AF and a mechanical subsystem describing the cardiovascular mechanics to simulate hemodynamics during atrial fibrillation based on the AV node network model and the CircAdapt model. The author processed the clinical data and performed a patient-specific model fitting to replicate the clinical measurements. The author analyzed the results and wrote the manuscript.

IV. Prognostic value of ECG-derived f-wave characteristics from implantable LOOP recorder: Analysis from the LOOP study.
Felix Plappert*, Søren Zöga Diederichsen*, Claus Graff, Lucas Yixi Xing, Ketil Jørgen Haugan, Søren Højberg, Derk Krieger, Axel Brandes, Lars Køber, Fredrik Holmqvist, Mikael Wallman, Frida Sandberg, Jesper Hastrup Svendsen, Pyotr G Platonov
Manuscript
* Felix Plappert and Søren Zöga Diederichsen share first authorship

The author developed the data processing pipeline, which excludes and groups AF episodes based on their f-wave characteristics. The author performed the Cox regression and adjusted it for clinical risk factors to assess the association between f-wave indices and clinical endpoints. The author analyzed the results and wrote the manuscript.

Related work

The work has been presented at the following conferences.

I. Changes in RR Series Characteristics During Atrial Fibrillation: An AV Node Simulation Study.
Felix Plappert, Mikael Wallman, Pyotr G Platonov, Frida Sandberg
Presented at 48th Computing in Cardiology, Brno, Czech Republic, 2021.

II. Tilt-Induced Changes in RR Series Characteristics: An AV Node Simulation Study.
Felix Plappert, Mikael Wallman, Pyotr G Platonov, Sten Östenson, Frida Sandberg
Presented at 49th Computing in Cardiology, Tampere, Finland, 2022.

III. Estimating Respiratory Modulation in Atrial Fibrillation Using a Convolutional Neural Network
Felix Plappert, Mikael Wallman, Pyotr G Platonov, Frida Sandberg
Presented at 50th Computing in Cardiology, Atlanta, USA, 2023.

IV. Investigating the effect of RR series characteristics on hemodynamics
Felix Plappert*, Pim JA Oomen, Pyotr G Platonov, Mikael Wallman, Frida Sandberg
Presented at 49th International Congress on Electrocardiology, Lund, Sweden, 2024.
* Felix Plappert received the Poster Competition Award from the International Society of Electrocardiology

V. Hemodynamics in atrial fibrillation: An in-silico study
Felix Plappert, Pim JA Oomen, Pyotr G Platonov, Mikael Wallman, Frida Sandberg
Presented at Cardiac Physiome Workshop, Freiburg, Germany, 2024.

List of Abbreviations

1D 1-dimensional

AF atrial fibrillation

AFR atrial fibrillatory rate

ANS autonomic nervous system

AV atrioventricular

CN coupling node

CNN convolutional neural network

CT computed tomography

ECG electrocardiogram

FP fast pathway

HRV heart rate variability

ILR implantable loop recorder

MRI magnetic resonance imaging

NSR normal sinus rhythm

RR interval between consecutive ventricular activations

SA sinoatrial

SP slow pathway

TTE transthoracic echocardiography

Contents

Part I

Introduction

Chapter 1
Background and Aims

1.1 Background

Atrial fibrillation (AF) is the most common arrhythmia globally [1], with a prevalence in the United States alone expected to increase from 5.2 million in 2010 to 12.1 million by 2030 [2]. Atrial fibrillation is a supraventricular tachyarrhythmia with uncoordinated atrial activation and ineffective atrial contraction [1, 3] and is associated with impaired quality of life and an increased risk of stroke, heart failure, and death [1, 3]. Atrial fibrillation is recognized as a progressive disease that requires different strategies at different stages, from prevention to screening, to rate and rhythm control therapies [1].

The progressive nature of AF is attributed to the cardiac remodeling resulting from AF, which subsequently facilitates both the recurrence and the persistence of the arrhythmia [4]. An important pathophysiological mechanism contributing to AF is changes in the autonomic nervous system (ANS) control regulating the atrial electrophysiology [4]. The ANS is densely innervating the atrioventricular (AV) node [5], which is an anatomical structure within the cardiac conduction system with distinct electrophysiological properties [6]. The AV node is normally the only physiological path for electrical excitation propagation between atria and ventricles, providing a conduction pathway between the atria and the bundle of His [6]. In AF, when increased and irregular atrial activation enters the AV node, the filtering of electrical impulses through AV nodal conduction or blockage determines the ventricular rate and rhythm [7]. Hence, the AV node is an attractive indicator of autonomic function in AF. However, due to the unfeasibility of directly measuring electrical activity within the AV node, its function must be inferred from the relationship between atrial and ventricular activation times.

Although AF is an electrophysiological disease, its detrimental effects are mainly

due to its hemodynamic consequences. The heart functions as a pump, enabling blood circulation to and from all organs and tissues of the body. As the cardiac muscle contracts, triggered by electrical activity propagating over the cardiac tissue, the heart ejects blood into the cardiovascular system. Cardiac output, defined as the blood volume ejected per minute, is determined by the duration of heartbeats and the degree of coordinated contraction. A regular heart rhythm associated with normal sinus rhythm results in a higher cardiac output compared to an irregular heart rhythm characteristic of AF [8, 9, 10]. Understanding the effect of AF therapy on hemodynamics can guide treatment selection. However, predicting the hemodynamics for a sequence of irregular heartbeats is challenging, as the amount of blood ejected by the heart depends on the history of preceding heartbeats.

Biomedical signals originating from electrical, mechanical, or chemical sources contain a wealth of information about the cardiac rhythm and hemodynamics [11]. It is recommended that all AF patients undergo a 12-lead electrocardiogram (ECG) and transthoracic echocardiography (TTE) for diagnostic evaluation [3]. Although the ECG contains relevant information for the diagnostic assessment in AF, the presence of measurement noise and signal components from other interacting subsystems can obscure this information [11]. To address this issue, signal processing techniques can be used to extract interpretable data from these biomedical signals. For instance, f-waves and atrial fibrillatory rate (AFR) can be extracted from the ECG during AF and reveal information about the organization of atrial activity [12, 13]. As a second example, given that respiration is recognized to modulate parasympathetic activity and consequently affect cardiac rhythm, information about the respiration-induced autonomic modulation can be extracted from ECG data [14, 15]. Incorporating assumptions derived from a mechanistic understanding of cardiac physiology through model fitting may be essential for extracting information from biomedical signals. Computational modeling of cardiac physiology is a growing research field that combines mathematics, physics, experimental, and clinical data into a mechanistic framework with successful applications in risk prediction and personalized treatment of AF [16, 17]. These models can be fitted to individual patients using patient-specific data to provide diagnostic information and predict treatment outcomes [18, 19]. They are an essential tool for conducting virtual experiments, especially in scenarios where *in vivo* or *in vitro* studies are unethical or practically impossible [20].

1.2 Motivation and Aims

The work in this PhD thesis addresses the lack of non-invasive methods to determine the patient-specific cardiac ANS modulation during AF. Heart rate variability (HRV) analysis of ECG signals has been used in normal sinus rhythm (NSR) to extract

information about ANS modulation [21], but the HRV analysis is based on the ANS modulation of the sinoatrial (SA) node as primary pacemaker. In AF, the variations in the heart rate do not originate in the SA node but from the continuous uncoordinated atrial activity filtered by the AV node. Hence, new methods for analyzing the impact of autonomic modulation of the AV node during AF are needed.

Moreover, the work in this PhD thesis addresses the challenge of predicting the impact of the irregular heart rhythm in AF on patient-specific hemodynamics. Because the stroke volume depends on the history of previous heartbeats [22], the hemodynamics during an irregular rhythm cannot be accurately predicted from a single cardiac cycle but rather from an irregular series of many cardiac cycles. A computational model is suitable for predicting patient-specific hemodynamics in AF. However, there is a lack of computational models that could simulate the hemodynamics during AF fast enough to allow for personalized model calibration based on the hemodynamics of a series of irregular heartbeats. Thus, there is a need for fast computational models to study the impact of the atrial and ventricular rhythms on the hemodynamics during AF.

It was previously shown in the MUSIC study that a low AFR in patients with persistent AF and congestive heart failure was associated with poor outcomes, such as an increased risk of death [23]. The AFR represents the dominant frequency of the f-waves and is extracted from the ECG signal, and low AFR reflects more organized atrial activity and has been suggested to be linked to atrial remodeling. The recent LOOP study provides subcutaneous ECG recordings of automatically detected AF episodes in a large patient cohort at the earliest stages of AF, but the connection between f-wave characteristics at the earliest stages of AF and AF prognosis has not been studied.

Given this background, the specific aims of the thesis are the following:

Aim 1: To develop and use a computational model of the AV node to study patient-specific ANS modulation on AV nodal conduction properties during AF based on ECG recordings (*Paper I-II*).

Aim 2: To develop and use a computational model to study patient-specific hemodynamics during AF based on ECG recordings and hemodynamic measurements (*Paper III*).

Aim 3: To study the prognostic value of f-wave characteristics in ECG recordings from implantable loop recorders at the earliest stages of AF (*Paper IV*).

1.3 Thesis Outline

This thesis is structured into two parts, with Part I, titled *Introduction*, providing the essential theoretical framework and contextual background for the research presented in Part II, titled *Included Papers*. The chapters of Part I are structured as follows: Chapter 2 describes the cardiac anatomy and physiology at the tissue, organ, and organ system level and connects the fundamentals to typical ECG and hemodynamic measurements. Chapter 3 focuses on the diagnosis, mechanisms, and management of atrial fibrillation. Chapter 4 describes the analysis of clinical signals, covering methods for ECG analysis, as well as sensitivity analysis, an overview of neural networks, and survival analysis. Chapter 5 introduces cardiac computational modeling, providing a comprehensive review of current computational models of the AV node and an overview of computational hemodynamic models. Chapter 6 provides an overview of the four journal publications presented in Part II. Chapter 7 concludes the *Introduction* and highlights potential future research directions adding to this work.

Chapter 2

Cardiac Anatomy and Physiology

This chapter provides the anatomical and physiological foundations underlying the computational modeling and analysis of electrophysiology and hemodynamics during AF. The chapter begins with a description of cardiac anatomy and the cardiac conduction system at the organ level (Section 2.1). Sections 2.2 and 2.4 cover the cardiovascular system and autonomic nervous system, respectively. Section 2.3 describes cardiac tissue properties, focusing on the electrophysiological basis of regional variations in refractory periods and conduction delays. Given the central role of the AV node model in *Paper I–III*, Section 2.5 details its anatomical structure and dual-pathway physiology. Finally, Section 2.6 connects these anatomical and physiological fundamentals to the ECG and hemodynamic measurements used in subsequent chapters for the computational modeling and analysis of the cardiac function during AF.

2.1 The Heart

The heart is a hollow muscular organ that serves as a pump within the circulation system (Figure 2.1A). It comprises four chambers: two atria and two ventricles, arranged in left and right pairs. While the atria serve as primer pumps facilitating ventricular filling, the ventricles provide the main contractile force that propels blood through the circulation system (Figure 2.2). Unidirectional blood flow through the circulation system is maintained by two sets of heart valves: the A-V valves (i.e., the *tricuspid* and *mitral valves*) prevent backflow from ventricles to atria, while the semilunar valves (i.e., the *aortic* and *pulmonary artery valves*) prevent backflow from the *aorta* and *pulmonary arteries* to the ventricles. These heart valves open and close passively when a pressure

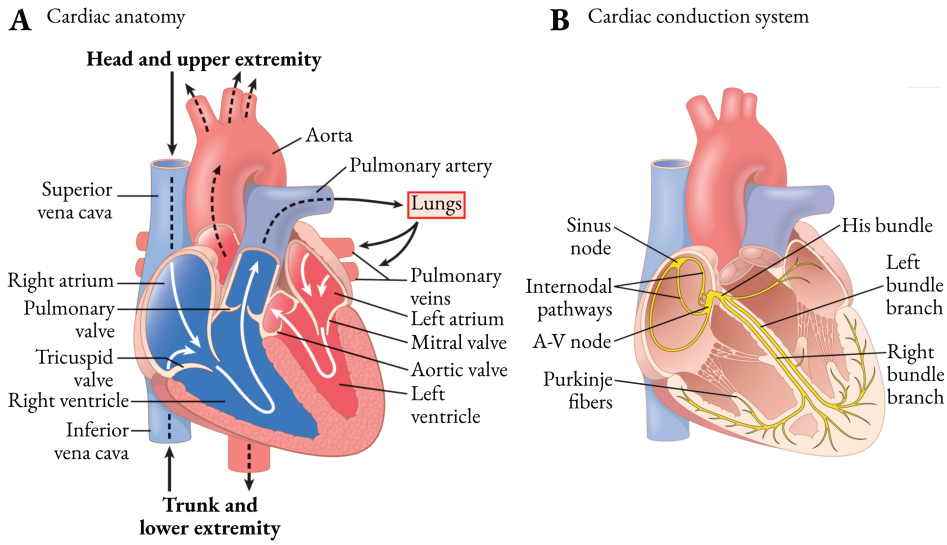

Figure 2.1: Illustration of **A)** the anatomy of the human heart with the four heart chambers, heart valves, and connecting arteries and veins and **B)** cardiac conduction system governing the electrical excitation propagation across the heart that results in the contraction of the myocardium. Modified from Hall and Hall [24] with permission from Elsevier.

gradient pushes blood forward or backward, respectively [24].

The cardiac conduction system governs the coordinated and rhythmical electrical excitation propagation and the resulting cardiac contraction (Figure 2.1B). The depolarization of the cardiac myocytes can trigger the depolarization of adjacent cells, thus promoting the propagation of electrical impulses across cardiac tissue, as described in more detail in Section 2.3. In NSR, a heartbeat is initiated by the self-excitation of the *sinus node*, which produces an electrical activation that propagates throughout the heart. Upon self-excitation of the *sinus node*, the electrical excitation propagates over the atria to the *AV node* and then via the *AV node*, *His bundle*, *bundle branches*, and *Purkinje fiber network* to the entire ventricular muscle mass. The *AV node* is normally the only electrical conduction pathway between atria and ventricles in healthy cardiac tissue (Figure 2.3). In NSR, the primary function of the *AV node* is to delay the electrical conduction between the atria and the ventricles to allow for the relocation of blood from the atria to the ventricles between their respective contractions. In AF, the *AV node* protects the ventricles from the high rate of electrical activation by enforcing a minimum duration between electrical activations [24].

2.2 The Cardiovascular System

The cardiovascular system is a closed circuit comprising the heart, *systemic circulation*, and *pulmonary circulation* (Figure 2.2). The cardiovascular system is responsible for blood circulation, transporting nutrients, oxygen, carbon dioxide, waste products, and hormones throughout the body. Deoxygenated blood arrives from the body via the systemic veins (i.e., *superior vena cava* and *inferior vena cava*) in the *right atrium*. The right heart, comprising the *right atrium* and *right ventricle*, pumps the blood into the *pulmonary circulation*, where it is oxygenated in the lungs. The oxygenated blood then arrives from the lungs via the pulmonary veins in the *left atrium*. The left heart, comprising the *left atrium* and *left ventricle*, pumps blood into the *systemic circulation* that connects to all parts of the body. The *arteries* have strong vascular walls that enable blood transport to the tissues under high pressure and at high blood velocity. The venous system returns the blood to the heart, has low blood pressure, and serves as a reservoir for extra blood that can contract or expand in response to the circulatory system's demands [24].

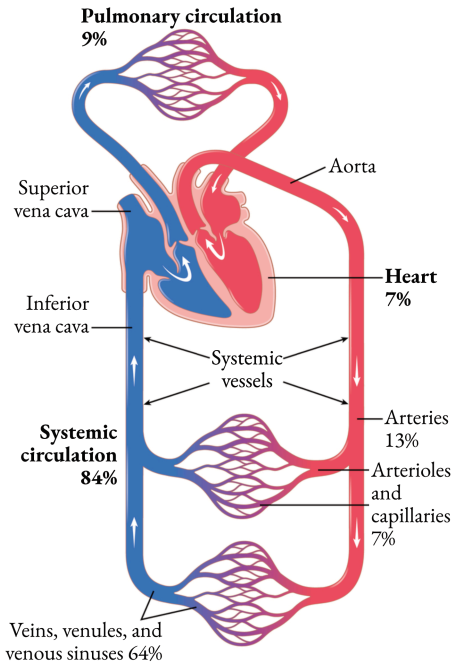

Figure 2.2: Illustration of the cardiovascular system comprising the heart, systemic circulation, and pulmonary circulation. Modified from Hall and Hall [24] with permission from Elsevier.

2.3 Cardiac Tissue

Cardiac tissue exhibits regional variations in its electrophysiological and mechanical properties that emerge from its structure on the molecular level and result in a coordinated cardiac activity on the organ level [25]. These functional differences across the heart are especially evident in the different electrical conduction velocities. Rapid conduction in the *Purkinje fibers* (2.3 m/s) facilitates near-simultaneous ventricular contraction. In contrast, slower conduction in the *AV node* (0.05 m/s)

ensures a delay between atrial and ventricular activation to allow for ventricular filling [26]. Between these extremes, the electrical excitation propagates through the atrial and ventricular myocardium at intermediate velocities: on average 0.6 m/s in the atria and 0.75 m/s in the ventricles [26]. The functional differences in the electrophysiology are also evident in the mechanical function. The *left ventricle* has a larger wall thickness (7.24±1.86 mm) than the *right ventricle* (3.4±0.8 mm), *left atrium* (2.4±0.7 mm), or *right atrium* (2.7±0.7 mm) [27, 28, 29]. The wall thickness of each chamber corresponds to the contractile force required to eject blood into the subsequent compartment, with thicker walls enabling greater contractile force.

Regional variations in electrophysiological and mechanical properties emerge from structural differences at the tissue, cellular, and molecular level [30, 31]. *Papers I–III* present a computational AV node network model that approximates tissue electrophysiology by incorporating conduction delay and refractory period parameters that are determined by the cardiac action potential. The action potential represents the change in membrane potential during cellular depolarization and repolarization, driven by transmembrane ion fluxes, primarily Na^+, K^+, and Ca^{2+}. Voltage-gated sodium channels facilitate a rapid depolarization at the start of the action potential, causing Na^+ influx that elevates membrane potential from approximately -90 mV to +20 mV. Conduction velocity and inverse proportional conduction delay are determined by several factors, including maximal upstroke velocity of action potentials, cell size, cell shape, and gap junction distribution [26, 25]. Following cellular depolarization, K^+ efflux reduces membrane voltage while Ca^{2+} influx increases it. The action potential enters a plateau phase when inward Ca^{2+} and outward K^+ currents are approximately in equilibrium. Subsequently, the cell returns to resting membrane potential through K^+ efflux and the redistribution of Na^+ and Ca^{2+} to the extracellular space and K^+ to the intracellular space [30]. The voltage-gated sodium channels, that facilitated the rapid depolarization at the start of the action potential, cycle through three states based on membrane potential: 1) closed–activated, 2) open–activated, and 3) closed–inactivated. These channels can only reactivate when membrane potential approaches its resting membrane potential [24]. Consequently, cells become temporarily unresponsive to electrical stimuli, known as the refractory period. The electrophysiological properties of cardiac tissue, such as action potential morphology, refractory period, and conduction delay, are history-dependent and vary dynamically depending on the time since the last activation [32].

2.4 The Autonomic Nervous System

The autonomic nervous system (ANS) represents the part of the nervous system that governs most visceral functions, including the regulation of heart rate and contractile

force to modulate cardiac output. The ANS comprises the sympathetic and parasympathetic nervous system. The sympathetic nervous system primarily controls physiological mechanisms that enhance energy expenditure and increase the heart rate. In contrast, the parasympathetic nervous system primarily decreases the heart rate and facilitates the restoration of energy supplies. Anatomically, the sympathetic and parasympathetic nervous systems innervate the organs via separate nerves. The parasympathetic nervous system originates in the brain stem and innervates the heart primarily via the vagus nerve. In contrast, the sympathetic nervous system is more extensively branched, with nerve fibers originating from multiple segments of the cervical and thoracic spinal cord [33]. Furthermore, the heart possesses an intrinsic nervous system that releases neurotransmitters associated with both sympathetic and parasympathetic signaling [34]. The anatomical landmarks of the cardiac conduction system – the *sinus node*, *AV node*, and *His bundle* (Figure 2.1B)– are more densely innervated by both sympathetic and parasympathetic efferent fibers than the working myocardium [34].

Signal transmission between the ANS and heart occurs through chemical neurotransmitters that bind to specific cardiac cell membrane receptors. The main sympathetic neurotransmitters, norepinephrine and epinephrine, interact with cardiac adrenergic receptors to increase AV nodal excitability and conduction velocity [35, 36, 37, 38] while decreasing action potential duration [37, 38]. During head-up tilt from a supine position, plasma concentrations of norepinephrine and epinephrine increase significantly [39]. Head-up tilt is associated with increased sympathetic tone, as evidenced by an increase in muscle sympathetic nerve activity and a corresponding decrease in both AV nodal conduction delay and refractory period [40, 39]. The impact of head-down tilt on sympathetic and parasympathetic activity is unclear. Conversely, the main parasympathetic neurotransmitter, acetylcholine, decreases atrial contractility, atrial effective refractory period, and ventricular contractile force [34]. In the *AV node*, parasympathetic activity increases both AV nodal conduction delay and refractory period [41]. Respiration is known to modulate the parasympathetic activity, with inspiration reducing vagal activity and expiration increasing it [42, 14]. The ANS utilizes multiple neurotransmitters and receptors beyond the main sympathetic and parasympathetic neurotransmitters outlined here. For a comprehensive overview into these neuromodulatory mechanisms, the reader is referred to [43, 34].

2.5 Atrioventricular Node

The *atrioventricular (AV) node* is a spindle-shaped network of cells located at the base of the *right atrium*. Specifically, the AV node is located at the apex of the *Triangle of Koch*, a region between the *coronary sinus ostium*, *tendon of Todaro*, and *tricuspid valve's* septal leaflet [6, 5] (Figure 2.3). The AV node is essential in the cardiac conduction

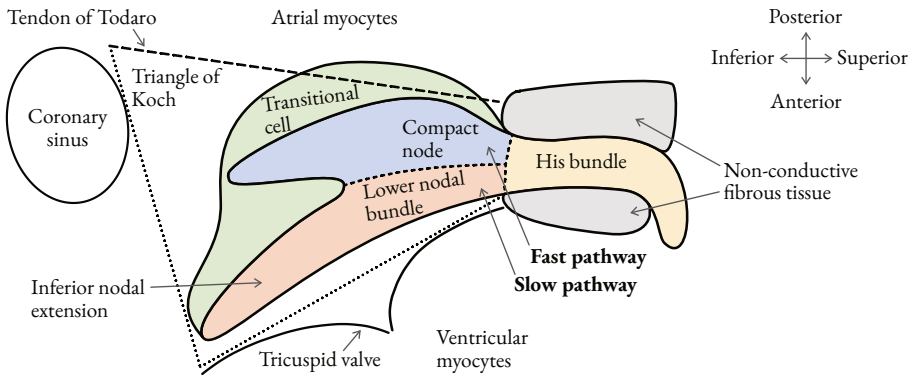

Figure 2.3: Anatomy of AV node with its two functional pathways. Illustration is based on the work of [6, 5].

system (Section 2.1), and its function during AF was modeled in *Paper I–III*. The AV node comprises two functional conduction pathways, known as the slow pathway (SP) and the fast pathway (FP). The FP is characterized by a shorter conduction delay and longer refractory period compared to the SP due to differences in the structure of cells [6]. The SP, comprising the *lower nodal bundle* and *inferior nodal extension*, extends along the *tricuspid valve* from the *coronary sinus* towards the *His bundle*. While less anatomically defined, the FP is allocated to the area of the compact node [6, 5].

2.6 Electrical Activity and Hemodynamic Variation in the Cardiac Cycle

This section connects the anatomical and physiological fundamentals described in Section 2.1–2.5 to typical ECG and hemodynamic measurements during a cardiac cycle in NSR. The ECG originates from the electrical activation propagation through the heart during each cardiac cycle. This generates a time-varying potential field outside the heart which can be measured at the body surface using electrodes, giving rise to the characteristic ECG signals. The cardiac cycle during NSR begins with the spontaneous self-excitation of the sinus node and subsequent atrial electrical activation (Section 2.1). The cardiac cycle comprises two phases: *systole*, representing the contraction phase, and *diastole*, representing the relaxation phase of the heart (Figure 2.4). Atrial depolarization is reflected in the ECG as the *P-wave* (Figure 2.5), triggering atrial systole and consequently increasing atrial pressure (*a-wave*) and ventricular volume (Figure 2.4). The *AV node* introduces a conduction delay between atrial and ventricular activation, evident in the *P–Q interval* on the ECG. Ventricular depolarization is

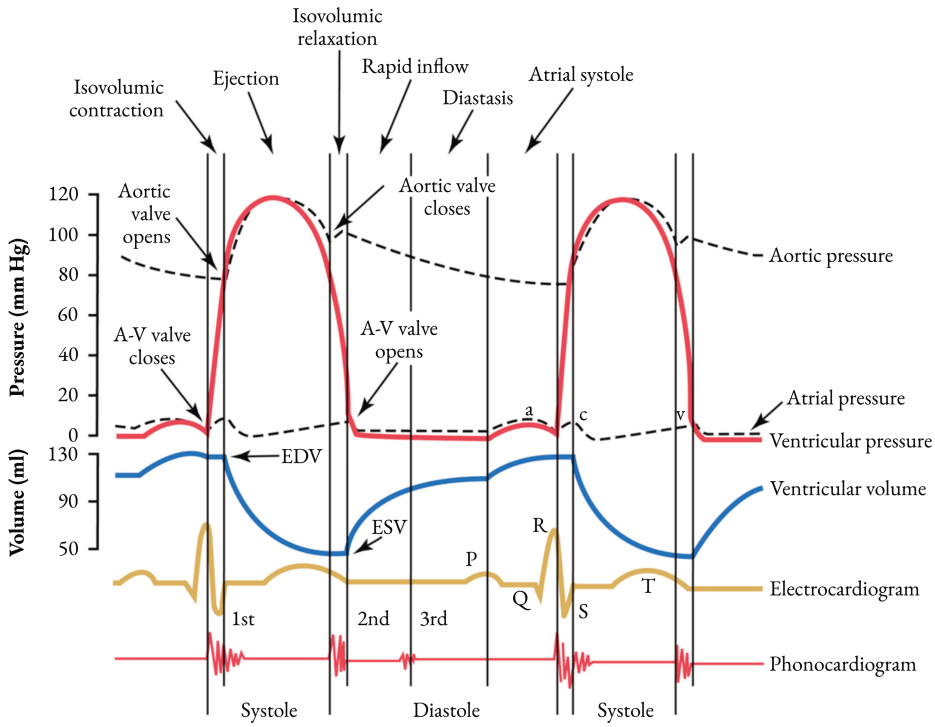

Figure 2.4: Illustration of the cardiac pressure and volume trends with an ECG and phonocardiogram signal over two cardiac cycles. Modified from Hall and Hall [24] with permission from Elsevier.

represented by the *QRS complex*, initiating ventricular contraction and a rapid rise in ventricular pressure. Once ventricular pressure exceeds atrial pressure, the A-V valves close, causing the *v-wave* in the atrial pressure signal. Subsequently, when ventricular pressure exceeds aortic pressure, the aortic valves open, resulting in ventricular ejection and a decrease in ventricular volume. Ventricular repolarization, following the action potential plateau (Section 2.3), is observed as the *T-wave* on the ECG. As the ventricles relax and ventricular pressure falls below aortic and atrial pressures, the aortic valves close, and the A-V valves open. During ventricular diastole, atrial filling causes a slow rise in atrial pressure (*v-wave*) until the A-V valves open and blood flows into the ventricles, increasing ventricular volume. Systolic pressure and volume refer to the maximum pressure and minimum volume, respectively, during systole. Conversely, diastolic pressure and volume represent the minimum pressure and maximum volume during diastole. Ventricular ejection fraction is a common index for assessing cardiac

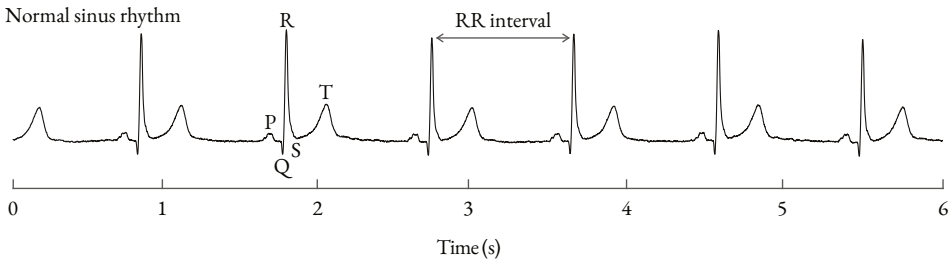

Figure 2.5: Typical ECG signal in normal sinus rhythm. Adapted from Sörnmo [44] with permission from Springer Nature.

pumping function and is defined as in Eq. 2.1,

$$EF_{ventricle}(\%) = \frac{EDV - ESV}{EDV} \cdot 100, \tag{2.1}$$

where EDV represents the end-diastolic volume at the aortic valve opening, and ESV denotes the end-systolic volume at the A-V valve opening (Figure 2.4). Because there are no valves between the veins and the atria, the atrial ejection fraction is calculated using the atrial diastolic and systolic volumes instead of the end-diastolic and end-systolic volumes. The cardiac output defines the amount of blood pumped each minute.

Chapter 3
Atrial Fibrillation

This chapter focuses on the diagnosis, mechanisms, and management of atrial fibrillation (AF), providing an overview of the underlying pathology that prompted the development of new techniques in this thesis. First, Section 3.1 describes the characteristic electrical activity of AF in the ECG that differentiates AF from normal sinus rhythm (NSR) and gives evidence for its diagnosis. Atrial fibrillation has a progressive nature and is promoted by several pathophysiological mechanisms [4]. These mechanisms can result from cardiac disease but also from the consequences of AF itself. Because the ECG measures the cardiac electrical activity, it may contain information about the AF progression and the underlying mechanisms, given the methods to extract this information exist. Section 3.2 describes the main mechanisms behind AF. Based on these mechanisms behind AF, computational models with a mechanistic description of AF were developed in *Paper I–III* to predict patient-specific autonomic modulation and hemodynamic response in AF. Finally, Section 3.3 addresses the management of AF, emphasizing that personalized treatment approaches must recognize patient-specific differences and that different strategies are required at different stages.

3.1 Atrial Fibrillation in the ECG

Atrial fibrillation is a supraventricular tachyarrhythmia with uncoordinated atrial activation and ineffective atrial contraction [1, 3]. Atrial fibrillation is a rhythm disorder that alters the electrical activity in the atria and ventricles. In Section 2.1 and 2.6, the electrical excitation propagation in the heart and the resulting ECG signal morphology was described for healthy NSR. In NSR, the electrical excitation is initiated in the SA node and spreads throughout the atria. In the ECG, the atrial depolarization phase is represented by the *P-wave*, the atrial repolarization phase is

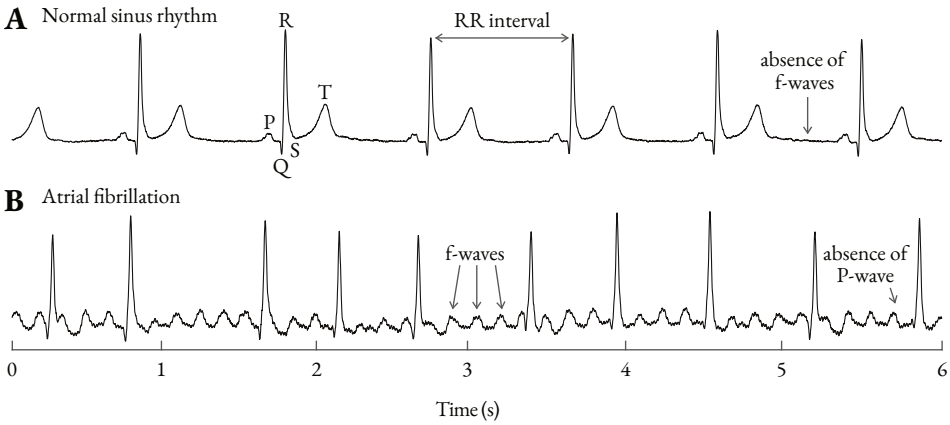

Figure 3.1: ECG signal in normal sinus rhythm and atrial fibrillation. **A**) In NSR, the *P-wave* represents the atrial depolarization, the *QRS complex* represents the ventricular depolarization, and the *T-wave* represents the ventricular repolarization. The period between heartbeats is characterized by the RR interval between two *R waves*. Ventricular activations occur at a regular rhythm. **B**) In AF, the *f-waves* represent the atrial activity and are superimposed on the *QRS complex* and *T-wave* representing the ventricular activity. Ventricular activations occur at an irregular rhythm. Adapted from Sörnmo [44] with permission from Springer Nature.

concealed by the *QRS complex*, and the remaining ECG is not affected by the atrial electrical activity (Figure 3.1A). In AF, the electrical excitation does not terminate between heartbeats but propagates continuously over the atrial tissue. Thus, the atrial activity is not governed by the SA node, and the atria contract irregularly at rates of 400 to 600 beats per minute [45]. In the ECG, the *P-wave* is absent in AF and is replaced by *f-waves* present throughout the ECG signal reflecting the continuous atrial electrical activity (Figure 3.1B). The f-waves, their fundamental frequency, and the f-wave frequency spectrum overall contain information about the disorganization of atrial electrical activity and were studied in *Paper IV*.

In NSR, every atrial activation is succeeded by a ventricular activation after being delayed by the AV node. In the ECG, the ventricular depolarization phase is represented by the *QRS complex* and the ventricular repolarization phase is represented by the *T-wave* (Figure 3.1A). The period between heartbeats is characterized by the RR interval between two *R waves*. The typical resting heart rate for individuals in NSR ranges from 60 to 80 beats per minute [45]. In AF with rapid atrial activation of 400 to 600 beats per minute, the AV node is blocking part of the rapid and irregular incoming atrial activations, resulting in a ventricular rate ranging from 110 to 180 beats per minute, which is an increased heart rate and more irregular heart rhythm compared to NSR (Figure 3.1B) [45].

The ECG is the gold standard, and ECG documentation is required for the diagnosis of AF [3]. A 12-lead ECG or ≥30 s single-lead ECG displaying irregular RR intervals and absent P waves indicate clinical AF, with diagnosis confirmed upon the physician's review of the ECG signal [3]. As described in Section 4, ECG signals were processed in all of the *Papers I-IV* to extract patient-specific measures of atrial and ventricular electrical activity.

3.2 Mechanisms behind Atrial Fibrillation

Atrial fibrillation arises from a complex interplay of four pathophysiological mechanisms that contribute to its development and maintenance: electrical remodeling, structural remodeling, autonomic nervous system changes, and calcium handling abnormalities [46, 4, 47]. Electrical remodeling primarily involves a reduction in L-type Ca^{2+} current, an up-regulation of rectifier background K^+ current, an enhanced constitutive acetylcholine-regulated K^+ current, and modified gap junction functionality [4, 47]. The electrical remodeling promotes re-entry by shortening action potential duration, hyperpolarizing atrial cardiomyocytes, and removing voltage-dependent sodium current inactivation (Section 2.3) [48, 4, 47]. Structural remodeling includes atrial enlargement, which increases available tissue mass, as well as tissue fibrosis, which creates areas of slow conduction and functional block [4, 47]. These electrical and structural remodeling mechanisms, which create a substrate prone to reentry, can be further promoted by autonomic nervous system changes and calcium handling abnormalities [4]. Changes in the autonomic nervous system and calcium handling abnormalities can prolong action potentials and generate delayed afterdepolarizations of sufficient magnitude to trigger spontaneous atrial ectopic activation [4, 47]. These mechanisms create a substrate for AF and facilitate a vicious circle where "AF begets AF" [49, 50, 51, 4]. Despite exhibiting uncoordinated electrical activity, AF can arise from a regularly firing source, with propagation through the AF substrate leading to chaotic and irregular atrial excitation patterns [4, 52]. These sources are typically observed as either reentrant circuits or focal ectopic activity [53]. A reentrant circuit is defined by a self-sustaining electrical excitation wave circulating an anatomical obstacle [54], while an ectopic focus is defined as a cardiac site other than the SA node that functions as a pacemaker with a significantly higher firing rate than the SA node [53]. Spontaneous atrial ectopic activity can be promoted by both autonomic hyperinnervation and calcium handling abnormalities [4]. Reentry requires that the conduction time of a full circle of electrical activation exceeds the refractory period, a condition facilitated by both electrical and structural remodeling [4].

3.3 Management of Atrial Fibrillation

The management of AF starts with the confirmation using a 12-lead ECG or a rhythm strip showing AF pattern for $\geq$30 s [3]. The next step in AF management is the characterization of AF, which encompasses stroke risk stratification using the CHA_2DS_2-VASc score, symptom severity assessment via the EHRA score, AF burden quantification based on time spent in AF, and substrate severity evaluation through clinical assessment and imaging [3]. The CHA_2DS_2-VASc score summarizes clinical risk factors and awards points to congestive heart failure, hypertension, age $\geq$75 years, diabetes mellitus, stroke, vascular disease, age 65–74 years, and sex category (female) [3]. The EHRA symptom scale quantifies AF-related symptoms from none to mild, moderate, severe, and disabling [3]. Finally, the treatment of AF involves a three-pronged approach: 1) stroke prevention guided by the CHA_2DS_2-VASc score, 2) management of comorbidities and cardiovascular risk factors through lifestyle modifications such as weight loss, exercise, and reduced alcohol consumption, and 3) symptom control [3].

The AF patient cohorts studied in *Paper I–IV* represented AF at different stages of disease progression. The AF pattern is classified into five classes based on the duration of continuous AF: first diagnosed (*Paper IV*), paroxysmal (*Paper II–III*), persistent (*Paper I–III*), long-standing persistent, and permanent. If AF has not been diagnosed before, it is 'first-diagnosed'; if AF terminates within 7 days of onset, it is 'paroxysmal'; if it is sustained between 7 days to 12 months, it is 'persistent'; if it is sustained for longer than 12 months, it is 'long-standing persistent'. In these four classes, the patient and clinician discuss treatment options to restore and maintain NSR. If no further attempts to restore NSR are planned, then AF is classified as 'permanent' [3, 1].

Symptom control can be realized with rate control and rhythm control. The goal of rate control is to keep the average heart rate below 100-110 beats per minute [3]. In most cases, rate control is realized with drugs, such as beta-blockers and calcium-channel blockers [3]. When medication fails, an alternative rate control approach is ablating the AV node and implantation of a pacemaker to control the ventricular rate [3]. The goal of rhythm control is to restore and maintain NSR. In the first 48 hours of AF onset, cardioversion is the preferred method to restore NSR [3]. In patients with paroxysmal or persistent AF, targeted ablation of ectopic foci or reentrant circuits aims to eliminate the sources of AF and restore NSR [55, 56].

Chapter 4
Analysis of Cardiac Signals

This chapter discusses the analysis of clinical signals relevant to addressing the three aims of this thesis. Because direct measurements of AV nodal conduction are practically impossible to obtain in AF patients, the AV nodal conduction properties in *Paper I–III* are estimated from ECG-derived features described in Section 4.1. In Section 4.1.1, the extraction of f-wave signals from ECG signals of AF patients is described together with three f-wave characteristics quantifying the uncoordinated atrial electrical activity. The f-wave characteristics are used in *Paper I–II* to model the atrial electrical activity and in *Paper IV* to study their prognostic value on clinical outcomes such as total mortality in the earliest stages of AF. In Section 4.1.2, the detection of ventricular activations from ECG signals are described together with three RR series characteristics quantifying the irregular ventricular activity. The RR series characteristics are used in *Paper I–III* to quantify the ventricular activity. In Section 4.1.3, the extraction of respiration signals from 12-lead ECG of AF patients is described. The respiration signals are used in *Paper II* to predict respiration-induced autonomic modulation in AV nodal conduction during AF.

A recurring theme in this PhD thesis is the development of computational models and the model-based analysis of clinical signals. In this context, a sensitivity analysis described in Section 4.2 is applied in *Paper I* to study the individual influence of each model parameter on the AV node model output. Furthermore, Section 4.3 gives an introduction to convolutional neural networks (CNNs) that can be trained to learn complex, non-linear relationships within data which is used in *Paper II* to predict the magnitude of respiration-induced autonomic modulation from ECG signals in AF patients.

Finally, to evaluate clinical significance of the derived ECG characteristics and fitted model parameters, an introduction to survival analysis is given in Section 4.4, which is used in *Paper IV* to compare the survival outcomes among groups within a

study cohort. In Section 4.4.1, the Kaplan-Meier estimator is described for visualizing the survival curves of each group over time. In Section 4.4.2, the Cox proportional hazards model is described to assess whether two groups are at an equal or different risk of a clinical outcome.

4.1 ECG Analysis

In Chapter 2, the ECG was described as a non-invasive sensor that captures the electrical conduction propagation through the heart. The ECG measures the electric field on the body surface that results from electrophysiological processes ranging from the molecular to the organ level. In Chapter 3, the characteristic differences in ECG recordings between NSR and AF were described, highlighting an irregular RR series, absence of P waves, and presence of f-waves as the basis of AF diagnosis. This section covers the analysis of ECG signals for quantifying the atrial rhythm based on f-wave characteristics, the ventricular rhythm in AF based on RR series characteristics, and the respiration based on ECG-derived respiration signals.

4.1.1 Analysis of f-waves

During AF, f-waves are a component in the ECG signal representing the rapid and uncoordinated atrial activity. The f-waves have predictive clinical value. For example, f-wave characteristics such as atrial fibrillation rate, average amplitude of the f-wave envelope, and organization index derived from the signal's spectral characteristics can be predictive of spontaneous termination of paroxysmal AF [57, 58, 59], atrial tissue pathology [60, 61], and increased mortality in congestive heart failure patients with AF [23]. Because the f-waves represent atrial activity and the QRST complex represents ventricular activity in AF (Section 3.1), the f-waves can be extracted from the ECG by removal of the QRST component. For *Paper I*, *II*, and *IV*, f-wave signals were extracted from the ECG using spatiotemporal QRST cancellation [62]. Spatiotemporal QRST cancellation is based on average beat subtraction. Each ECG lead is processed independently. The average beat subtraction creates a beat template from the average of time-aligned beats, which is then subtracted from each beat in the ECG lead. Spatiotemporal QRST cancellation corrects for the variations in the orientation of the heart's electrical axis that is primarily induced by respiration and takes all leads into account when creating a beat template [44]. Figure 4.1 shows a typical f-wave signal extracted using spatiotemporal QRST cancellation.

In this thesis, the f-wave signal has been characterized by the atrial fibrillatory rate (AFR), the average amplitude of the f-wave envelope (Amp), and an organization index derived from the signal spectral characteristics (ExpDec). The AFR represents

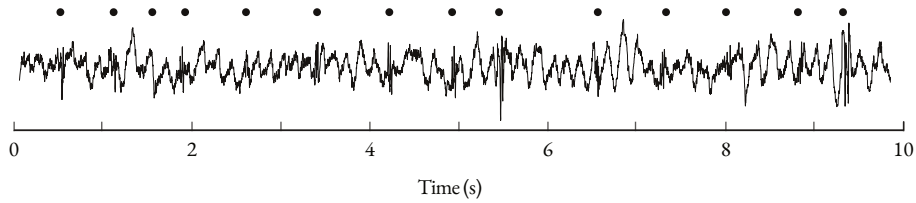

Figure 4.1: Example of f-wave signal in lead V_2 using spatiotemporal QRST cancellation. The dots indicate the location of the removed QRS complexes. Adapted from Sörnmo [44] with permission from Springer Nature.

the dominant frequency in the f-waves and serves as a surrogate marker for the atrial refractory period [63]. In *Paper I*, *II*, and *IV*, an AFR trend $f(n_1)$ sampled at 50 Hz was estimated by fitting a complex sinusoidal model $s(n_1)$ to a 20 ms overlapping 0.5 s segment of the f-wave signal [64, 65], as defined in Eq. 4.1

$$s(n_1) = \sum_{m_1=1}^{M_1} A_m e^{j(2\pi f_0 m_1 n_1 + \phi_m)}, \tag{4.1}$$

where AFR in each segment corresponded to the fundamental frequency f_0 in $s(n_1)$ and $n_1 = 0, \ldots, N_1 - 1$ with N_1 samples. The AFR trend $f(n_1)$ comprises the local frequency estimates of $\hat{f}_0$ estimated from each segment using maximum likelihood estimation. The complex sinusoidal model $s(n_1)$ consists of two harmonically related complex exponentials ($M_1 = 2$), where A_m and ϕ_m represent the amplitude and phase of the m:th exponential. In *Paper I*, the mean and standard deviation of atrial inter-arrival times are estimated from the mean and standard deviation of $f(n_1)$ to account for changes in AFR during the tilt test. In *Paper II* and *IV*, a constant AFR value is computed for each patient from the mean of the extracted AFR trend.

A high average amplitude of the f-wave envelope (Amp) before catheter ablation predicts AF termination and freedom from AF at follow-up. In contrast, a low Amp suggests AF continuation and left atrial enlargement [60]. For the calculation of Amp, an upper envelope $e_{MAX}(n_2)$ and lower envelope $e_{MIN}(n_2)$ passing through local maxima and local minima of the f-waves, respectively, were estimated by the shape-preserving piecewise cubic Hermite interpolating polynomial (PCHIP) [66]. The Amp was computed as the mean of the absolute difference between the upper and lower envelope with N_2 samples as defined in Eq. 4.2

$$\text{Amp} = \frac{1}{N_2} \sum_{n_2=1}^{N_2} |e_{MAX}(n_2) - e_{MIN}(n_2)|. \tag{4.2}$$

The degree of f-wave organization characterized by ExpDec is predictive of NSR maintenance after cardioversion of AF [67]. The ExpDec characterizes the exponential decay in magnitude between the AFR and its harmonics in the f-waves' frequency spectrum. The frequency spectrum of the f-waves was computed using a short-term Fourier transform, where the f-wave signal was divided into 128 sample-long segments with 50 sample overlaps [12]. For the calculation of ExpDec, a spectral line model was fitted to the frequency spectrum of the f-waves as described in Eq. 4.3

$$\phi_l(p_l + h_m) = \begin{cases} b_l e^{-\gamma_l m_3}, & m_3 = 0, 1, ..., M_3, \\ 0, & \text{otherwise}, \end{cases} \tag{4.3}$$

where ϕ_l represents the normalized spectral profile, p_l is the fundamental frequency determined by the peak position in an exponentially averaged input spectrum, h_m denotes the offset position of the m_3:th harmonic relative to p_l, γ_l describes the exponential decay, and b_l is the magnitude at p_l. The spectral line model allows a decoupled description of the fundamental frequency and the waveform shape. In the spectral line model, the frequency corresponding to the AFR is represented by $m_3 = 0$, while its harmonics are represented by $m_3 > 0$. Here, M_3 is chosen to consider only harmonics below 20 Hz [12].

4.1.2 Analysis of RR Series

For the analysis of the ventricular activity in NSR and AF, the RR series was characterized by its mean, variability, and irregularity. As illustrated in Figure 4.5, the RR series comprises intervals between consecutive heartbeats, where the time of a heartbeat is determined by the corresponding R peak in the ECG signal. The R peaks were detected using CardioLund ECG parser in *Paper I–II* and using the free ECGdeli toolbox in *Paper III* [68]. The mean of the RR intervals was computed according to

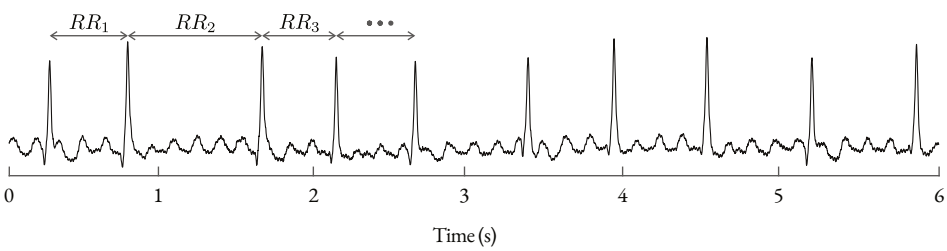

Figure 4.2: ECG signal in atrial fibrillation with an irregular series of RR intervals RR_i. Adapted from Sörnmo [44] with permission from Springer Nature.

Eq. 4.4

$$\overline{RR} = \frac{1}{N}\sum_{i=1}^{N} RR_i, \tag{4.4}$$

where RR_i denotes the i:th RR interval in the RR series that follows the i:th heatbeat. In *Paper I–II*, the RR series variability was computed as the root mean square of successive RR interval differences (RR rmssd) defined in Eq. 4.5

$$RR_V = \sqrt{\frac{1}{N-1}\sum_{i=1}^{N-1}(RR_{i+1} - RR_i)^2}. \tag{4.5}$$

In *Paper III*, the RR series variability was computed as the RR rmssd normalized with respect to $\overline{RR}$ to facilitate the comparison between RR series variabilities over a range of heart rates as described in Eq. 4.6 (Figure 4.3)

$$\hat{RR}_V = \frac{RR_V}{\overline{RR}}. \tag{4.6}$$

The RR series irregularity was computed as the sample entropy of the RR series, characterized as the logarithm of the conditional probability that, within a specified tolerance r, a sequence that recurs for m samples will also recur for $m+1$ samples, as described in Eq. 4.7 (Figure 4.3)

$$RR_I = -\ln\left(\frac{\sum_{i=1}^{N-m}\sum_{j=1,j\neq i}^{N-m} b_{i,j}^{m+1}(r)}{\sum_{i=1}^{N-m}\sum_{j=1,j\neq i}^{N-m} b_{i,j}^{m}(r)}\right). \tag{4.7}$$

The binary variable $b_{i,j}^{l}(r)$ with $l \in \{m, m+1\}$ has the value 1 if the maximum absolute distance between corresponding scalar elements in the vectors $V_i^l = \{RR_i, RR_{i+1}, ..., RR_{i+l-1}\}$ and V_j^l is below the tolerance r times the standard deviation of the RR interval series; otherwise the value is zero [69]. In *Paper I–III*, the parameters were set to $m = 2$ and $r = 0.2$.

Compared to NSR, the $\overline{RR}$ is decreased, and RR_V and RR_I are increased in AF. To provide context for normal ranges of RR series variability, the study by McManus et al. [70] found an $\hat{RR}_V^{AF} = 0.29 \pm 0.09$ in 76 AF patients and an $\hat{RR}_V^{NSR} = 0.08 \pm 0.08$ in 18 ECG recordings during NSR. An RR series variability threshold of 0.115 for $\hat{RR}_V$ was determined best for the use in AF detection [70]. For RR series irregularity, the study by Corino et al. [71] found an $RR_I^{AF} = 1.68 \pm 0.18$ in 60 AF patients and the study by Solís-Montufar et al. [72] found an $RR_I^{NSR} = 0.84 \pm 0.204$ in 52 healthy subjects while sleeping.

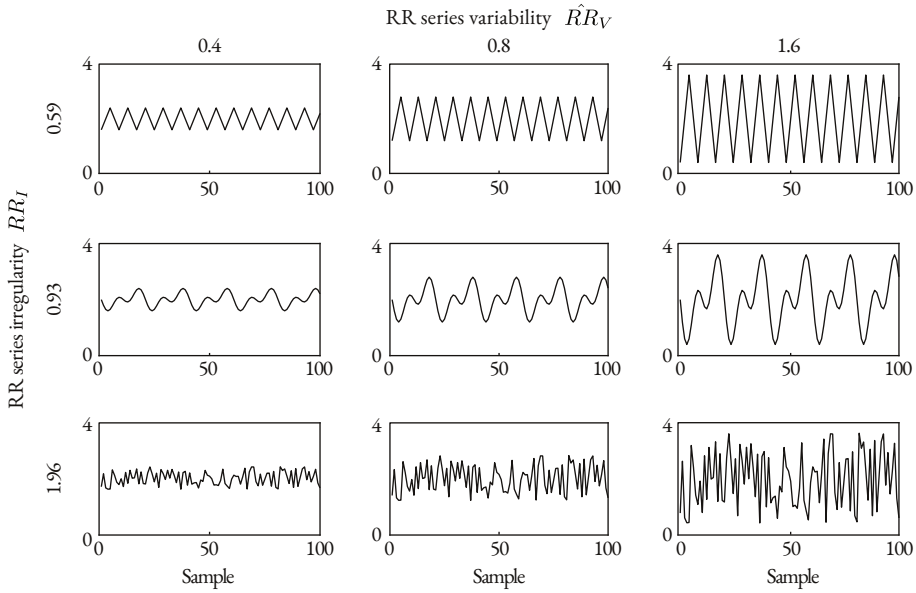

Figure 4.3: Comparative visualization of RR series characteristics, illustrating the independent parameters of variability (horizontal axis) and irregularity (vertical axis). Each panel shows an RR series with identical irregularity but increasing variability (left to right) or identical variability but increasing irregularity (top to bottom). The axis units are arbitrary. Adapted from Sörnmo [44] with permission from Springer Nature.

4.1.3 ECG-derived Respiration

Respiration modulates the ECG, resulting in baseline wander, amplitude modulation, and frequency modulation [73]. Baseline wander and amplitude modulation arise from dynamic changes in the heart's electrical axis relative to the electrodes and changes in thoracic impedance [73]. Frequency modulation reflects respiratory sinus arrhythmia, characterized by an increase in heart rate during inspiration and a decrease during exhalation. Various filter-based and feature-based techniques have been proposed to extract the respiration signal from the ECG, as summarized in [73]. However, in AF, frequency modulation cannot reliably capture respiration, as RR interval fluctuations originate not solely from the autonomic modulation of the SA node but also from the uncoordinated and irregular atrial activity. Among the available methods, the feature-based slope range technique demonstrated the best performance in robustly estimating the respiration rate from the ECG during AF [74]. In a single ECG lead segment $y_i(n)$ comprising an i:th QRS complex, the slope range method extracts respiration information and is defined by the difference between the maximum up-slope and minimum down-slope as defined in Eq. 4.8

$$d_{SR}(i) = \max_n \left(y'(n)\right) - \min_n \left(y'(n)\right), \tag{4.8}$$

where $y'_i(n) = y_i(n) - y_i(n-1)$ [74]. Consequently, the respiration signal is sampled non-uniformly, with one sample at the location of each heartbeat. To create an uniformly sampled respiration signal from the non-uniformly sampled slope range values, the signal can be resampled using shape-preserving piecewise cubic Hermite interpolating polynomial (PCHIP) [75].

4.2 Analysis of the Model

In the model development, a sensitivity analysis enables quantifying how uncertainties in model inputs $\boldsymbol{x} = [x_1, x_2, \ldots, x_N]$ propagate to affect the model's outputs $\boldsymbol{y} = [y_1, y_2, \ldots, y_M]$ [76]. The sensitivity analysis techniques are fundamentally divided into local and global methodologies, each offering distinct advantages for uncertainty quantification. Local sensitivity analysis assesses parameter sensitivity by evaluating variations around a specific point in the parameter space, utilizing partial derivatives that can be approximated through methods such as finite differences. In its most basic form, a local sensitivity analysis yields the partial derivative of the model with respect to a single input factor $\partial y_m / \partial x_n$, with the one-at-a-time approach representing a widely implemented variation of this methodology [76]. The partial derivative quantifies how much each input x_n affects each output y_m at a given point in the input space. This computationally efficient local sensitivity analysis yields reliable sensitivity indices for linear models with negligible parameter interactions.

For nonlinear models, global sensitivity analysis techniques are more suitable. These methods systematically evaluate the output variations across the complete range of possible input parameters simultaneously, thereby accounting for parameter interactions. Variance-based sensitivity analysis, particularly Sobol's method, represents a prominent example of global sensitivity analysis techniques [77]. In this method, the sensitivity index of a model input represents the expected proportional reduction in output variance resulting from fixing that particular model input.

However, variance-based sensitivity analysis techniques inherently assume that the outputs follow a normal distribution. Given that the RR series characteristics produced by the AV node model exhibited skewed and multi-modal distributions, a distribution-based sensitivity analysis was implemented in *Paper I* instead [78]. This alternative approach requires no assumptions regarding the shape of the output distribution, making it more suitable for the complex dynamics observed in the AV node model. For each combination of the n:th model input x_n and the m:th model output y_m, a sensitivity coefficient $\mathcal{S}_{n,m}$ is computed as defined in Eq. 4.9

$$\mathcal{S}_{n,m} = \underset{c=1,\ldots,C}{\text{median}} \; \underset{d=1,\ldots,D}{\text{median}} \; \text{KS}(F_{y_m}^{(d)}(y_m), F_{y_m|x_n}(y_m|x_n \in \mathcal{I}_c)). \tag{4.9}$$

The Kolmogorov-Smirnov (KS) distance measures the difference between two empirical cumulative distribution functions (CDFs): the unconditional $F_{y_m}^{(d)}(y_m)$ and the conditional $F_{y_m|x_n}(y_m|x_n \in \mathcal{I}c)$. To approximate the conditional CDF, the parameter space of x_n is divided into C equal intervals $\mathcal{I}c$ (where $c = 1, ..., C$), and all samples within each interval contribute to the corresponding conditional CDF estimation. The unconditional CDFs are generated through bootstrapping, where K/C samples are randomly selected D times to create multiple reference distributions $F_{y_m}^{(d)}(y_m)$. All CDFs are computed as defined in Eq. 4.10

$$F_l(y) = \frac{1}{l} \sum_{k=1}^{l} I(y_k \leq y), \tag{4.10}$$

where l is the number of samples and $I(y_k \leq y)$ is an indicator function that is 1 if $y_k \leq y$ and 0 otherwise. Due to the finite sampling nature of both conditional and unconditional CDFs, even parameters with no actual influence on y_m may yield non-zero $\mathcal{S}_{n,m}$ values. To account for these approximation errors, a dummy parameter $\mathcal{D}_m$ is computed for each output y_m:

$$\mathcal{D}_m = \underset{d=2,\ldots,D}{\text{median}} \; \text{KS}(F_{y_m}^{(d)}(y_m), F_{y_m}^{(1)}(y_m)), \tag{4.11}$$

This dummy parameter serves as a threshold: a model parameter x_n is considered to significantly influence y_m only when its sensitivity coefficient exceeds this threshold ($\mathcal{S}_{n,m} > \mathcal{D}_m$).

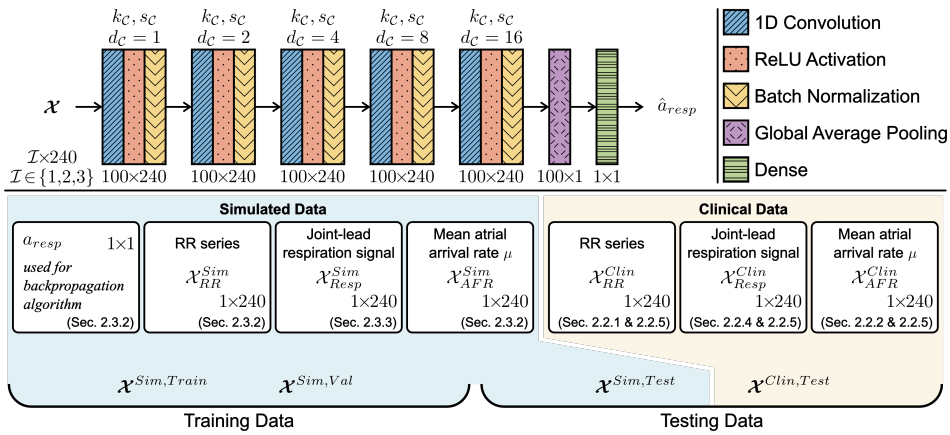

Figure 4.4: The CNN was composed of five 1D convolution layers with 100 filters each. The convolution layers had a kernel size $k_\mathcal{C} = 3$, stride $s_\mathcal{C} = 1$ and dilation factor $d_\mathcal{C}$. Training datasets $\boldsymbol{\mathcal{X}}^{Sim,Train}$, validation datasets $\boldsymbol{\mathcal{X}}^{Sim,Val}$, and testing datasets $\boldsymbol{\mathcal{X}}^{Sim,Test}$ were constructed from the simulated data $\mathcal{X}_{RR}^{Sim}$, $\mathcal{X}_{Resp}^{Sim}$ and $\mathcal{X}_{AFR}^{Sim}$. A testing dataset $\boldsymbol{\mathcal{X}}^{Clin,Test}$ was constructed from the clinical ECG-derived features $\mathcal{X}_{RR}^{Clin}$, $\mathcal{X}_{Resp}^{Clin}$ and $\mathcal{X}_{AFR}^{Clin}$.

4.3 Neural network

Neural networks have emerged as powerful tools in ECG analysis, facilitating the extraction and interpretation of complex patterns within ECG signals and predicting clinical markers. These networks can learn complex, non-linear relationships within data, which has led to their application in biomedical engineering tasks such as automatically classifying ECG abnormalities [79]. The layered structure of neural networks allows for the sequential processing of input features at different levels of abstraction.

Paper II presents a 1-dimensional (1D)-CNN developed to predict respiratory modulation during AF using time series data from RR intervals, respiration signals, and AFR (Figure 4.4). While neural networks require large amounts of training data, clinical data is often sparse. To address this limitation, computational modeling was used to generate synthetic datasets. The 1D-CNN architecture was constructed with building blocks representing five layer types: 1D convolution layers, ReLU activation layers, batch normalization layers, global average pooling layers, and dense layers. The 1D convolution layers process temporal input data by applying sliding convolutional filters and computing the dot product of weights and inputs before adding a bias term. Following these, rectified linear unit (ReLU) layers introduce non-linearity through a thresholding operation that maintains positive values while setting negative inputs to zero. The ReLU activation function enables us to learn and represent complex,

non-linear relationships between input features [80]. This activation mechanism shares similarities with biological neurons, where activation occurs only above a certain threshold. Batch normalization layers normalize each row in the d-dimensional input $\boldsymbol{x} = [x_1(n), \ldots, x_d(n)]^\intercal$, enabling faster training through higher learning rates while achieving comparable accuracy with fewer training steps [81]. At the end of the 1D-CNN, global average pooling layers reduce dimensional complexity by converting each row in the d-dimensional input $\boldsymbol{x}$ into a single value through temporal averaging. Finally, dense layers integrate the learned features by multiplying weights and adding biases to produce the prediction based on the patterns in the temporal input data.

4.4 Survival analysis

Survival analysis provides a statistical framework for time-to-event analysis, allowing one to model the time until a specific event and to compare the survival outcomes across different groups. This section introduces two fundamental techniques: the Kaplan-Meier method for visualizing survival probabilities over time and the Cox proportional hazards model for assessing the impact of various factors on event occurrence.

4.4.1 Kaplan-Meier estimator

Survival analysis is a statistical approach that examines the temporal progression to a specified event by monitoring subjects over time. Survival analysis requires two key pieces of information: the duration from a predetermined starting point to either the event occurrence or the end of the observation period and the event status within this timeframe. To illustrate, in a mortality study, a subject's death one year after enrollment would be recorded with a time value of one year and a status indicator of 1, denoting the event's occurrence. Alternatively, subjects who remain alive at study completion or lose contact during follow-up receive a status indicator of 0, representing censored data. Censoring occurs when the event does not happen until the end of the follow-up. This may result from various circumstances, including participant withdrawal, study conclusion, or intervening events that preclude the event of interest. Rather than excluding censored observations, which would introduce statistical bias, these data provide valuable information about event-free survival up to the censoring point [82].

The Kaplan-Meier estimator is a widely used non-parametric statistical tool for estimating the survival function, $S(t)$, which quantifies the probability of survival beyond time t. The estimated survival function $\hat{S}(t)$ is calculated according to Eq. 4.12

$$\hat{S}(t) = \prod_{i:\, t_i \leq t} \left(1 - \frac{d_i}{n_i}\right), \tag{4.12}$$

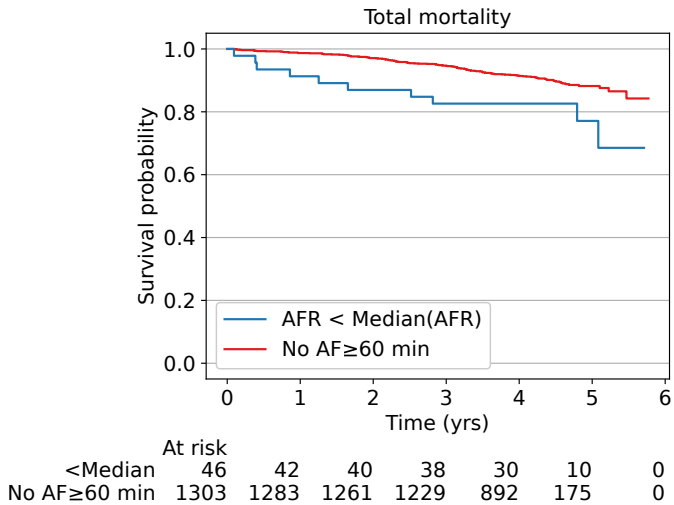

Figure 4.5: Kaplan–Meier plots for the AFR on total mortality for patients with AF episodes $\geq$60 min. The estimated survival function of the reference group containing patients without AF episodes $\geq$60 min is illustrated by the red line, and the estimated survival function of the patients with AF episodes $\geq$60 min and an AFR estimate below the population median is illustrated by the blue line. At 0 years in the plot, patients had lived with an implantable loop recorder for 1 year. The decreasing 'At risk' numbers below the plot shows how many subjects remained in the study population due to the event or censoring.

where t_i denotes the time of an event, d_i the number of events (e.g., death, cardiovascular death, heart failure, stroke) at t_i, and n_i the number of individuals at risk at t_i. The number n_i is defined as the total population minus those who experienced an event or were censored before t_i [83]. The Kaplan-Meier estimator computes the survival probabilities at each event occurrence, accounting for the current at-risk population. These discrete probability calculations are subsequently connected to generate a step function, as demonstrated in Figure 4.5, which depicts survival rates for two distinct groups analyzed in *Paper IV*. This graphical representation facilitates group comparisons and provides comprehensive temporal insights into event occurrence patterns. The strength of the Kaplan-Meier estimator lies in its distribution-free approach to survival time analysis and its capability to accommodate censoring at varied time points across the study population. This feature is essential in longitudinal studies where subjects may enter and exit the study at various times.

4.4.2 Cox proportional hazards model

The Cox proportional hazards model is a regression technique used to investigate the influence of various covariates on event rates over time. The model is based on the hazard function $h(t|x_i)$ described in Eq. 4.13

$$h(t|x_i) = h_0(t) \cdot \exp\left(\sum_{j=1}^{p} x_{ij}\beta_j\right), \tag{4.13}$$

where $h_0(t) \geq 0$ is the baseline hazard function, $x_i = [x_{i1}, \ldots, x_{ip}]$ represent covariates for an individual i, and $\beta = [\beta_1, \ldots, \beta_p]$ are the corresponding scaling factors for each covariate. The hazard function represents the instantaneous probability of an event occurring at time t, given survival up to that point. No assumptions are made about the functional form of the baseline hazard function $h_0(t)$. This is possible, because $h_0(t)$ gets canceled out in the estimation of β. The Cox model can accommodate diverse types for the covariates x_i, including continuous variables (e.g., age), categorical variables (e.g., gender), and binary variables (e.g., presence of hypertension). The scaling factors β are estimated by maximizing the partial likelihood in Eq. 4.14 with respect to β,

$$PL(\beta) = \prod_{i:\delta_i=1} \frac{\exp\left(\sum_{j=1}^{p} x_{ij}\beta_j\right)}{\sum_{i':t'_i \geq t_i} \exp\left(\sum_{j=1}^{p} x_{i'j}\beta_j\right)}, \tag{4.14}$$

where t_i is the event time of the i:th observation that is not censored ($\delta_i = 1$) [84].

A key assumption of the Cox model is the proportionality of hazards, which means that the hazard ratio, defined in Eq. 4.15, remains constant throughout the observation period between individuals with a hazard function $h_k(t)$ and those with a hazard function $h'_k(t)$.

$$HR = \frac{h_k(t)}{h'_k(t)} = \frac{h_0(t) \cdot \exp\left(\sum_{i=1}^{N} \beta_i x_i\right)}{h_0(t) \cdot \exp\left(\sum_{i=1}^{N} \beta_i x'_i\right)} = \frac{\exp\left(\sum_{i=1}^{N} \beta_i x_i\right)}{\exp\left(\sum_{i=1}^{N} \beta_i x'_i\right)} \tag{4.15}$$

If a study group has a hazard function $h_k(t)$ and a reference group has a hazard function $h'_k(t)$, a hazard ratio greater than 1 indicates an increased risk, while a value less than 1 indicates a decreased risk compared to the reference group. In *Paper IV*, the hazard ratio was computed to investigate the prognostic value of f-wave characteristics derived from implantable loop recorder for clinical outcomes in patients at the earliest stages of AF.

Chapter 5
Cardiac Modeling

This chapter gives an overview of relevant cardiac computational models. Generally, the modeling choices of the cardiac computational models are based on the accumulated understanding of cardiac physiology developed from previous experiments in animals or humans. The level of detail and amount of incorporated mechanisms are modeling choices and have to be weighed against the interpretability and computation time of the model. Therefore, no one-size-fits-all model exists, but many highly specialized computational models have been developed for specific use cases. The challenge in developing cardiac computational models is identifying a choice of model properties essential for reproducing experimental data and for which previous studies can support the choice.

Cardiac physiology can be understood on multiple levels of abstraction, from the molecular to the cellular, tissue, organ, and organ system levels. Cardiac computational models conform to the same levels of abstraction, e.g., modeling ion channels on the molecular level [85], modeling action potentials on the cellular level [85, 86, 17], modeling electrical excitation propagation on the tissue level [87, 86, 17], modeling the cardiac conduction system on the organ level [17], and modeling the interaction between the nervous system and the heart on the organ system level [88]. Often, computational models focus on mechanisms on a single level if the research question allows for the assumption that the mechanisms on this level can be viewed in isolation from the other levels. But there are also multi-scale models integrating mechanisms on multiple levels to explain how changes at one level can impact the entire system [89, 90, 91, 92]. Multi-scale modeling of the heart comes with both advantages and disadvantages. With a multi-scale model, it is, for example, possible to test the hypothesis that a change in sodium channel conductance on the molecular level affects the electrical excitation propagation in the heart on the organ level and explains an ST-elevation in the ECG in Brugada syndrome [91]. A limitation of multi-scale models can

be the computational cost, mainly when replicating cellular processes at high resolution across the entire organ. For example, one cardiac cycle of 800 ms in the work of Wülfers et al. [91] took approximately 45 min on a high-performance computer. When investigating cardiac arrhythmias, requiring the simulation of numerous cardiac cycles, or when personalizing models to patient-specific data, requiring numerous simulations, the computational burden necessitates either a reduction in model complexity or the optimization of the algorithms [18, 17]. The reduction of computational cost could be achieved by abandoning a multi-scale approach or by reducing the complexity of the physiological process description with an approximation of the physiological processes.

The first aim of this thesis is the development of an AV node model to study patient-specific ANS modulation on AV nodal conduction properties during AF based on ECG recordings. A design decision was to keep the number of model parameters manageable so that the function could be interpreted, computation times could be short, and the model parameters could be estimated from non-invasive clinical data. In Section 5.1, an overview of previously published AV node models is given. Section 5.1.6 describes the network AV node model adopted in this thesis. The design decisions for the network AV node model can be described in five points by which all the other AV node models are assessed in this section: 1) the AV nodal dual-pathway physiology, 2) the description of the refractory period, and 3) conduction delay, 4) the arrival of atrial impulses into the AV node model, 5) and how the model was fitted to clinical data.

This thesis's second aim is to develop a computational model to study patient-specific hemodynamics during AF based on ECG recordings and hemodynamic measurements. The design decisions are based on the same philosophy as the first aim: to enable short computation times for numerous simulations with numerous cardiac cycles. In Section 5.2, an overview of previously published hemodynamic models is given. The design decisions for the hemodynamic model can be described in three points by which all the other hemodynamic models are assessed in this section: 1) the cardiac mechanics, 2) the cardiac electrophysiology, 3) and the mechanics of the vasculature.

5.1 AV Node Models

This overview focuses exclusively on AV node models described at the tissue level [93, 94, 95, 96, 97, 98, 99]. For models that rely on action potentials described on the cellular level for electrical conduction, the reader is referred to [100, 101, 102, 103, 104, 105, 106, 107, 108]; these models are excluded from this overview as their computational complexity contradicts the efficiency criteria established for the first aim of the thesis. For models designed for fitting to experimental data collected with

the S_1S_2 or $S_1S_2S_3$ pacing protocols described in [109], the reader is referred to [110, 111, 112, 113, 114]; these models are excluded from this overview as their parameter estimation requires intracardiac recordings, contradicting the non-invasive clinical data requirement established for the first aim of the thesis. At the tissue level, the electrical activation propagates over the cardiac tissue as a wave (Section 2.3). In the models described below, the electrical excitation propagation as a waveform is frequently simplified to an impulse characterized solely by its time of arrival and location. Commonly, various researchers use distinct variables to represent identical model parameters in their descriptions of the same phenomenon. To enhance clarity and facilitate the comparison of similarities and disparities among AV node model representations, the model descriptions from prior research were reformatted to align with the terminology utilized in our AV node network model. When applicable, the refractory period $R^P(\Delta t_k)$ and conduction delay $D^P(\Delta t_k)$ are characterized for an AV nodal pathway P with respect to the diastolic interval Δt_k defined in Eq. 5.1

$$\Delta t_k = t_k - t_{k-1} - R^P(\Delta t_{k-1})\,, \tag{5.1}$$

where t_k denotes the arrival time of the k:th conducted electrical impulse.

5.1.1 Precedent Descriptions of AVN Dual-pathway Physiology

The AV node has a dual-pathway physiology with distinct electrical conduction properties within the tissue of the respective pathways (Section 2.3).

In the work of Corino et al. [96, 97] and Henriksson et al. [99], the dual-pathway physiology was described in a lumped statistical model, where atrial impulses enter exclusively one of two pathways. The lumped statistical model does not simulate the conduction of discrete impulses; rather, it characterizes the conduction of a distribution of atrial impulses through the SP with a probability of $\alpha \in [0, 1]$ and conversely through the FP with a probability of $1-\alpha$.

In the AV node models described in Cohen et al. [93], Mangin et al. [94], Lian et al. [95], and Masè et al. [98], the dual-pathway physiology was not incorporated, and the conduction through the AV node was simplified by a single pathway.

5.1.2 Precedent Descriptions of AVN Refractory Period

The myocardium can be electrically stimulated to induce a mechanical contraction and propagate the electrical excitation to adjacent cells. However, a cardiac cell is insensitive to electrical conduction during the absolute refractory period and exhibits reduced sensitivity during the subsequent relative refractory period. AV nodal conduction and blockage in the following AV node models are determined by a refractory period

$R(\Delta t_k)$, permitting the conduction of an impulse if $\Delta t_k \geq 0$ (Eq. 5.1). Many of the models described below characterize the refractory period with a minimum refractory period R_{min} [94, 95, 96, 97, 98, 99] and a prolongation of the refractory period ΔR [95, 96, 97, 99].

In the work in Cohen et al. [93], the refractory period was defined as in Eq. 5.2

$$R = \Delta R_\infty \left(1 - e^{-(t_i - t_{i-1})/\Delta R_\infty}\right) \tag{5.2}$$

where ΔR_∞ is the maximum refractory period.

In the work in Lian et al. [95], the computation of the refractory period incorporated a prolongation caused by concealed conduction. First, a refractory period $R(\Delta t_k)$ without concealed conduction was computed as in Eq. 5.3

$$R(\Delta t_k) = R_{min} + \Delta R \left(1 - e^{-\Delta t_k/\tau_R}\right) \tag{5.3}$$

where τ_R was a fixed model parameter representing the time constant of the exponential decay. Then, a correlated refractory period $R_{CC}(\Delta t_k)$ was computed by adding a term for concealed conduction as defined as in Eq. 5.4

$$R_{CC}(\Delta t_k) = R(\Delta t_k) + R_{min} \sum_j \left(\frac{t'_j - t_k}{R(\Delta t_k)}\right)^\theta \left(\max\left(1, V\right)\right)^\delta \tag{5.4}$$

where t'_j represents the time of the j:th blocked impulse, V is a constant for the AV nodal membrane potential, and θ and δ are positive scaling factors.

In the work in Mangin et al. [94] and Masè et al. [98], the refractory period was defined as in Eq. 5.5

$$R(\Delta t_k) = D(\Delta t_k) + R_{min} + \mathcal{N}(\mu_R, n \cdot \sigma_R^2), \tag{5.5}$$

where a stochastic prolongation was drawn from a Gaussian distribution with mean μ_R and standard deviation σ_R multiplied by the number n of blocked impulses since the last conducted impulse. Further, $D(\Delta t_k)$ was an AV nodal conduction delay computed according to Eq. 5.7.

Unlike the previous models [93, 94, 95, 98], where the relative refractory period is accounted for by a term incorporating the history of previously conducted impulses (Eq. 5.1), the lumped statistical model in Corino et al. [96, 97] and Henriksson et al. [99] described the relative refractory period for the two pathways $P \in \{\text{SP}, \text{FP}\}$ with a piecewise linear probability of conduction described in Eq. 5.6

$$\beta(t)^P = \begin{cases} 0, & 0 < t_k - t_{k-1} < R^P_{min}, \\ \dfrac{t_k - t_{k-1} - R^P_{min}}{\Delta R^P}, & R^P_{min} \leq t_k - t_{k-1} < R^P_{min} + \Delta R^P, \\ 1, & t_k - t_{k-1} \geq R^P_{min} + \Delta R^P. \end{cases} \tag{5.6}$$

Thus, all impulses are blocked if the time since the last conducted impulse is shorter than R^P_{min}, and all impulses are conducted if the time is longer than $R^P_{min} + \Delta R^P$, and between these two phases, the ratio of conducted atrial impulses increases linearly from 0 to 1.

5.1.3 Precedent Descriptions of AVN Conduction Delay

The speed of electrical conduction in the heart varies depending on the gap-junctions on the cell level and differs at different parts of the heart on the tissue level (Section 2.3). In the AV node models of Mangin et al. [94], Lian et al. [95], and Masè et al. [98], the conduction delay was characterized with a minimum conduction delay D_{min} and a prolongation of the conduction delay ΔD as defined in Eq. 5.7

$$D(\Delta t_k) = D_{min} + \Delta D e^{-\Delta t_k/\tau_D}, \tag{5.7}$$

where τ_D was a fixed model parameter.

In the AV node models described in Cohen et al. [93], Corino et al. [96, 97] and Henriksson et al. [99], the conduction delay between atrial and ventricular activation was not incorporated, and the conduction through the AV node was assumed to be instant.

5.1.4 Precedent Descriptions of Atrial Impulse Arrival

All AV node models described in this section required a series of atrial activation times, that was either extracted from clinical data or drawn from a stochastic distribution.

In the model of Cohen et al. [93], Lian et al. [95], Corino et al. [96, 97] and Henriksson et al. [99], the distribution of inter-arrival times of atrial activations was described as exponential distribution with mean $\mu_{AA} = 1/\lambda$, requiring a single parameter λ. In Cohen et al. [93] and Corino et al. [96], the distribution of AA intervals was defined within the ranges $[0, \infty)$. In Lian et al. [95], Corino et al. [97] and Henriksson et al. [99], the distribution was truncated to account for a minimum atrial refractory period of $\delta = 50$ ms and was defined within the ranges $[\delta, \infty)$. The mean of the exponential distribution after truncation was corrected in Corino et al. [97] and Henriksson et al. [99] by adjusting $\lambda = \lambda_{AFR}/(1 - \delta\lambda_{AFR})$.

In the model of Masè et al. [98], the distribution of inter-arrival times of atrial activations was described as Gaussian distribution with mean $\mu_{AA} \in [100\,\text{ms}, 250\,\text{ms}]$ and standard deviation $\sigma_{AA} = 25$ ms.

In the AV node models described in Mangin et al. [94], the series of atrial impulses was not drawn from a stochastic distribution. Instead, it was extracted from clinical unipolar epicardial signals.

5.1.5 Precedent Estimation of AV Nodal Refractory Period and Conduction Delay

Each model parameter must be assigned a value for simulation. Some of the previously described AV node models have been fitted to clinical data [93, 96, 97, 99, 94]. In the model of Cohen et al. [93], the mean inter-arrival time of atrial activations λ and average refractory period $\overline{R}$ was fitted to canine data.

In the model of Corino et al. [96, 97] and Henriksson et al. [99], the refractory period was fitted using the maximum likelihood technique with AFR and RR series extracted from ECG signals. The exponential distribution parameter $\lambda = \lambda_{AFR}$ was estimated as the average AFR. Deriving the AFR from the ECG involved the extraction of f-waves through spatiotemporal QRST cancellation [62], followed by AFR estimation from these f-waves with a hidden Markov model-based approach [115]. Using the model proposed in [97], changes in the refractory period were estimated in Corino et al. [97] between supine and head-up tilt; in Corino et al. [116] between baseline and β-blocker metoprolol; in Sandberg et al. [117] between baseline, β-blockers metoprolol and carvedilol, and calcium channel blockers verapamil and diltiazem; and in Corino et al. [118] between baseline, β-blocker esmolol, and selective A1-adenosine receptor agonist tecadenoson.

In the model of Mangin et al. [94], the refractory period and conduction delay were estimated using atrial and ventricular activation times extracted from atrial epicardial electrograms. Changes in conduction delay and refractory period were estimated before and after antiarrhythmic drug therapy for patients not receiving a drug, patients receiving amiodarone, patients receiving β-blocker metoprolol, and patients receiving amiodarone and metoprolol.

In the works of Lian et al. [95] and Masè et al. [98], the refractory period and conduction delay parameters were fixed and not fitted to clinical data.

5.1.6 Network AV Node Model Adopted in this Thesis

The network AV node model described in Karlsson et al. [119] was adopted for this work. The model incorporates the dual-pathway physiology with a network of 21 nodes, wherein the SP and FP are represented by two separate chains of 10 nodes solely connected at their last nodes. Impulses move bidirectionally between connected nodes, allowing for retrograde conduction and concealed conduction. The impulses leave the model through an additional node assigned to a third pathway category, namely the coupling node (CN), which receives impulses from the last node of the SP and FP. The nodes assigned to the same pathway $P \in \{\text{SP}, \text{FP}, \text{CN}\}$ use the same model parameters $R^P_{min}, \Delta R^P, \tau^P_R$ for the refractory period and $D^P_{min}, \Delta D^P, \tau^P_D$ for the conduction delay. Each node in the network AV node model has its own refractory

period $R^P(\Delta t_k)$ and conduction delay $D^P(\Delta t_k)$ as defined in Eqs. 5.8 and 5.9

$$R^P(\Delta t_k) = R^P_{min} + \Delta R^P \left(1 - e^{-\Delta t_k/\tau^P_R}\right) \tag{5.8}$$

$$D^P(\Delta t_k) = D^P_{min} + \Delta D^P e^{-\Delta t_k/\tau^P_D}, \tag{5.9}$$

using the diastolic interval Δt_k defined in Eq. 5.1. Whether an impulse is conducted to all adjacent nodes for $\Delta t_k \geq 0$ or blocked by the current node for $\Delta t_k < 0$ is determined by the refractory period $R^P(\Delta t_k)$. If an impulse is conducted, the delay of conduction between adjacent nodes is determined by the conduction delay $D^P(\Delta t_k)$. As noted in Section 5.1.3, this description of the conduction delay was previously used in the model of Mangin et al. [94], Lian et al. [95], and Masè et al. [98]. The impulses are processed chronologically and conducted node by node, utilizing a priority queue of nodes and sorted by impulse arrival time, as described in Wallman and Sandberg [120].

The series of atrial activation times were drawn from a truncated exponential distribution of inter-arrival times using $\lambda = \lambda_{AFR}/(1 - \delta\lambda_{AFR})$. All inter-arrival times below $\delta = 50$ ms were omitted to account for a minimum atrial refractory period of 50 ms. As described in Section 5.1.4, the truncated exponential distribution was previously used in the model of Corino et al. [97] and Henriksson et al. [99]. When fitting the model to ECG signals, the λ_{AFR} was estimated from the ECG by extracting the f-waves through spatiotemporal QRST cancellation [62], followed by AFR estimation from these f-waves with a hidden Markov model-based approach [115]. When the model was used to generate RR series characteristic for a patient population, the λ_{AFR} was drawn from a uniform distribution with the ranges [100 ms, 250 ms].

5.2 Hemodynamic Models

This section describes hemodynamic models using a modular architecture with interchangeable descriptions of cardiac mechanics, cardiac electrophysiology, and mechanics of the vasculature. This overview adopted this modular approach to accommodate the varying levels of detail found in previous studies. Depending on the specific research question and available clinical data, each module is represented in a simplified 0-dimensional or detailed 3-dimensional manner. All hemodynamic models in this overview simulate the dynamic interaction between blood volume and pressure within each compartment, numerically approximating the influence of volume on pressure and vice versa. Blood flow is determined by the pressure gradient and impedance between adjacent compartments, resulting in blood flow towards the compartment with lower pressure. Blood flow is bidirectional between the atria and the compartments of

the vasculature; however, heart valves located between the atria, ventricles, and arteries regulate blood flow. The simplest heart valve representation is analogous to a diode in series with a resistance, permitting unidirectional flow [121]. Valve regurgitation can be modeled using two parallel diodes with differing resistances oriented in opposite directions [122]. A more detailed valve description incorporates a time-varying orifice area, facilitating the calculation of blood flow velocity through the valve [123, 124]. More complex valve descriptions exist but are beyond the scope of this overview; the reader is referred to [125, 126, 127].

5.2.1 Modeling the Cardiac Mechanics

Previously proposed computational models of cardiac mechanics vary in complexity depending on the research question. Some incorporate all four heart chambers [123, 128, 129, 130, 90, 122], while others focus on the left and right ventricle [131], or the left atrium and left ventricle [132].

The simplest representation of a heart chamber employs a time-varying elastance model, where the heart muscle contraction is simulated as a change in elastance [133]. The pressure P_i at each time step t_i is calculated using Eq. 5.10,

$$P_i = E_i(V_i - V_d), \tag{5.10}$$

where V_i is the volume at time t_i, V_d is a constant, and E_i is the time-varying elastance. Various formulations for elastance have been proposed [134, 127, 135]; in Korakianitis and Shi [127] for example, ventricular elastance was modeled as defined in Eq. 5.11,

$$E_i = \begin{cases} \cos\left(\dfrac{t_i}{T_{s1}\,\pi}\right), & 0 \le t_i < T_{s1}, \\ \cos\left(\dfrac{t_i + T_{s2} - T_{s1}}{T_{s1}}\pi\right), & T_{s1} \le t_i \le T_{s2}, \\ 0, & T_{s2} \le t_i < T, \end{cases} \tag{5.11}$$

with time constants T_{s1} and T_{s2} for the systolic phase and the cardiac cycle length T.

Beyond the elastance model, a more sophisticated 0-dimensional representation of cardiac chambers has been developed. This approach, implemented in the widely used CircAdapt model, describes the heart chambers with spherical wall segments [123, 128]. The cavity mechanics are coupled to a one-fiber sarcomere mechanics model that links the macroscopic hemodynamic load to the myofiber stress and strain. The pressure in the heart chamber is determined from the myofiber stress σ_f, which is the sum of a passive stress element $\sigma_{f,pas}$ and an active stress element $\sigma_{f,act}$ as defined in Eq. 5.12,

$$\sigma_f = \sigma_{f,pas}(\epsilon_f) + \sigma_{f,act}(C, L_{sc}), \tag{5.12}$$

where ϵ_f is the myofiber strain that is computed from the compartment volume, C is the contractility that is modeled as a Hill-type function and is initiated by an electrical activation, and L_{sc} is the contractile element length and represents how stretched the spherical wall is [123, 128]. In the first description of the CircAdapt model [123], the left ventricle was a spherical chamber inside the right ventricle. This description was updated in Lumens et al. [128] with the introduction of the TriSeg formulation, where the left and right ventricle were described using three spherical wall segments connected at a junction circle representing the left free wall, septal wall, and right free wall. The curvature of the spherical wall segments is adjusted at each time step to achieve a tension equilibrium between the three spherical wall segments. This description of the cardiac mechanics is part of the CircAdapt model and was adopted in the hemodynamic model used in *Paper III*.

In contrast to these simplified 0-dimensional models, a significant body of research focuses on detailed multiscale 3-dimensional models [136, 137, 138, 139, 90]. These three-dimensional models comprise detailed descriptions of cardiac electrophysiology coupled with active and passive cardiac mechanics, represented by partial differential equations. The computational domain for these equations, i.e., the cardiac tissue, is typically described by geometries derived from end-diastolic magnetic resonance imaging (MRI) or computed tomography (CT), and discretized into millions of elements to facilitate numerical solution using, e.g., finite element methods. Due to their high computational cost, these whole-heart models are not suitable for the aims of this thesis.

5.2.2 Modeling the Cardiac Electrophysiology

The simulation of cardiac mechanics requires defining the timing of mechanical contraction, which is initiated by electrical conduction. Detailed 3-dimensional models, as discussed previously, incorporate descriptions of cardiac electrophysiology alongside mechanical deformation [136, 137, 138, 139, 90]. The electrical excitation propagation across cardiac tissue is frequently computed using the monodomain or bidomain equations [140]. The bidomain equation models intracellular and extracellular spaces as distinct but interconnected domains, whereas the monodomain equation approximates these spaces using a single set of equations. While the bidomain equation offers greater accuracy, the monodomain equation can be computationally more efficient and sufficiently accurate for certain applications.

In contrast to these 3-dimensional models, the 0-dimensional CircAdapt model does not explicitly simulate electrical excitation propagation. Various approaches have been employed to determine cardiac wall activation times in both healthy and diseased states. Three-dimensional models created based on magnetic resonance imaging have been employed to compute maps of local electrical excitation times as input for the

CircAdapt model. For ventricular pacing, these maps have previously been generated using an Eikonal model [141] and a cellular automata framework [131]. Furthermore, the electrical excitation maps have been reconstructed using electrocardiographic imaging and used as input for the CircAdapt model [142]. For simulations of AF in a study by Lyon et al. [143], the ventricles were activated synchronously according to patient-specific RR intervals extracted from ECG signals, while the atria did not contract. The study by Lyon et al. [143] also simulated an S1S2 protocol by activating the ventricles at a regular rate, followed by a single RR interval perturbed by $\pm 10\%$, and then resuming the regular rate. Another approach taken by [144] modeled cardiac excitation propagation for the CircAdapt model using a system of coupled automata.

5.2.3 Modeling the Vasculature

Models of the vasculature range in complexity from 0-dimensional to 3-dimensional representations with varying levels of spatial discretization [145, 146]. In *Paper III*, a 0-dimensional lumped parameter model of the vasculature was implemented using an RCRCR Windkessel model to characterize the systemic and pulmonary circulation [147] (Figure 5.1). This RCRCR Windkessel model represents the arterial and venous circulation as an electrical circuit with resistances R and capacitances C, modeling the relationship between upstream pressure P_i and flow rate Q_i and their downstream counterparts P_o and Q_o. Windkessel models have been proposed in different configurations, ranging from the most simplistic RC Windkessel model to more complex configurations using resistances, inductances, and capacitances [148, 145, 129, 146]. Higher resolution vasculature models, such as those in Guala et al. [149], Scarsoglio et al. [132], extend the vasculature to a 1-dimensional representation of the arterial tree. Focusing specifically on aortic blood flow, a 3-dimensional aortic model coupled to a 0-dimensional lumped-parameter model of the left heart and systemic circulation was presented in Deyranlou et al. [150]. A complete pipeline for hemodynamic simulations, encompassing image segmentation, 3-dimensional mesh generation, and hemodynamic simulation, was presented in Updegrove et al. [151].

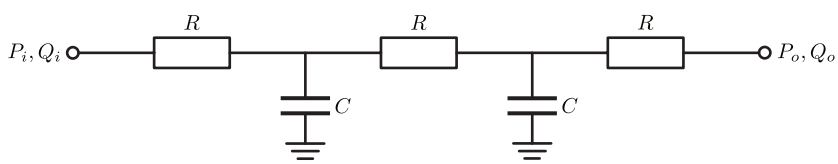

Figure 5.1: Illustration of an RCRCR Windkessel model. C, capacitance; P_i, upstream pressure; P_o, downstream pressure; Q_i, upstream flow-rate; Q_o, downstream flow-rate; R, resistance.

Chapter 6

Summary of Papers

6.1 Paper I: An atrioventricular node model incorporating autonomic tone

This study proposed an extension to an AV node network model presented in Karlsson et al. [119] to investigate the influence of the ANS on AV nodal conduction during AF (Figure 6.1). The aim of *Paper I* was to develop a computational model of the AV node that incorporates changes in autonomic tone and accurately reproduces observed changes in RR series characteristics during tilt testing.

This proposed AV node model is the first to incorporate ANS-induced changes to AV nodal conduction by introducing scaling factors A_R and A_D, which account for the combined influence of sympathetic and parasympathetic activity on the refractory period and conduction delay, respectively, as defined in Eqs. 6.1, 6.2

$$R^P(\Delta t_k) = A_R \left(R^P_{min} + \Delta R^P \left(1 - e^{-\Delta t_k / \tau^P_R} \right) \right) \tag{6.1}$$

$$D^P(\Delta t_k) = A_D \left(D^P_{min} + \Delta D^P e^{-\Delta t_k / \tau^P_D} \right), \tag{6.2}$$

where $P \in \{SP, FP, CN\}$ denotes the pathway. Unlike previous versions of the AV node network model [120, 119], inter-arrival times were modeled using a Pearson Type IV distribution, which was shown to most realistically replicate inter-arrival times observed in atrial fibrillation [152]. To guide the model extension for incorporating ANS-induced changes to AV nodal conduction, a distribution-based sensitivity analysis was conducted [78]. This sensitivity analysis evaluated the relative contributions of atrial activity and AV nodal properties to the ventricular response during AF.

The results demonstrated that changes in atrial activity alone could not fully explain changes in RR series characteristics during tilt testing. The observed trends in RR series characteristics in response to tilt, illustrated in Figure 6.2, demonstrate the effects

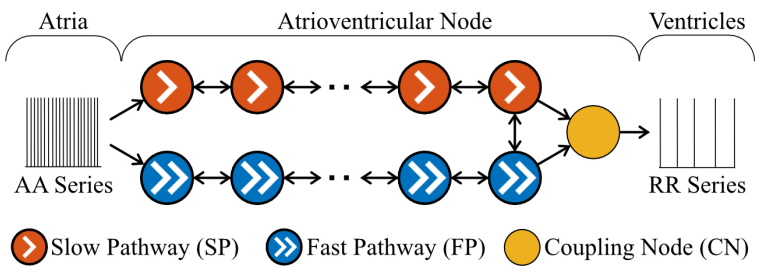

Figure 6.1: A schematic representation of the AV node model. Retrograde conduction is possible within the AV node model. Only a subset of ten nodes in each pathway is shown for simplicity.

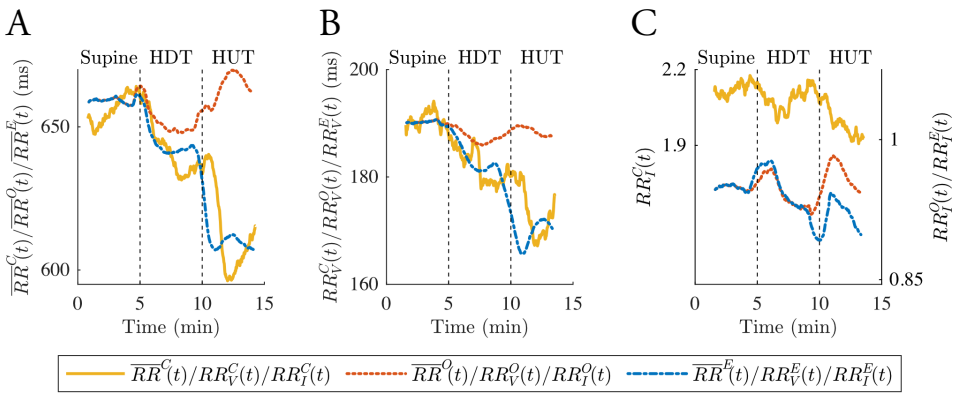

Figure 6.2: Average clinical and simulated RR series characteristic trends for RR mean ($\overline{RR}$), RR rmssd (RR_V), and RR sample entropy (RR_I), including average clinical RR series characteristics (A) $\overline{RR}^C(t)$, (B) $RR_V^C(t)$, and (C) $RR_I^C(t)$ (yellow) and average simulated RR series characteristics for the original model without ANS-induced changes in AV nodal conduction (A) $\overline{RR}^O(t)$, (B) $RR_V^O(t)$, and (C) $RR_I^O(t)$ (red) and average simulated RR series characteristics for the extended model with ANS-induced changes in AV nodal conduction (A) $\overline{RR}^E(t)$, (B) $RR_V^E(t)$, and (C) $RR_I^E(t)$ (blue). The dashed black lines separate the five-minute segments of supine, head-down tilt, and head-up tilt, respectively.

of the scaling factors A_R and A_D on model output, suggesting that combined changes in both refractory period and conduction delay are necessary to achieve agreement with clinical observations.

These findings suggest that ANS-induced changes in AV nodal conduction play a significant role in observed heart rate dynamics during AF. These findings also support the hypothesis that both atrial activity and AV nodal properties contribute to the ventricular response in AF, providing a basis for future patient-specific modeling of autonomic effects on AV nodal function.

6.2 Paper II: ECG-based estimation of respiration-induced autonomic modulation of AV nodal conduction during atrial fibrillation

This study proposed a method for predicting the magnitude of respiration-induced autonomic modulation from ECG-derived features in AF, recognizing the clinical relevance of ANS activity in understanding AF progression and informing personalized treatment. To achieve this prediction, a 1-dimensional convolutional neural network (1D-CNN) was trained using synthetic data generated by a slightly modified AV node model (Figure 6.3) based on the work in *Paper I*.

Methodologically, *Paper II* presents three key innovations. First, the AV node network model was extended to incorporate respiration-induced autonomic modulation by introducing a time-varying scaling factor, $A^P(t)$, affecting AV nodal refractory period and conduction delay within AV nodal pathways $P \in \{SP, FP, CN\}$, as defined in Eqs. 6.3, 6.4

$$R^P\left(\Delta t_k, A^P(t), \boldsymbol{\theta}_R^P\right) = A^P(t)\left(R_{min}^P + \Delta R^P\left(1 - e^{-\Delta t_k/\tau_R^P}\right)\right) \tag{6.3}$$

$$D^P\left(\Delta t_k, A^P(t), \boldsymbol{\theta}_D^P\right) = A^P(t)\left(D_{min}^P + \Delta D^P e^{-\Delta t_k/\tau_D^P}\right). \tag{6.4}$$

This scaling factor, $A^P(t)$, shared by SP and FP was defined as a sinusoidal function with a constant respiratory frequency f_{resp} and peak-to-peak amplitude a_{resp}. The scaling factor for the coupling node (CN) was set to $A^{CN} = 1$ and remained unaffected by respiration. Second, a novel approach was developed for extracting respiration

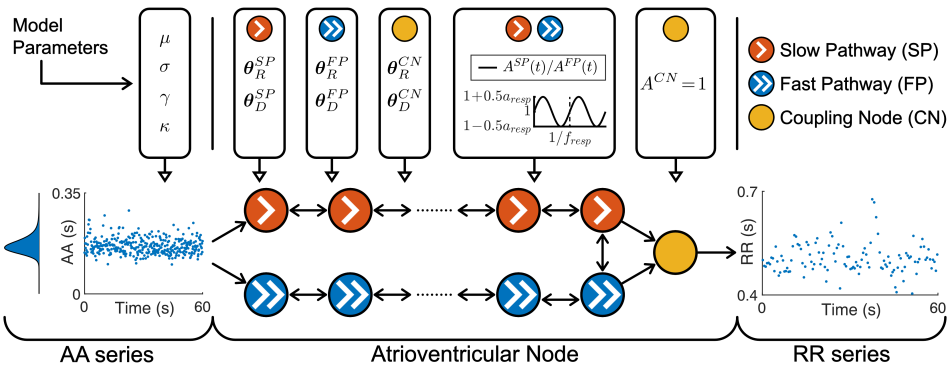

Figure 6.3: A schematic representation of the AV node model. Retrograde conduction is possible within the AV node model. Only a subset of ten nodes in each pathway is shown for simplicity.

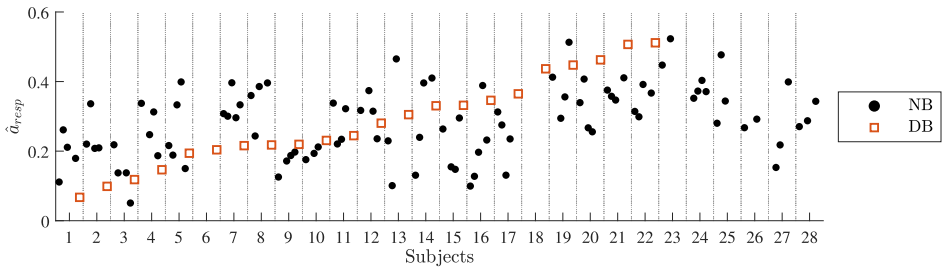

Figure 6.4: Black dots correspond to the estimated $\hat{a}_{resp}$ of 1-min segments during normal breathing (NB), and red squares correspond to $\hat{a}_{resp}$ of 1-min segments during deep breathing (DB).

signals from 12-lead ECG based on periodic component analysis. Third, a 1D-CNN architecture was designed to predict the magnitude of respiration-induced autonomic modulation a_{resp} from ECG-derived time signals. This 1D-CNN was trained on a synthetic dataset comprising RR series, respiration signals, and AFR trends generated from 2 million simulations. The trained 1D-CNN was then evaluated on a separate synthetic dataset generated from 2 million simulations and applied to ECG recordings obtained from AF patients during a deep breathing task to predict a_{resp}.

The results demonstrated that the 1D-CNN could estimate respiration-induced autonomic modulation from RR series alone, with improved estimation accuracy when incorporating respiration signals and AFR. Initial analysis of ECG data from 20 patients performing deep breathing indicated that the a_{resp} prediction is reproducible and sufficiently sensitive to monitor changes and detect individual differences in response to deep breathing. Figure 6.4 illustrates both the inter-patient variability in a_{resp} predictions and the varying responses to deep breathing, with some patients showing increased modulation, others decreased modulation, and some showing no change.

These findings suggest that autonomic modulation during AF can be quantified from standard ECG recordings, potentially providing a new tool for monitoring AF progression. The observed variations in responses to deep breathing within the predictions of respiration-induced autonomic modulation may reflect different stages of autonomic remodeling or AF progression. This work presents a potential avenue for non-invasive monitoring of autonomic function in AF patients, which could potentially support more personalized treatment approaches and a better understanding of AF progression; however, further research is necessary to validate the reproducibility, sensitivity, and clinical significance of a_{resp}.

6.3 Paper III: A computational model to study hemodynamics during atrial fibrillation

This study proposed a computationally efficient model designed to simulate hemodynamics in AF (Figure 6.5). The aim of *Paper III* was to develop a model capable of simulating a sufficient number of cardiac cycles to capture beat-to-beat hemodynamic variability characteristic of irregular AF rhythms while maintaining computational efficiency to permit the generation of sufficient model realizations for robust parameter estimation. This capacity to simulate extended periods of irregular rhythm and generate sufficient realizations was intended to facilitate the investigation of patient-specific AF hemodynamics.

The proposed model combines a mechanical subsystem based on previously published models of cardiac mechanics [123, 128, 130, 131] and vasculature [121, 131], with a novel electrical subsystem that produces atrial and ventricular activation timings characteristic of AF, which are used to initiate contractions in the cardiac wall within the mechanical subsystem. Cardiac walls are divided into multiple patches with distinct electrical activation times, with atrial activation times generated using a Pearson Type IV distribution and ventricular activation times produced with the AV node model described in *Paper I–II*. Patient-specific model parameter calibration was performed using Bayesian history matching with Gaussian process emulators [122], and the model was fitted to data from 17 patients from the SMURF study [153]. The fitted estimates were compared to clinical measurements of arterial and intracardiac pressures in NSR and AF, as well as ejection fractions and cardiac volumes in NSR.

The results demonstrated the ability to fit the computational model to clinical measurements during NSR and AF, with a large majority (75%) of absolute pressure and ejection fraction estimation errors below 9 mmHg and 9% respectively, and a large majority of absolute normalized estimation errors within 1.4 standard deviations of the inter-patient variability. However, the model showed limitations, including underestimating systolic blood pressure during AF and challenges in reproducing minimum pressures in the heart chambers and vessels, resulting in an underestimation of right ventricular diastolic pressure.

Although the model underestimates systolic blood pressure during AF and right ventricular diastolic pressure, indicating a potential area for refinement of the mechanical subsystem, the hemodynamic estimates largely aligned with clinical measurements in both NSR and AF, both in absolute and normalized terms. Moreover, the computational model approach achieved a computational efficiency of 100 simulated heartbeats per second. This model may be useful for predicting patient-specific responses to AF treatments and investigating the relationship between the AF electrical activity and resulting mechanical cardiac function.

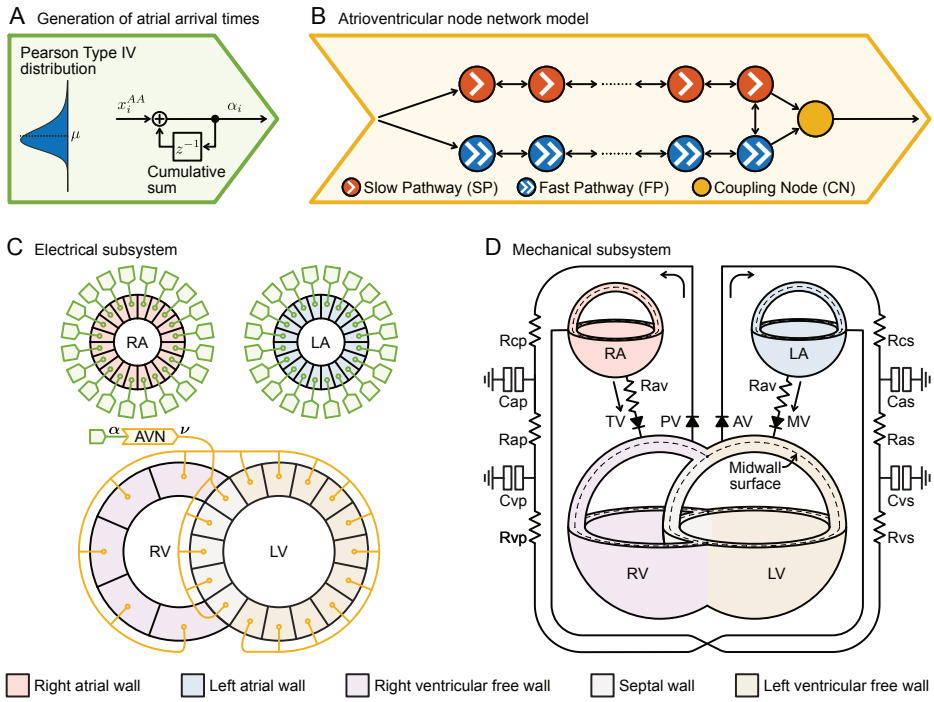

Figure 6.5: Illustration of the computational model of hemodynamics in AF. The model is divided into a subsystem describing cardiac electrical activation times in AF (A-C) and a subsystem describing the cardiovascular mechanics (D).

6.4 Paper IV: Prognostic value of ECG-derived f-wave characteristics from implantable LOOP recorder: Analysis from the LOOP study

This study presents a statistical analysis of the association between ECG-derived f-wave characteristics and clinical outcomes. The aim of *Paper IV* was to investigate the prognostic value of f-wave characteristics derived from implantable loop recorder (ILR) for clinical outcomes in patients at the earliest stages of AF. The investigation focused on three f-wave characteristics: atrial fibrillatory rate (AFR), average amplitude of f-wave envelope (Amp), and an organization index derived from the signal spectral characteristics (ExpDec).

The study cohort comprised 1411 patients without a prior history of AF (54% men, median age 73 years) enrolled in the LOOP study who received ILRs. Patients were stratified into two subgroups based on AF episode duration within the first year following ILR implantation: episodes lasting $\geq$6 minutes and episodes lasting $\geq$60 minutes. The relationship between the f-wave indices and clinical endpoints was assessed using Cox regression analysis, adjusted for common clinical risk factors. These analyses encompassed a primary endpoint (total mortality) and secondary endpoints (a composite of cardiovascular mortality or heart failure and a composite of ischemic stroke or transitory ischemic attack).

The results demonstrated significant associations between lower values of the three f-wave characteristics and an increased risk of total mortality in patients experiencing AF episodes lasting $\geq$60 min (Figure 6.6). Specifically, AFR values below 317 fibrillations per minute, ExpDec values below 1.25, and Amp values below 97.25 were significantly associated with an increased risk of total mortality (Hazard ratio (HR): 2.5, 2.8, and 2.7, respectively). Furthermore, lower values of AFR and ExpDec were associated with an increased risk of the composite endpoint of cardiovascular mortality or heart failure (HR: 4.0 and 3.7, respectively). In patients with AF episodes $\geq$6 minutes, higher AFR was significantly associated with increased risk of total mortality (Hazard ratio (HR): 1.7). Moreover, lower AFR but higher ExpDec and Amp values were significantly associated with increased risk of the composite endpoint of cardiovascular mortality or heart failure (HR: 2.4, 2.6, and 2.5, respectively). Importantly, none of the f-wave indices demonstrated prognostic value for the composite endpoint of ischemic stroke or transitory ischemic attack in the early stages of AF.

These findings suggest that ECG-derived indices of atrial remodeling, particularly AFR, ExpDec and Amp, may facilitate more targeted interventions in the early management of AF. The results indicate a possible association between these f-wave characteristics and the identification of patients at higher risk for total mortality and cardiovascular complications in the early stages of AF.

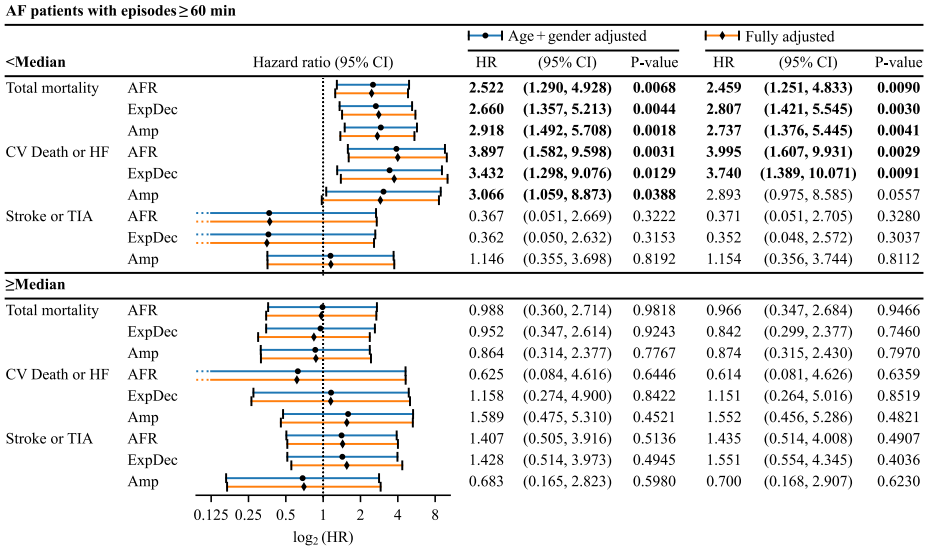

Figure 6.6: Forest plot of Cox proportional hazards model of AFR, ExpDec, and Amp on total mortality, cardiovascular mortality or heart failure (CV Death or HF), and ischemic stroke or transitory ischemic attack (Stroke or TIA) for AF patients with episodes ≥60 min. The top half displays the Cox model of patients with f-wave indices (AFR, ExpDec, Amp) below the population median compared to a reference group without AF, while the bottom half illustrates the model for patients with f-wave indices above the population median. On the right side of the forest plot, the hazard ratio (HR), 95% confidence interval (CI) and P-value are listed for a model adjusted for age and gender (blue) and a model adjusted for age, gender, congestive heart failure, diabetes, hypertension, acute myocardial infarction, and coronary artery bypass graft (orange). A Cox model with P-value<0.05 was presented in bold text.

Chapter 7
Conclusion

In conclusion, contributions have been made to computational modeling and analysis of electrophysiology and hemodynamics during AF, addressing the aims outlined in Section 1.2. The first aim was to develop a computational model of the AV node that replicates patient-specific ANS modulation of AV nodal conduction properties during AF. In *Paper I*, an extension to the AV node model was introduced to replicate the observed changes in heart rate and RR series variability and irregularity during head-up and head-down tilt. The results indicated that the changes in atrial activity alone during tilt were insufficient to replicate the changes in RR series characteristics, suggesting that ANS modulation of the AV node plays an important role. In succession, the AV node model was further refined in *Paper II* by incorporating a time-varying scaling factor to account for respiration-induced autonomic modulation of AV nodal conduction. The proposed model was used to train a CNN to estimate the respiration-induced autonomic modulation based on ECG-derived data. The results suggested that the accuracy of the estimates was sufficiently high to monitor changes and to detect patient-specific differences. Collectively, *Paper I–II* reveal the potential for model-based analysis of autonomic modulation in AV nodal conduction properties based on ECG recordings during AF. By quantifying ANS-induced changes in AV nodal conduction, *Paper I–II* offer a novel methodological approach that could contribute to more personalized AF management. However, a critical limitation remains: the absence of ground-truth data on ANS activity in AF patients constrains the model validation. To advance this research, the necessary validation data in AF patients could be provided by future clinical studies employing novel techniques such as ultrasound micro-neurography [154, 155].

The second aim was to develop a computational model replicating hemodynamics during AF suited for patient-specific model fitting. *Paper III* introduced an integrated computational framework combining an electrical subsystem, incorporating the previously developed AV node model, with a mechanical subsystem comprising a com-

partmental model of the heart and circulation. The computational complexity of the proposed model enabled parallel simulations of 200 irregular cardiac cycles, allowing both the quantification of hemodynamics at an irregular rhythm and patient-specific parameter estimation. The proposed model was fitted to clinical data from 17 patients in the SMURF study, and the results revealed that patient-specific differences in arterial and intracardiac pressures could be replicated. However, the right ventricular diastolic pressure was consistently too low, suggesting the need to refine the circulation system's model description. To address this issue, future research should investigate advanced circulation system models [145, 146] that can be fitted to clinical measurements while accurately replicating minimum pressures across cardiac compartments.

The third aim was to investigate the prognostic value of f-wave characteristics in ECG recordings from implantable loop recorders at the earliest stages of AF. *Paper IV* presented a comprehensive analysis of f-wave characteristics in the LOOP study cohort of 1411 patients and 16538 AF episodes, stratifying patients based on AF episode duration ($\geq$6 min and $\geq$60 min), and systematically evaluated their association with multiple clinical endpoints: total mortality, cardiovascular mortality or heart failure admission, and ischemic stroke or transitory ischemic attack. The statistical analysis revealed that a low AFR, a low organization index derived from the f-wave signal spectral characteristics, and a low average amplitude of the f-wave envelope were associated with increased total mortality and cardiovascular mortality. Conversely, the f-wave characteristics could not predict a higher risk for ischemic stroke or transitory ischemic attack. The findings in *Paper IV* suggest that f-wave analysis can help identify high-risk patients already at the earliest stages of AF, potentially enabling more targeted interventions.

In *Paper III*, the AV node network model was integrated into a computational framework comprising a compartmental model of the heart and circulation, producing realistic atrial and ventricular activation times characteristic of AF. The current hemodynamic model operates as an open loop controller, where the electrical subsystem determines the rate and rhythm of atrial and ventricular contractions in the mechanical subsystem. Future work may extend this model into a closed loop controller, enabling simulated hemodynamics to modulate the electrical subsystem. The ANS, particularly through the arterial baroreceptor reflex, provides the physiological basis for this bidirectional interaction. *Paper I–II* have laid the foundation for incorporating ANS-induced changes in AV nodal conduction properties.

References

[1] J. A. Joglar, M. K. Chung, A. L. Armbruster, E. J. Benjamin, J. Y. Chyou, E. M. Cronin, A. Deswal, L. L. Eckhardt, Z. D. Goldberger, R. Gopinathannair *et al.*, "2023 ACC/AHA/ACCP/HRS Guideline for the Diagnosis and Management of Atrial Fibrillation: A Report of the American College of Cardiology/American Heart Association Joint Committee on Clinical Practice Guidelines," *Journal of the American College of Cardiology*, vol. 83, no. 1, pp. 109–279, 2024.

[2] S. Colilla, A. Crow, W. Petkun, D. E. Singer, T. Singer, and X. Liu, "Estimates of Current and Future Incidence and Prevalence of Atrial Fibrillation in the U.S. Adult Population," *The American Journal of Cardiology*, vol. 112, no. 8, pp. 1142–1147, 2013.

[3] G. Hindricks, T. Potpara, N. Dagres, E. Arbelo, J. J. Bax, C. Blomström-Lundqvist, G. Boriani, M. Castella, G.-A. Dan, P. E. Dilaveris *et al.*, "2020 ESC Guidelines for the diagnosis and management of atrial fibrillation developed in collaboration with the European Association for Cardio-Thoracic Surgery (EACTS): The Task Force for the diagnosis and management of atrial fibrillation of the European Society of Cardiology (ESC) Developed with the special contribution of the European Heart Rhythm Association (EHRA) of the ESC," *European Heart Journal*, vol. 42, no. 5, pp. 373–498, 2020.

[4] S. Nattel and M. Harada, "Atrial remodeling and atrial fibrillation," *Journal of the American College of Cardiology*, vol. 63, no. 22, pp. 2335–2345, 2014.

[5] S. A. George, N. R. Faye, A. Murillo-Berlioz, K. B. Lee, G. D. Trachiotis, and I. R. Efimov, "At the atrioventricular crossroads: dual pathway electrophysiology in the atrioventricular node and its underlying heterogeneities," *Arrhythmia and Electrophysiology Review*, vol. 6, no. 4, pp. 179–185, 2017.

[6] T. Kurian, C. Ambrosi, W. Hucker, V. V. Fedorov, and I. R. Efimov, "Anatomy and electrophysiology of the human AV node," *Pacing and Clinical Electrophysiology*, vol. 33, no. 6, pp. 754–762, 2010.

[7] A. C. Rankin and A. J. Workman, "Rate control in atrial fibrillation: role of atrial inputs to the AV node," *Cardiovascular Research*, vol. 44, no. 2, pp. 249–251, 1999.

[8] J. J. Morris, M. Entman, W. C. North, Y. Kong, and H. McIntosh, "The changes in cardiac output with reversion of atrial fibrillation to sinus rhythm," *Circulation*, vol. 31, no. 5, pp. 670–678, 1965.

[9] W. Shapiro and G. Klein, "Alterations in cardiac function immediately following electrical conversion of atrial fibrillation to normal sinus rhythm," *Circulation*, vol. 38, no. 6, pp. 1074–1084, 1968.

[10] C.-P. Lau, W.-H. Leung, C.-K. Wong, and C.-H. Cheng, "Haemodynamics of induced atrial fibrillation: a comparative assessment with sinus rhythm, atrial and ventricular pacing," *European Heart Journal*, vol. 11, no. 3, pp. 219–224, 1990.

[11] E. Pueyo, R. Bailón, E. Gil, J. P. Martínez, and P. Laguna, "Signal processing guided by physiology: making the most of cardiorespiratory signals," *IEEE Signal Processing Magazin*, vol. 30, no. 5, pp. 136–142, 2013.

[12] M. Stridh, L. Sörnmo, C. J. Meurling, and S. B. Olsson, "Sequential characterization of atrial tachyarrhythmias based on ECG time-frequency analysis," *IEEE Transactions on Biomedical Engineering*, vol. 51, no. 1, pp. 100–114, 2004.

[13] P. G. Platonov, V. D. A. Corino, M. Seifert, F. Holmqvist, and L. Sörnmo, "Atrial fibrillatory rate in the clinical context: natural course and prediction of intervention outcome," *EP Europace*, vol. 16, no. suppl_4, pp. iv110–iv119, 2014.

[14] M. A. Russo, D. M. Santarelli, and D. O'Rourke, "The physiological effects of slow breathing in the healthy human," *Breathe*, vol. 13, no. 4, pp. 298–309, 2017.

[15] C. Varon, J. Morales, J. Lázaro, M. Orini, M. Deviaene, S. Kontaxis, D. Testelmans, B. Buyse, P. Borzée, L. Sörnmo *et al.*, "A comparative study of ECG-derived respiration in ambulatory monitoring using the single-lead ECG," *Scientific Reports*, vol. 10, no. 1, p. 5704, 2020.

[16] J. Heijman, H. Sutanto, H. J. G. M. Crijns, S. Nattel, and N. A. Trayanova, "Computational models of atrial fibrillation: achievements, challenges, and perspectives for improving clinical care," *Cardiovascular Research*, vol. 117, no. 7, pp. 1682–1699, 2021.

[17] N. A. Trayanova, A. Lyon, J. Shade, and J. Heijman, "Computational modeling of cardiac electrophysiology and arrhythmogenesis: toward clinical translation," *Physiological Reviews*, vol. 104, no. 3, pp. 1265–1333, 2024.

[18] S. A. Niederer, J. Lumens, and N. A. Trayanova, "Computational models in cardiology," *Nature Reviews Cardiology*, vol. 16, no. 2, pp. 100–111, 2019.

[19] S. F. Bifulco, N. Akoum, and P. M. Boyle, "Translational applications of computational modelling for patients with cardiac arrhythmias," *Heart*, vol. 107, no. 6, pp. 456–461, 2021.

[20] G. P. Garnett, S. Cousens, T. B. Hallett, R. Steketee, and N. Walker, "Mathematical models in the evaluation of health programmes," *The Lancet*, vol. 378, no. 9790, pp. 515–525, 2011.

[21] R. Sassi, S. Cerutti, F. Lombardi, M. Malik, H. V. Huikuri, C.-K. Peng, G. Schmidt, and Y. Yamamoto, "Advances in heart rate variability signal analysis: joint position statement by the e-Cardiology ESC Working Group and the European Heart Rhythm Association co-endorsed by the Asia Pacific Heart Rhythm Society," *EP Europace*, vol. 17, no. 9, pp. 1341–1353, 2015.

[22] J. C. Greenfield Jr., A. Harley, H. K. Thompson, and A. G. Wallace, "Pressure-flow studies in man during atrial fibrillation," *The Journal of Clinical Investigation*, vol. 47, no. 10, pp. 2411–2421, 1968.

[23] P. G. Platonov, I. Cygankiewicz, M. Stridh, F. Holmqvist, R. Vazquez, A. Bayes-Genis, S. McNitt, W. Zareba, and A. Bayes de Luna, "Low atrial fibrillatory rate is associated with poor outcome in patients with mild to moderate heart failure," *Circulation: Arrhythmia and Electrophysiology*, vol. 5, no. 1, pp. 77–83, 2012.

[24] J. E. Hall and M. E. Hall, *Guyton and Hall Textbook of Medical Physiology, 14th Edition*. Philadelphia, PA 19103-2899: Elsevier – OHCE, 2021.

[25] I. D. Kotadia, J. Whitaker, C. H. Roney, S. Niederer, M. O'Neill, and M. Bishop, "Anisotropic cardiac conduction," *Arrhythmia & Electrophysiology Review*, vol. 9, no. 4, pp. 202–210, 2020.

[26] T. Desplantez, E. Dupont, N. J. Severs, and R. Weingart, "Gap junction channels and cardiac impulse propagation," *Journal of Membrane Biology*, vol. 218, no. 1, pp. 13–28, 2007.

[27] H. Matsukubo, T. Matsuura, N. Endo, J. Asayama, and T. Watanabe, "Echocardiographic measurement of right ventricular wall thickness. A new application of subxiphoid echocardiography," *Circulation*, vol. 56, no. 2, pp. 278–284, 1977.

[28] M. Varela, R. Morgan, A. Theron, D. Dillon-Murphy, H. Chubb, J. Whitaker, M. Henningsson, P. Aljabar, T. Schaeffter, C. Kolbitsch *et al.*, "Novel MRI technique enables non-invasive measurement of atrial wall thickness," *IEEE Transactions on Medical Imaging*, vol. 36, no. 8, pp. 1607–1614, 2017.

[29] J. Walpot, D. Juneau, S. Massalha, G. Dwivedi, F. J. Rybicki, B. J. Chow, and J. a. R. Inácio, "Left ventricular mid-diastolic wall thickness: normal values for coronary CT angiography," *Radiology: Cardiothoracic Imaging*, vol. 1, no. 5, p. e190034, 2019.

[30] S. Nattel and L. Carlsson, "Innovative approaches to anti-arrhythmic drug therapy," *Nature Reviews Drug Discovery*, vol. 5, no. 12, pp. 1034–1049, 2006.

[31] M. E. Mangoni and J. Nargeot, "Genesis and regulation of the heart automaticity," *Physiological Reviews*, vol. 88, no. 3, pp. 919–982, 2008.

[32] J. Billette and R. Tadros, "An integrated overview of AV node physiology," *Pacing and Clinical Electrophysiology*, vol. 42, no. 7, pp. 805–820, 2019.

[33] M. J. Shen and D. P. Zipes, "Role of the autonomic nervous system in modulating cardiac arrhythmias," *Circulation Research*, vol. 114, no. 6, pp. 1004–1021, 2014.

[34] G. Giannino, V. Braia, C. Griffith Brookles, F. Giacobbe, F. D'Ascenzo, F. Angelini, A. Saglietto, G. M. De Ferrari, and V. Dusi, "The intrinsic cardiac nervous system: from pathophysiology to therapeutic implications," *Biology*, vol. 13, no. 2, p. 105, 2024.

[35] J. W. Lister, E. Stein, B. D. Kosowsky, S. H. Lau, and A. N. Damato, "Atrioventricular conduction in man: effect of rate, exercise, isoproterenol and atropine on the P-R interval," *The American Journal of Cardiology*, vol. 16, no. 4, pp. 516–523, 1965.

[36] R. C. Dhingra, E. Winslow, J. M. Pouget, S. H. Rahimtoola, and K. M. Rosen, "The effect of isoproterenol on atrioventricular and intraventricular conduction," *The American Journal of Cardiology*, vol. 32, no. 5, pp. 629–636, 1973.

[37] F. Morady, S. D. Nelson, W. H. Kou, R. Pratley, S. Schmaltz, M. De Buitleir, and J. B. Halter, "Electrophysiologic effects of epinephrine in humans," *Journal of the American College of Cardiology*, vol. 11, no. 6, pp. 1235–1244, 1988.

[38] S. F. Cossú, S. A. Rothman, I. L. Chmielewski, H. H. Hsia, R. L. Vogel, J. M. Miller, and A. E. Buxton, "The effects of isoproterenol on the cardiac conduction system," *Journal of Cardiovascular Electrophysiology*, vol. 8, no. 8, pp. 847–853, 1997.

[39] R. Furlan, A. Porta, F. Costa, J. Tank, L. Baker, R. Schiavi, D. Robertson, A. Malliani, and R. Mosqueda-Garcia, "Oscillatory patterns in sympathetic neural discharge and cardiovascular variables during orthostatic stimulus," *Circulation*, vol. 101, no. 8, pp. 886–892, 2000.

[40] T. Hashimoto, M. Fukatani, M. Mori, and K. Hashiba, "Effects of standing on the induction of paroxysmal supraventricular tachycardia," *Journal of the American College of Cardiology*, vol. 17, no. 3, pp. 690–695, 1991.

[41] P. Martin, "The influence of the parasympathetic nervous system on atrioventricular conduction," *Circulation Research*, vol. 41, no. 5, pp. 593–599, 1977.

[42] P. Katona, J. Poitras, G. Barnett, and B. Terry, "Cardiac vagal efferent activity and heart period in the carotid sinus reflex," *American Journal of Physiology*, vol. 218, no. 4, pp. 1030–1037, 1970.

[43] V. Y. H. van Weperen, C. M. Ripplinger, and M. Vaseghi, "Autonomic control of ventricular function in health and disease: current state of the art," *Clinical Autonomic Research*, vol. 33, no. 4, pp. 491–517, 2023.

[44] L. Sörnmo, *Atrial fibrillation from an engineering perspective*. Springer Cham, 2018.

[45] J. E. P. Waktare, "Atrial fibrillation," *Circulation*, vol. 106, no. 1, pp. 14–16, 2002.

[46] U. Schotten, S. Verheule, P. Kirchhof, and A. Goette, "Pathophysiological Mechanisms of Atrial Fibrillation: A Translational Appraisal," *Physiological Reviews*, vol. 91, no. 1, pp. 265–325, 2011.

[47] J. Heijman, N. Voigt, S. Ghezelbash, I. Schirmer, and D. Dobrev, "Calcium handling abnormalities as a target for atrial fibrillation therapeutics: how close to clinical implementation?" *Journal of Cardiovascular Pharmacology*, vol. 66, no. 6, pp. 515–522, 15.

[48] S. Makary, N. Voigt, A. Maguy, R. Wakili, K. Nishida, M. Harada, D. Dobrev, and S. Nattel, "Differential protein kinase C isoform regulation and increased constitutive activity of acetylcholine-regulated potassium channels in atrial remodeling," *Circulation Research*, vol. 109, no. 9, pp. 1031–1043, 2011.

[49] M. C. Wijffels, C. J. Kirchhof, R. Dorland, and M. A. Allessie, "Atrial Fibrillation Begets Atrial Fibrillation," *Circulation*, vol. 92, no. 7, pp. 1954–1968, 1995.

[50] M. A. Allessie, "Atrial Electrophysiologic Remodeling: Another Vicious Circle?" *Journal of Cardiovascular Electrophysiology*, vol. 9, no. 12, pp. 1378–1393, 1998.

[51] L. Yue, P. Melnyk, R. Gaspo, Z. Wang, and S. Nattel, "Molecular mechanisms underlying ionic remodeling in a dog model of atrial fibrillation," *Circulation Research*, vol. 84, no. 7, pp. 776–784, 1999.

[52] P. S. Cunha, S. Laranjo, J. Heijman, and M. M. Oliveira, "The atrium in atrial fibrillation – A clinical review on how to manage atrial fibrotic substrates," *Frontiers in Cardiovascular Medicine*, vol. 9, no. 879984, 2022.

[53] R. Wakili, N. Voigt, S. Kääb, D. Dobrev, and S. Nattel, "Recent advances in the molecular pathophysiology of atrial fibrillation," *The Journal of Clinical Investigation*, vol. 121, no. 8, pp. 2955–2968, 2011.

[54] S. V. Pandit and J. Jalife, "Rotors and the dynamics of cardiac fibrillation," *Circulation Research*, vol. 112, no. 5, pp. 849–862, 2013.

[55] G. F. Michaud and W. G. Stevenson, "Atrial fibrillation," *New England Journal of Medicine*, vol. 384, no. 4, pp. 353–361, 2021.

[56] L. Azzolin, M. Eichenlaub, C. Nagel, D. Nairn, J. Sanchez, L. Unger, O. Dössel, A. Jadidi, and A. Loewe, "Personalized ablation vs. conventional ablation strategies to terminate atrial fibrillation and prevent recurrence," *EP Europace*, vol. 25, no. 1, pp. 211–222, 2022.

[57] F. Nilsson, M. Stridh, A. Bollmann, and L. Sörnmo, "Predicting spontaneous termination of atrial fibrillation using the surface ECG," *Medical Engineering & Physics*, vol. 28, no. 8, pp. 802–808, 2006.

[58] S. Petrutiu, A. V. Sahakian, and S. Swiryn, "Abrupt changes in fibrillatory wave characteristics at the termination of paroxysmal atrial fibrillation in humans," *EP Europace*, vol. 9, no. 7, pp. 466–470, 2007.

[59] M. B. Choudhary, F. Holmqvist, J. Carlson, H.-J. Nilsson, A. Roijer, and P. G. Platonov, "Low atrial fibrillatory rate is associated with spontaneous conversion of recent-onset atrial fibrillation," *EP Europace*, vol. 15, no. 10, pp. 1445–1452, 2013.

[60] I. Nault, N. Lellouche, S. Matsuo, S. Knecht, M. Wright, K.-T. Lim, F. Sacher, P. Platonov, A. Deplagne, P. Bordachar *et al.*, "Clinical value of fibrillatory wave amplitude on surface ECG in patients with persistent atrial fibrillation," *Journal of Interventional Cardiac Electrophysiology*, vol. 26, no. 1, pp. 11–19, 2009.

[61] F. Squara, D. Scarlatti, S.-S. Bun, P. Moceri, E. Ferrari, O. Meste, and V. Zarzoso, "Fibrillatory wave amplitude evolution during persistent atrial fibrillation ablation: implications for atrial substrate and fibrillation complexity assessment," *Journal of Clinical Medicine*, vol. 11, no. 15, p. 4519, 2002.

[62] M. Stridh and L. Sörnmo, "Spatiotemporal QRST cancellation techniques for analysis of atrial fibrillation," *IEEE Transactions on Biomedical Engineering*, vol. 48, no. 1, pp. 105–111, 2001.

[63] M. Holm, S. Pehrson, M. Ingemansson, L. Sörnmo, R. Johansson, L. Sandhall, M. Sunemark, B. Smideberg, C. Olsson, and S. Olsson, "Non-invasive assessment of the atrial cycle length during atrial fibrillation in man: introducing, validating and illustrating a new ECG method," *Cardiovascular Research*, vol. 38, no. 1, pp. 69–81, 1998.

[64] M. Henriksson, A. Petrėnas, V. Marozas, F. Sandberg, and L. Sörnmo, "Model-based assessment of f-wave signal quality in patients with atrial fibrillation," *IEEE Transactions on Biomedical Engineering*, vol. 65, no. 11, pp. 2600–2611, 2018.

[65] M. Abdollahpur, G. Engström, P. G. Platonov, and F. Sandberg, "A subspace projection approach to quantify respiratory variations in the f-wave frequency trend," *Frontiers in Physiology*, vol. 13, no. 976925, 2022.

[66] M. Meo, V. Zarzoso, O. Meste, D. G. Latcu, and N. Saoudi, "Spatial variability of the 12-lead surface ECG as a tool for noninvasive prediction of catheter ablation outcome in persistent atrial fibrillation," *IEEE Transactions on Biomedical Engineering*, vol. 60, no. 1, pp. 20–27, 2013.

[67] F. Holmqvist, M. Stridh, J. E. Waktare, A. Roijer, L. Sörnmo, P. G. Platonov, and C. J. Meurling, "Atrial fibrillation signal organization predicts sinus rhythm maintenance in patients undergoing cardioversion of atrial fibrillation," *EP Europace*, vol. 8, no. 8, pp. 559–565, 2006.

[68] N. Pilia, C. Nagel, G. Lenis, S. Becker, O. Dössel, and A. Loewe, "ECGdeli - An open source ECG delineation toolbox for MATLAB," *SoftwareX*, vol. 13, p. 100639, 2021.

[69] J. S. Richman and J. R. Moorman, "Physiological time-series analysis using approximate entropy and sample entropy," *American Journal of Physiology-Heart and Circulatory Physiology*, vol. 278, no. 6, pp. H2039–H2049, 2000.

[70] D. D. McManus, J. Lee, O. Maitas, N. Esa, R. Pidikiti, A. Carlucci, J. Harrington, E. Mick, and K. H. Chon, "A novel application for the detection of an irregular pulse using an iPhone 4S in patients with atrial fibrillation," *Heart Rhythm*, vol. 10, no. 3, pp. 315–319, 2013.

[71] V. D. Corino, S. R. Ulimoen, S. Enger, L. T. Mainardi, A. Tveit, and P. G. Platonov, "Rate-control drugs affect variability and irregularity measures of RR intervals in patients with permanent atrial fibrillation," *Journal of Cardiovascular Electrophysiology*, vol. 26, no. 2, pp. 137–141, 2015.

[72] E. E. Solís-Montufar, G. Gálvez-Coyt, and A. Muñoz-Diosdado, "Entropy analysis of RR-time series from stress tests," *Frontiers in Physiology*, vol. 11, 2020.

[73] P. H. Charlton, D. A. Birrenkott, T. Bonnici, M. A. F. Pimentel, A. E. W. Johnson, J. Alastruey, L. Tarassenko, P. J. Watkinson, R. Beale, and D. A. Clifton, "Breathing rate estimation from the electrocardiogram and photoplethysmogram: A review," *IEEE Reviews in Biomedical Engineering*, vol. 11, pp. 2–20, 2018.

[74] S. Kontaxis, J. Lázaro, V. D. A. Corino, F. Sandberg, R. Bailón, P. Laguna, and L. Sörnmo, "ECG-Derived Respiratory Rate in Atrial Fibrillation," *IEEE Transactions on Biomedical Engineering*, vol. 67, no. 3, pp. 905–914, 2020.

[75] F. N. Fritsch and R. E. Carlson, "Monotone piecewise cubic interpolation," *SIAM Journal on Numerical Analysis*, vol. 17, no. 2, pp. 238–246, 1980.

[76] A. Saltelli, K. Aleksankina, W. Becker, P. Fennell, F. Ferretti, N. Holst, S. Li, and Q. Wu, "Why so many published sensitivity analyses are false: A systematic

review of sensitivity analysis practices," *Environmental Modelling & Software*, vol. 114, pp. 29–39, 2019.

[77] I. Sobol, "Global sensitivity indices for nonlinear mathematical models and their Monte Carlo estimates," *Mathematics and Computers in Simulation*, vol. 55, no. 1, pp. 271–280, 2001.

[78] F. Pianosi and T. Wagener, "Distribution-based sensitivity analysis from a generic input-output sample," *Environmental Modelling & Software*, vol. 108, pp. 197–207, 2018.

[79] A. H. Ribeiro, M. H. Ribeiro, G. M. M. Paixão, D. M. Oliveira, P. R. Gomes, J. A. Canazart, M. P. S. Ferreira, C. R. Andersson, P. W. Macfarlane, W. Meira Jr. *et al.*, "Automatic diagnosis of the 12-lead ECG using a deep neural network," *Nature Communications*, vol. 11, no. 1, p. 1760, 2020.

[80] V. Nair and G. E. Hinton, "Rectified linear units improve restricted boltzmann machines," in *Proceedings of the 27th International Conference on International Conference on Machine Learning*, ser. ICML'10. Madison, WI, USA: Omnipress, 2010, p. 807–814.

[81] S. Ioffe and C. Szegedy, "Batch normalization: accelerating deep network training by reducing internal covariate shift," in *Proceedings of the 32nd International Conference on International Conference on Machine Learning - Volume 37*, ser. ICML'15. JMLR.org, 2015, p. 448–456.

[82] J. Ranstam and J. A. Cook, "Kaplan–Meier curve," *British Journal of Surgery*, vol. 104, no. 4, pp. 442–442, 2017.

[83] E. L. Kaplan and P. Meier, "Nonparametric Estimation from Incomplete Observations," *Journal of the American Statistical Association*, vol. 53, p. 282, 1958.

[84] G. James, D. Witten, T. Hastie, R. Tibshirani, and J. Taylor, *An introduction to statistical learning with applications in python*. Springer Cham, 2023.

[85] Y. Rudy and J. R. Silva, "Computational biology in the study of cardiac ion channels and cell electrophysiology," *Quarterly Reviews of Biophysics*, vol. 39, no. 1, pp. 57–116, 2006.

[86] A. P. Benson, H. J. Stevenson-Cocks, D. G. Whittaker, E. White, and M. A. Colman, "Multi-scale approaches for the simulation of cardiac electrophysiology: II – tissue-level structure and function," *Methods*, vol. 185, pp. 60–81, 2021.

[87] R. H. Clayton, "Computational models of normal and abnormal action potential propagation in cardiac tissue: linking experimental and clinical cardiology," *Physiological Measurement*, vol. 22, no. 3, p. R15, 2001.

[88] P.-C. Yang, A. Rose, K. R. DeMarco, J. R. D. Dawson, Y. Han, M.-T. Jeng, R. D. Harvey, L. F. Santana, C. M. Ripplinger, I. Vorobyov *et al.*, "A multiscale predictive digital twin for neurocardiac modulation," *The Journal of Physiology*, vol. 601, no. 17, pp. 3789–3812, 2023.

[89] K. Gillette, M. A. Gsell, A. J. Prassl, E. Karabelas, U. Reiter, G. Reiter, T. Grandits, C. Payer, D. Štern, M. Urschler *et al.*, "A framework for the generation of digital twins of cardiac electrophysiology from clinical 12-leads ECGs," *Medical Image Analysis*, vol. 71, p. 102080, 2021.

[90] M. Fedele, R. Piersanti, F. Regazzoni, M. Salvador, P. C. Africa, M. Bucelli, A. Zingaro, L. Dede', and A. Quarteroni, "A comprehensive and biophysically detailed computational model of the whole human heart electromechanics," *Computer Methods in Applied Mechanics and Engineering*, vol. 410, p. 115983, 2023.

[91] E. M. Wülfers, R. Moss, H. Lehrmann, T. Arentz, D. Westermann, G. Seemann, K. E. Odening, and J. Steinfurt, "Whole-heart computational modelling provides further mechanistic insights into ST-elevation in Brugada syndrome," *IJC Heart & Vasculature*, vol. 51, p. 101373, 2024.

[92] T. Gerach and A. Loewe, "Differential effects of mechano-electric feedback mechanisms on whole-heart activation, repolarization, and tension," *The Journal of Physiology*, vol. 602, no. 18, pp. 4605–4624, 2024.

[93] R. J. Cohen, R. D. Berger, and T. E. Dushane, "A quantitative model for the ventricular response during atrial fibrillation," *IEEE Transactions on Biomedical Engineering*, vol. BME-30, no. 12, pp. 769–781, 1983.

[94] L. Mangin, A. Vinet, P. Pagé, and L. Glass, "Effects of antiarrhythmic drug therapy on atrioventricular nodal function during atrial fibrillation in humans," *EP Europace*, vol. 7, no. s2, pp. S71–S82, 2005.

[95] J. Lian, D. Müssig, and V. Lang, "Computer modeling of ventricular rhythm during atrial fibrillation and ventricular pacing," *IEEE Transactions on Biomedical Engineering*, vol. 53, no. 8, pp. 1512–1520, 2006.

[96] V. D. Corino, F. Sandberg, L. T. Mainardi, and L. Sörnmo, "An atrioventricular node model for analysis of the ventricular response during atrial fibrillation,"

IEEE Transactions on Biomedical Engineering, vol. 58, no. 12, pp. 3386–3395, 2011.

[97] V. D. Corino, F. Sandberg, F. Lombardi, L. T. Mainardi, and L. Sörnmo, "Atrioventricular nodal function during atrial fibrillation: Model building and robust estimation," *Biomedical Signal Processing and Control*, vol. 8, no. 6, pp. 1017–1025, 2013.

[98] M. Masè, M. Marini, M. Disertori, and F. Ravelli, "Dynamics of AV coupling during human atrial fibrillation: role of atrial rate," *American Journal of Physiology-Heart and Circulatory Physiology*, vol. 309, no. 1, pp. H198–H205, 2015.

[99] M. Henriksson, V. D. A. Corino, L. Sörnmo, and F. Sandberg, "A statistical atrioventricular node model accounting for pathway switching during atrial fibrillation," *IEEE Transactions on Biomedical Engineering*, vol. 63, no. 9, pp. 1842–1849, 2016.

[100] M. Kawato, A. Yamanaka, S. Urushibara, O. Nagata, H. Irisawa, and R. Suzuki, "Simulation analysis of excitation conduction in the heart: Propagation of excitation in different tissues," *Journal of Theoretical Biology*, vol. 120, no. 4, pp. 389–409, 1986.

[101] S. Urushibara, M. Kawato, K. Nakazawa, and R. Suzuki, "Simulation analysis of conduction of excitation in the atrioventricular node," *Journal of Theoretical Biology*, vol. 126, no. 3, pp. 275–288, 1987.

[102] A.-R. LeBlanc and B. Dubé, "Propagation in the AV node: A model based on a simplified two-dimensional structure and a bidomain tissue representation," *Medical and Biological Engineering and Computing*, vol. 31, no. 6, pp. 545–556, 1993.

[103] J. C. Hancox, K. H. Yuill, J. S. Mitcheson, and M. K. Convery, "Progress and gaps in understanding the electrophysiological properties of morphologically normal cells from the cardiac atrioventricular node," *International Journal of Bifurcation and Chaos*, vol. 13, no. 12, pp. 3675–3691, 2003.

[104] S. Inada, J. Hancox, H. Zhang, and M. Boyett, "One-dimensional mathematical model of the atrioventricular node including atrio-nodal, nodal, and nodal-His cells," *Biophysical Journal*, vol. 97, no. 8, pp. 2117–2127, 2009.

[105] P. Podziemski and J. J. Żebrowski, "A simple model of the right atrium of the human heart with the sinoatrial and atrioventricular nodes included," *Journal of Clinical Monitoring and Computing*, vol. 27, no. 4, pp. 481–498, 2013.

[106] J. Li, S. Inada, J. E. Schneider, H. Zhang, H. Dobrzynski, and M. R. Boyett, "Three-dimensional computer model of the right atrium including the sinoatrial and atrioventricular nodes predicts classical nodal behaviours," *PLOS ONE*, vol. 9, no. 11, pp. 1–18, 2014.

[107] C. Schölzel, V. Blesius, G. Ernst, A. Goesmann, and A. Dominik, "Countering reproducibility issues in mathematical models with software engineering techniques: A case study using a one-dimensional mathematical model of the atrioventricular node," *PLOS ONE*, vol. 16, no. 7, p. e0254749, 2021.

[108] C. Bartolucci, P. Mesirca, E. Ricci, C. Sales-Bellés, E. Torre, J. Louradour, M. E. Mangoni, and S. Severi, "Computational modelling of mouse atrio ventricular node action potential and automaticity," *The Journal of Physiology*, vol. 602, no. 19, pp. 4821–4847, 2024.

[109] J. Billette and R. Tadros, "Integrated rate-dependent and dual pathway AV nodal functions: principles and assessment framework," *American Journal of Physiology-Heart and Circulatory Physiology*, vol. 306, no. 2, pp. H173–H183, 2014.

[110] L. Dorveaux, W. Heddle, M. Jones, and A. Tonkin, "Comparison of exponential and hyperbolic models of conduction through the atrioventricular node," *International Journal of Bio-Medical Computing*, vol. 17, no. 3, pp. 227–235, 1985.

[111] L. Dorveaux and A. Tonkin, "A comprehensive model describing conduction through the atrioventricular node," *International Journal of Bio-Medical Computing*, vol. 18, no. 3, pp. 261–271, 1986.

[112] L. Dorveaux, N. Twidale, and A. Tonkin, "Direct identification of parameters in a mathematical model describing conduction through the atrioventricular node," *International Journal of Bio-Medical Computing*, vol. 23, pp. 69–76, 1988.

[113] J. Sun, F. Amellal, L. Glass, and J. Billette, "Alternans and period-doubling bifurcations in atrioventricular nodal conduction," *Journal of Theoretical Biology*, vol. 173, no. 1, pp. 79–91, 1995.

[114] A. M. Climent, M. S. Guillem, Y. Zhang, J. Millet, and T. N. Mazgalev, "Functional mathematical model of dual pathway AV nodal conduction," *American Journal of Physiology-Heart and Circulatory Physiology*, vol. 300, no. 4, pp. H1393–H1401, 2011.

[115] F. Sandberg, M. Stridh, and L. Sörnmo, "Frequency tracking of atrial fibrillation using hidden markov models," *IEEE Transactions on Biomedical Engineering*, vol. 55, no. 2, pp. 502–511, 2008.

[116] V. D. Corino, F. Sandberg, P. G. Platonov, L. T. Mainardi, S. R. Ulimoen, S. Enger, A. Tveit, and L. Sörnmo, "Non-invasive evaluation of the effect of metoprolol on the atrioventricular node during permanent atrial fibrillation," *EP Europace*, vol. 16, no. suppl_4, pp. iv129–iv134, 2014.

[117] F. Sandberg, V. D. Corino, L. T. Mainardi, S. R. Ulimoen, S. Enger, A. Tveit, P. G. Platonov, and L. Sörnmo, "Non-invasive assessment of the effect of beta blockers and calcium channel blockers on the AV node during permanent atrial fibrillation," *Journal of Electrocardiology*, vol. 48, no. 5, pp. 861–866, 2015.

[118] V. D. Corino, F. Sandberg, L. T. Mainardi, P. G. Platonov, and L. Sörnmo, "Noninvasive assessment of atrioventricular nodal function: Effect of rate-control drugs during atrial fibrillation," *Annals of Noninvasive Electrocardiology*, vol. 20, no. 6, pp. 534–541, 2015.

[119] M. Karlsson, F. Sandberg, S. R. Ulimoen, and M. Wallman, "Non-invasive characterization of human AV-nodal conduction delay and refractory period during atrial fibrillation," *Frontiers in Physiology*, vol. 12, no. 728955, 2021.

[120] M. Wallman and F. Sandberg, "Characterisation of human AV-nodal properties using a network model," *Medical & Biological Engineering & Computing*, vol. 56, pp. 247–259, 2018.

[121] W. P. Santamore and D. Burkhoff, "Hemodynamic consequences of ventricular interaction as assessed by model analysis," *American Journal of Physiology-Heart and Circulatory Physiology*, vol. 260, no. 1, pp. H146–H157, 1991.

[122] C. E. Jones and P. J. Oomen, "Synergistic biophysics and machine learning modeling to rapidly predict cardiac growth probability," *Computers in Biology and Medicine*, vol. 184, p. 109323, 2025.

[123] T. Arts, T. Delhaas, P. Bovendeerd, X. Verbeek, and F. W. Prinzen, "Adaptation to mechanical load determines shape and properties of heart and circulation: the CircAdapt model," *American Journal of Physiology-Heart and Circulatory Physiology*, vol. 288, no. 4, pp. H1943–H1954, 2005.

[124] G. Palau-Caballero, J. Walmsley, J. Gorcsan, J. Lumens, and T. Delhaas, "Abnormal ventricular and aortic wall properties can cause inconsistencies in grading

aortic regurgitation severity: a computer simulation study," *Journal of the American Society of Echocardiography*, vol. 29, no. 11, pp. 1122–1130.e4, 2016.

[125] M. Žáček and E. Kraus, "Numerical simulation of the blood flow in the human cardiovascular system," *Journal of Biomechanics*, vol. 29, no. 1, pp. 13–20, 1996.

[126] Y. Shi, T. J. Yeo, and Y. Zhao, "Numerical simulation of a systemic flow test rig," *ASAIO Journal*, vol. 50, no. 1, pp. 54–64, 2004.

[127] T. Korakianitis and Y. Shi, "Numerical simulation of cardiovascular dynamics with healthy and diseased heart valves," *Journal of Biomechanics*, vol. 39, no. 11, pp. 1964–1982, 2006.

[128] J. Lumens, T. Delhaas, B. Kirn, and T. Arts, "Three-wall segment (TriSeg) model describing mechanics and hemodynamics of ventricular interaction," *Annals of Biomedical Engineering*, vol. 37, no. 11, pp. 2234–2255, 2009.

[129] S. Scarsoglio, A. Guala, C. Camporeale, and L. Ridolfi, "Impact of atrial fibrillation on the cardiovascular system through a lumped-parameter approach," *Medical & Biological Engineering & Computing*, vol. 52, no. 11, pp. 905–920, 2014.

[130] J. Walmsley, T. Arts, N. Derval, P. Bordachar, H. Cochet, S. Ploux, F. W. Prinzen, T. Delhaas, and J. Lumens, "Fast simulation of mechanical heterogeneity in the electrically asynchronous heart using the MultiPatch module," *PLOS Computational Biology*, vol. 11, no. 7, pp. 1–23, 2015.

[131] P. J. A. Oomen, T.-K. N. Phung, S. H. Weinberg, K. C. Bilchick, and J. W. Holmes, "A rapid electromechanical model to predict reverse remodeling following cardiac resynchronization therapy," *Biomechanics and Modeling in Mechanobiology*, vol. 21, no. 1, pp. 231–247, 2022.

[132] S. Scarsoglio, C. Gallo, and L. Ridolfi, "Effects of atrial fibrillation on the arterial fluid dynamics: a modelling perspective," *Meccanica*, vol. 53, no. 13, pp. 3251–3267, 2018.

[133] K. Sagawa, "The ventricular pressure-volume diagram revisited," *Circulation Research*, vol. 43, no. 5, pp. 677–687, 1978.

[134] H. Suga, "Theoretical analysis of a left-ventricular pumping model based on the systolic time-varying pressure/volume ratio," *IEEE Transactions on Biomedical Engineering*, vol. BME-18, no. 1, pp. 47–55, 1971.

[135] T. Korakianitis and Y. Shi, "A concentrated parameter model for the human cardiovascular system including heart valve dynamics and atrioventricular interaction," *Medical Engineering & Physics*, vol. 28, no. 7, pp. 613–628, 2006.

[136] C. M. Augustin, A. Neic, M. Liebmann, A. J. Prassl, S. A. Niederer, G. Haase, and G. Plank, "Anatomically accurate high resolution modeling of human whole heart electromechanics: A strongly scalable algebraic multigrid solver method for nonlinear deformation," *Journal of Computational Physics*, vol. 305, pp. 622–646, 2016.

[137] C. M. Augustin, M. A. Gsell, E. Karabelas, E. Willemen, F. W. Prinzen, J. Lumens, E. J. Vigmond, and G. Plank, "A computationally efficient physiologically comprehensive 3D–0D closed-loop model of the heart and circulation," *Computer Methods in Applied Mechanics and Engineering*, vol. 386, p. 114092, 2021.

[138] T. Gerach, S. Schuler, J. Fröhlich, L. Lindner, E. Kovacheva, R. Moss, E. M. Wülfers, G. Seemann, C. Wieners, and A. Loewe, "Electro-mechanical whole-heart digital twins: a fully coupled multi-physics approach," *Mathematics*, vol. 9, no. 11, p. 1247, 2021.

[139] R. Moss, E. M. Wülfers, S. Schuler, A. Loewe, and G. Seemann, "A fully-coupled electro-mechanical whole-heart computational model: influence of cardiac contraction on the ECG," *Frontiers in Physiology*, vol. 12, no. 778872, 2021.

[140] B. F. Nielsen, T. S. Ruud, G. T. Lines, and A. Tveito, "Optimal monodomain approximations of the bidomain equations," *Applied Mathematics and Computation*, vol. 184, no. 2, pp. 276–290, 2007.

[141] R. Meiburg, J. H. J. Rijks, A. S. Beela, E. Bressi, D. Grieco, T. Delhaas, J. G. L. Luermans, F. W. Prinzen, K. Vernooy, and J. Lumens, "Comparison of novel ventricular pacing strategies using an electro-mechanical simulation platform," *EP Europace*, vol. 25, no. 6, p. euad144, 2023.

[142] J. Lumens, S. Ploux, M. Strik, J. Gorcsan, H. Cochet, N. Derval, M. Strom, C. Ramanathan, P. Ritter, M. Haïssaguerre *et al.*, "Comparative electromechanical and hemodynamic effects of left ventricular and biventricular pacing in dyssynchronous heart failure: electrical resynchronization versus left–right ventricular interaction," *Journal of the American College of Cardiology*, vol. 62, no. 25, pp. 2395–2403, 2013.

[143] A. Lyon, M. van Mourik, L. Cruts, J. Heijman, S. C. A. M. Bekkers, U. Schotten, H. J. G. M. Crijns, D. Linz, and J. Lumens, "Both beat-to-beat changes in

RR-interval and left ventricular filling time determine ventricular function during atrial fibrillation," *EP Europace*, vol. 23, no. Supplement_1, pp. i21–i28, 2021.

[144] M. Taconné, K. P. Owashi, E. Galli, J. Duchenne, A. Hubert, E. Donal, A. I. Hernàndez, and V. Le Rolle, "Model-based analysis of myocardial strains in left bundle branch block," *Frontiers in Applied Mathematics and Statistics*, vol. 8, no. 833003, 2022.

[145] Y. Shi, P. Lawford, and R. Hose, "Review of zero-D and 1-D models of blood flow in the cardiovascular system," *BioMedical Engineering OnLine*, vol. 10, no. 33, 2011.

[146] S. Zhou, L. Xu, L. Hao, H. Xiao, Y. Yao, L. Qi, and Y. Yao, "A review on low-dimensional physics-based models of systemic arteries: application to estimation of central aortic pressure," *BioMedical Engineering OnLine*, vol. 18, no. 41, 2019.

[147] D. Burkhoff and J. V. Tyberg, "Why does pulmonary venous pressure rise after onset of LV dysfunction: a theoretical analysis," *American Journal of Physiology-Heart and Circulatory Physiology*, vol. 265, no. 5, pp. H1819–H1828, 1993.

[148] K. Lu, J. W. Clark, F. H. Ghorbel, D. L. Ware, and A. Bidani, "A human cardiopulmonary system model applied to the analysis of the Valsalva maneuver," *American Journal of Physiology-Heart and Circulatory Physiology*, vol. 281, no. 6, pp. H2661–H2679, 2001.

[149] A. Guala, C. Camporeale, F. Tosello, C. Canuto, and L. Ridolfi, "Modelling and subject-specific validation of the heart-arterial tree system," *Annals of Biomedical Engineering*, vol. 43, no. 1, pp. 222–237, 2015.

[150] A. Deyranlou, J. H. Naish, C. A. Miller, A. Revell, and A. Keshmiri, "Numerical study of atrial fibrillation effects on flow distribution in aortic circulation," *Annals of Biomedical Engineering*, vol. 48, no. 4, pp. 1291–1308, 2020.

[151] A. Updegrove, N. M. Wilson, J. Merkow, H. Lan, A. L. Marsden, and S. C. Shadden, "SimVascular: an open source pipeline for cardiovascular simulation," *Annals of Biomedical Engineering*, vol. 45, no. 3, pp. 525–541, 2017.

[152] A. M. Climent, F. Atienza, J. Millet, and M. S. Guillem, "Generation of realistic atrial to atrial interval series during atrial fibrillation," *Medical & Biological Engineering & Computing*, vol. 49, pp. 1261–1268, 2011.

[153] E. Charitakis, U. Walfridsson, F. Nyström, E. Nylander, A. Strömberg, A. U, and W. H, "Symptom burden, metabolic profile, ultrasound findings, rhythm, neurohormonal activation, haemodynamics and health-related quality of life in patients with atrial Fibrillation (SMURF): a protocol for an observational study with a randomised interventional component," *BMJ Open*, vol. 5, no. 12, p. e008723, 2015.

[154] M. M. Ottaviani, L. Wright, T. Dawood, and V. G. Macefield, "In vivo recordings from the human vagus nerve using ultrasound-guided microneurography," *The Journal of Physiology*, vol. 598, no. 17, 2020.

[155] M. Patros, M. M. Ottaviani, L. Wright, T. Dawood, and V. G. Macefield, "Quantification of cardiac and respiratory modulation of axonal activity in the human vagus nerve," *The Journal of Physiology*, vol. 600, no. 13, 2022.

Part II

Included Papers

Paper I

An atrioventricular node model incorporating autonomic tone.
Felix Plappert, Mikael Wallman, Mostafa Abdollahpur, Pyotr G Platonov, Sten Östenson, Frida Sandberg
Published in: Frontiers in Physiology, vol. 13, 976468, 2022

frontiers | Frontiers in Physiology

TYPE Original Research
PUBLISHED 15 September 2022
DOI 10.3389/fphys.2022.976468

OPEN ACCESS

EDITED BY
Axel Loewe,
Karlsruhe Institute of Technology, Germany

REVIEWED BY
Jordi Heijman,
Maastricht University, Netherlands
Alberto Porta,
University of Milan, Italy

*CORRESPONDENCE
Felix Plappert,
felix.plappert@bme.lth.se

SPECIALTY SECTION
This article was submitted to Cardiac Electrophysiology, a section of the journal Frontiers in Physiology

RECEIVED 23 June 2022
ACCEPTED 10 August 2022
PUBLISHED 15 September 2022

CITATION
Plappert F, Wallman M, Abdollahpur M, Platonov PG, Östenson S and Sandberg F (2022), An atrioventricular node model incorporating autonomic tone.
Front. Physiol. 13:976468.
doi: 10.3389/fphys.2022.976468

An atrioventricular node model incorporating autonomic tone

Felix Plappert[1]*, Mikael Wallman[2], Mostafa Abdollahpur[1], Pyotr G. Platonov[3], Sten Östenson[4] and Frida Sandberg[1]

[1]Department of Biomedical Engineering, Lund University, Lund, Sweden, [2]Department of Systems and Data Analysis, Fraunhofer-Chalmers Centre, Gothenburg, Sweden, [3]Department of Cardiology, Clinical Sciences, Lund University, Lund, Sweden, [4]Department of Internal Medicine and Department of Clinical Physiology, Central Hospital Kristianstad, Kristianstad, Sweden

The response to atrial fibrillation (AF) treatment is differing widely among patients, and a better understanding of the factors that contribute to these differences is needed. One important factor may be differences in the autonomic nervous system (ANS) activity. The atrioventricular (AV) node plays an important role during AF in modulating heart rate. To study the effect of the ANS-induced activity on the AV nodal function in AF, mathematical modelling is a valuable tool. In this study, we present an extended AV node model that incorporates changes in autonomic tone. The extension was guided by a distribution-based sensitivity analysis and incorporates the ANS-induced changes in the refractoriness and conduction delay. Simulated RR series from the extended model driven by atrial impulse series obtained from clinical tilt test data were qualitatively evaluated against clinical RR series in terms of heart rate, RR series variability and RR series irregularity. The changes to the RR series characteristics during head-down tilt were replicated by a 10% decrease in conduction delay, while the changes during head-up tilt were replicated by a 5% decrease in the refractory period and a 10% decrease in the conduction delay. We demonstrate that the model extension is needed to replicate ANS-induced changes during tilt, indicating that the changes in RR series characteristics could not be explained by changes in atrial activity alone.

KEYWORDS

atrial fibrillation, atrioventricular node, autonomic tone, tilt test, mathematical modeling, ECG, RR series characteristics, sample entropy

1 Introduction

Atrial fibrillation (AF) is the most common supraventricular tachyarrhythmia (Hindricks et al., 2020). Characteristic for AF is an increased and irregular atrial activity that results in a rapid and irregular ventricular activation. Atrial fibrillation is linked to substantial morbidity and mortality, and is a significant burden to patients, physicians, and healthcare systems globally. Two main strategies of AF treatments are rate control and rhythm control. Rate control is one of the corner stones of AF management, however the effect of individual rate-control drugs are difficult to predict in advance. This is why the choice of a rate-control drug today remains empiric and driven largely by their

safety profile and contraindications rather than predicted efficacy. Therefore, the complex mechanisms of AF have to be better understood to personalize the treatment and reduce the burden of AF on the healthcare system.

It has been shown that the autonomic nervous system (ANS) is contributing to the initiation and maintenance of AF (Shen and Zipes, 2014). Either a predominance in sympathetic or in parasympathetic modulation has been observed to initiate an episode of paroxysmal atrial fibrillation (PAF); and in some patients, both the sympatho-vagal and vagal predominances have been observed to initiate PAF episodes (Lombardi et al., 2004). Hence, differences in the ANS activity among patients may be an important factor behind the inter-patient differences in response to treatment. To investigate the ANS-induced changes to the pathophysiology of AF, the effect of the ANS has to be quantified. One common method to quantify the autonomic tone during normal sinus rhythm (NSR) is by heart rate variability (HRV) (Sassi et al., 2015). In sinus rhythm, HRV can be used to obtain information about the function of the sinoatrial (SA) node. This information is valuable for the quantification of the autonomic tone, because the SA node is densely innervated by the ANS (Shen and Zipes, 2014; George et al., 2017). In AF, however, HRV cannot be used to quantify the autonomic tone, because the heart beats are not initiated in the SA node.

Instead, the ventricular rhythm during AF is determined by the atrial electrical activity and the subsequent AV nodal modulation. Since the AV node is densely innervated by the ANS, characterizing the AV nodal behavior during AF may give valuable information about the autonomic tone. Results from previous studies suggest that the heart rate, as well as the heart rate variability, quantified by RR rmssd, and heart rate irregularity, quantified by RR sample entropy, are affected by β-blocker induced changes in sympathetic response (Corino et al., 2015). We hypothesize that such changes in the heart rate and its variability and irregularity reflect ANS-induced changes in the AV node. The ANS-induced changes on the cardiac electrophysiology can be studied using head-up and head-down tilt test, which in a previous study was shown to affect electrophysiological properties of atrial myocardium during AF (Östenson et al., 2017). It is unclear if the changes in the heart rate and its variability and irregularity are explained by the changes in the atrial electrophysiology alone or also by changes in the AV nodal properties. Investigating how the ANS is modulating the heart rate during AF is a complex task and requires a model based analysis.

Previously, several AV node models have been proposed that incorporate important characteristics of the AV nodal structure and electrophysiology in their design. Characteristic for the AV node is its dual-pathway physiology enabling a parallel excitation propagation of impulses with different electrophysiological properties (George et al., 2017). For example, the slow pathway (SP) has a longer conduction delay and shorter refractory period compared to the fast pathway (FP) (George et al., 2017). Furthermore, the refractory period and conduction delay are dynamic and depend on the recent history of the conducted and blocked impulses in the AV nodal tissue (George et al., 2017; Billette and Tadros, 2019). Early models of the AV node did not account for the dual-pathway physiology (Cohen et al., 1983; Jørgensen et al., 2002; Rashidi and Khodarahmi, 2005; Mangin et al., 2005; Lian et al., 2006). Later models have incorporated this feature, represented by separate refractory periods (Corino et al., 2011; Henriksson et al., 2016; Inada et al., 2017; Wallman and Sandberg, 2018) and separate conduction delays (Climent et al., 2011b; Inada et al., 2017; Wallman and Sandberg, 2018). However, no models have explicitly incorporated ANS-induced changes in their model description.

Therefore, the aim of the present study is to incorporate ANS-induced changes into the AV node network model previously proposed by Wallman and Sandberg, (2018). The extension of the AV node model was guided by a distribution-based sensitivity analysis (Pianosi and Wagener 2018) and incorporates ANS-induced changes in the computation of the refractoriness and conduction delay. The extended model is evaluated with respect to its ability to replicate changes in heart rate and RR series variability and irregularity observed during head-up and head-down tilt test.

2 Materials and methods

First, the clinical tilt test data is described in Section 2.1. The RR series characteristics are defined in Section 2.2, followed by the description of a network model of the AV node (Section 2.3). A sensitivity analysis on the AV node model is described in Section 2.4, that identifies the influence of changes in model parameters on the RR series characteristics. Based on the sensitivity analysis, the AV node model is modified to account for ANS-induced changes in AV node characteristics (Section 2.5). The ability of the modified AV node model to replicate ANS induced changes in RR series characteristics observed during tilt-test is assessed in Section 2.6. Finally, the statistical analysis is described in Section 2.7, that is used to determine significant differences in AFR and RR series characteristics between tilt positions.

2.1 Tilt test study

The autonomic influence on the RR series characteristics was analysed using ECG data recorded during a tilt test study performed by Östenson et al. (2017). Recordings from 24 patients with persistent AF were considered of sufficient quality for analysis and were included in the present study; their age was 66 ± 9 (mean ± std), and 63% were men. None

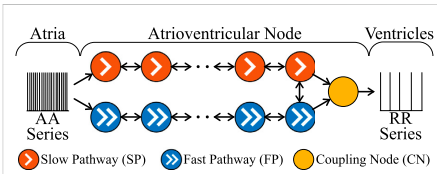

FIGURE 1
A schematic representation of the AV node model. Note that retrograde conduction is possible within the AV node model. For simplicity, only a subset of the ten nodes in each pathway is shown.

of the patients had abnormal levels of thyroid hormones, severe renal failure requiring dialysis, or heart valve disease. None of the patients were ablated for AF or on any of the Class I or Class III antiarrhythmic drugs. The tilt test was performed between 1 and 3 p.m. in a quiet study room. Standard 12-lead ECG was recorded during supine position, followed by head-down tilt (HDT, -30°) and then head-up tilt (HUT, +60°). The tilt table was manually operated and had hand grip and ankle support for HDT and foot board support for HUT; the patients remained in each position approximately 5 min. ECG preprocessing and R-peak detection was performed using the CardioLund ECG parser (www.cardiolund.com).

2.2 RR series characteristics

The RR series consists of the intervals between consecutive heartbeats, where the time of a heartbeat is determined by the corresponding R peak in the ECG signal. In this work, three statistical measures of the RR series characteristics were used, quantifying heart rate, heart rate variability and heart rate irregularity, respectively, defined according to Eqs. 1–3. The mean of the RR intervals ($\overline{RR}$) is computed as

$$\overline{RR} = \frac{1}{N}\sum_{i=1}^{N} RR_i, \tag{1}$$

where RR_i denotes the i:th RR interval in the RR series. The root mean square of successive RR interval differences (RR_V, variability) is computed as

$$RR_V = \sqrt{\frac{1}{N-1}\sum_{i=1}^{N-1}(RR_{i+1} - RR_i)^2}. \tag{2}$$

The sample entropy of the RR series (RR_I, irregularity) is computed as

$$RR_I = -\ln\left(\frac{\sum_{i=1}^{N-m}\sum_{j=1,j\neq i}^{N-m} b_{i,j}^{m+1}(r)}{\sum_{i=1}^{N-m}\sum_{j=1,j\neq i}^{N-m} b_{i,j}^{m}(r)}\right), \tag{3}$$

where the binary variable $b_{i,j}^{l}(r)$ with $l \in \{m, m+1\}$ has the value 1 if the maximum absolute distance between corresponding scalar elements in the vectors $V_i^l = \{RR_i, RR_{i+1}, \ldots, RR_{i+l-1}\}$ and V_j^l is below the tolerance r times the standard deviation of the RR interval series, otherwise the value is zero (Richman and Moorman, 2000). In this study, the parameters were set to $m = 2$ and $r = 0.2$.

2.3 Network model of the human atrioventricular node

The AV node is modelled by a network of 21 nodes (cf. Figure 1) (Wallman and Sandberg, 2018; Karlsson et al., 2021). The AV nodal dual-pathway physiology with a slow pathway (SP) and a fast pathway (FP) is represented with two chains of 10 nodes each. The last nodes of the two pathways are connected to each other and to an additional coupling node (CN). Impulses enter the AV node model simultaneously at the first node of each pathway and leave the model over the CN. Retrograde conduction is possible due to the bidirectional conduction within the pathways and between the last nodes of SP and FP.

Each node represents a section of the AV node and is described with an individual refractory period $R^P(\Delta t_k)$ and conduction delay $D^P(\Delta t_k)$ defined as

$$R^P(\Delta t_k) = R^P_{min} + \Delta R^P\left(1 - e^{-\Delta t_k/\tau_R^P}\right), \tag{4}$$

$$D^P(\Delta t_k) = D^P_{min} + \Delta D^P e^{-\Delta t_k/\tau_D^P}, \tag{5}$$

where P ∈ {SP, FP, CN} denotes the association to a pathway. The electrical excitation propagation through the AV node is modelled as a series of impulses that can either be passed on or blocked by a node. This decision is based on the interval Δt_k between the k:th impulse arrival time t_k and the end of the (k–1):th refractory period computed as

$$\Delta t_k = t_k - t_{k-1} - R^P(\Delta t_{k-1}). \tag{6}$$

If Δt_k is positive, the impulse is conducted to all adjacent nodes, otherwise the impulse is blocked due to the ongoing refractory period $R^P(\Delta t_{k-1})$. The conduction delay $D^P(\Delta t_k)$ describes the time delay between the arrival of an impulse at a node and its transmission to all adjacent nodes. If an impulse is conducted, $R^P(\Delta t_k)$ and $D^P(\Delta t_k)$ of the current node are updated according to Eqs. 4–6. For the computation of $R^P(\Delta t_k)$ and $D^P(\Delta t_k)$, the nodes in each pathway are characterized by six parameters, defining minimum refractory period, $R^P_{\min}$; maximum prolongation of refractory period, ΔR^P; time constant τ_R^P; minimum conduction delay, $D^P_{\min}$; maximum prolongation of conduction delay, ΔD^P; and the time constant τ_D^P. The SP, FP and CN are modelled with separate vectors $\boldsymbol{\theta}^P = [R^P_{\min}, \Delta R^P, \tau_R^P, D^P_{\min}, \Delta D^P, \tau_D^P]$, all with fixed values.

TABLE 1 Model parameters used for the sensitivity analysis.

Parameters	SP (ms)	FP (ms)	CN (ms)
$R_{\min}$	$\mathcal{U}[250, 600]$	$\mathcal{U}[250, 600]$	250
ΔR	$\mathcal{U}[0, 600]$	$\mathcal{U}[0, 600]$	0
τ_R	$\mathcal{U}[50, 300]$	$\mathcal{U}[50, 300]$	1
$D_{\min}$	$\mathcal{U}[0, 30]$	$\mathcal{U}[0, 30]$	0
ΔD	$\mathcal{U}[0, 75]$	$\mathcal{U}[0, 75]$	0
τ_D	$\mathcal{U}[50, 300]$	$\mathcal{U}[50, 300]$	1

The AV node model processes the impulse propagation chronologically and node by node, using a priority queue of nodes, sorted by impulse arrival time; details can be found in Wallman and Sandberg (2018). The input to the AV node model is a series of atrial impulses that is used to initialize the priority queue. As the impulses are conducted to adjacent nodes, new entries are added to the priority queue. The output of the AV node model is a series of impulses activating the ventricles.

In this study, the series of atrial impulses during AF is modelled as a point-process with independent inter-arrival times according to a Pearson Type IV distribution (Climent et al., 2011a). Hence, the atrial activation (AA) series is completely characterized by four parameters, namely the mean μ, standard deviation σ, skewness γ and kurtosis κ.

2.4 Distribution-based sensitivity analysis

The sensitivity of the three RR series characteristics $\boldsymbol{y} = [\overline{RR}, RR_V, RR_I]^\mathsf{T}$ to the AV node model and AA series parameters $\boldsymbol{x} = [\boldsymbol{\theta}^{SP}, \boldsymbol{\theta}^{FP}, \mu, \sigma]^\mathsf{T}$ is evaluated by applying a distribution-based sensitivity analysis, based on the work of Pianosi and Wagener, (2018). For the sensitivity analysis, cumulative distribution functions (CDF) are estimated using a dataset of $K = 250\,000$ randomly generated model parameter sets $\boldsymbol{x}$ and the characteristics $\boldsymbol{y}$ of the corresponding simulated RR series. For each simulation, an atrial impulse series with 60 000 AA intervals was generated using the Pearson Type IV distribution, with μ randomly drawn from $\mathcal{U}[100, 250]$ ms, σ randomly drawn from $\mathcal{U}[15, 30]$ ms, and γ and κ kept fixed to 1 and 6, respectively. The γ and κ were kept fixed since they cannot be estimated from the f-waves of the ECG. Negative AA intervals were excluded from the impulse series. The model parameters $\boldsymbol{\theta}^{SP}$ and $\boldsymbol{\theta}^{FP}$ were randomly drawn from bounded uniform distributions given in Table 1, as previously done in Karlsson et al. (2021). The $\boldsymbol{\theta}^{CN}$ were kept fixed according to Table 1, corresponding to $R^P(\Delta t_k)$ and $D^P(\Delta t_k)$ of the CN equal to 250 ms and 0 ms, respectively.

The RR series characteristics were computed using a series of 4000 RR intervals corresponding to the first impulses that left the AV node model through the CN. Two selection criteria were used to remove non-physiological parameter sets. First, a model parameter set was only included if the slow pathway had a lower refractory period $R^{SP}(\Delta t_k) < R^{FP}(\Delta t_k)$ and higher conduction delay $D^{SP}(\Delta t_k) > D^{FP}(\Delta t_k)$ than the fast pathway for all Δt_k. Second, the resulting $\overline{RR}$ was required to be in the range 300 ms $\leq \overline{RR} \leq$ 1000 ms, corresponding to heart rates between 60 bpm and 200 bpm. Heart rates below 60 bpm are disregarded, because the pacemaker function of the AV node, that becomes relevant in this case (George et al., 2017), is not incorporated in the AV node model. Heart rates above 200 bpm are disregarded based on a reported minimum refractory period in the bundle branches of around 300 ms (Denes et al., 1974).

A sensitivity coefficient $\mathcal{S}_{n,m}$ is computed for each pair of model parameter x_n and RR series characteristic y_m, where x_n is the n:th element in $\boldsymbol{x}$ and y_m is the m-th element in $\boldsymbol{y}$. The $\mathcal{S}_{n,m}$ indicates how much a change in model parameter x_n affects the distribution of y_m and is defined as

$$\mathcal{S}_{n,m} = \underset{c=1,\ldots,C}{\text{median}} \; \underset{d=1,\ldots,D}{\text{median}} \; \text{KS}\left(F^{(d)}_{y_m}(y_m), F_{y_m|x_n}(y_m|x_n \in \mathcal{I}_c)\right), \tag{7}$$

where $\text{KS}(F^{(d)}_{y_m}(y_m), F_{y_m|x_n}(y_m|x_n \in \mathcal{I}_c))$ is the Kolmogorov-Smirnov (KS) distance between the unconditional CDF $F^{(d)}_{y_m}(y_m)$ and the conditional CDF $F_{y_m|x_n}(y_m|x_n \in \mathcal{I}_c)$. When estimating $F_{y_m|x_n}(y_m|x_n \in \mathcal{I}_c)$, the range of variation of x_n is split into $C = 15$ equally spaced conditioning intervals $\mathcal{I}_c$, with $c = 1, \ldots, C$ (cf. Figure 2A). All samples within $\mathcal{I}_c$ are used to estimate the corresponding $F_{y_m|x_n}(y_m|x_n \in \mathcal{I}_c)$ (cf. Figure 2B). To generate the set of $F^{(d)}_{y_m}(y_m)$, with $d = 1, \ldots, D$, a subset of K/C samples are bootstrapped $D = 1000$ times (cf. Figures 2A,B). The KS distance is defined as

$$\text{KS}(F_1(y), F_2(y)) = \max_y |F_1(y) - F_2(y)|. \tag{8}$$

As the $F^{(d)}_{y_m}(y_m)$ and $F_{y_m|x_n}(y_m|x_n \in \mathcal{I}_c)$ are approximations based on a finite number of samples, parameters that have no influence on y_m can result in $\mathcal{S}_{n,m}$ above zero. The impact of approximation errors on $\mathcal{S}_{n,m}$ can be estimated for each y_m using a dummy parameter $\mathcal{D}_m$ defined as

$$\mathcal{D}_m = \underset{d=2,\ldots,D}{\text{median}} \; \text{KS}\left(F^{(d)}_{y_m}(y_m), F^{(1)}_{y_m}(y_m)\right), \tag{9}$$

A model parameter x_n is determined to have influence on y_m if and only if $\mathcal{S}_{n,m} > \mathcal{D}_m$.

2.5 Extended atrioventricular node model accounting for autonomic nervous system induced changes

The results from the sensitivity analysis (Section 3.1) indicate that changes in both the AV node model parameters and the AA

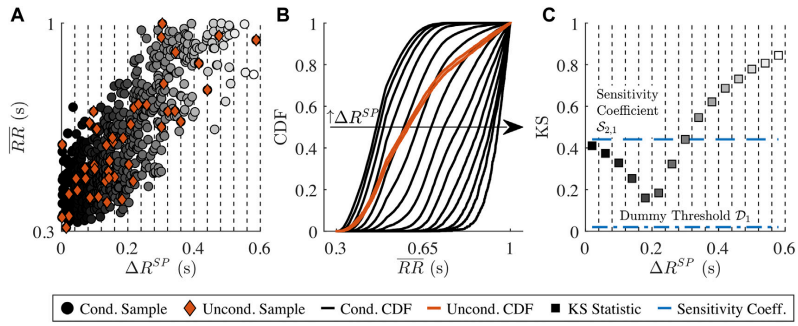

FIGURE 2
Illustration of the distribution-based sensitivity analysis. **(A)** $\overline{RR}$ plotted against one of the model parameters ΔR^{SP}. The samples that are used to estimate the conditional CDFs $F_{y_m|x_n}(y_m|x_n \in \mathcal{I}_c)$ are illustrated as circles and the conditioning intervals $\mathcal{I}_c$ are illustrated with vertical dotted lines. The samples that are used to estimate the unconditional CDF $F^{(d)}_{y_m}(y_m)$ are illustrated as diamonds. **(B)** $F_{y_m|x_n}(y_m|x_n \in \mathcal{I}_c)$ are illustrated as black lines, where the leftmost line corresponds to $F_{y_m|x_n}(y_m|x_n \in \mathcal{I}_1)$ with the lowest ΔR^{SP} values and the rightmost line corresponds to $F_{y_m|x_n}(y_m|x_n \in \mathcal{I}_{15})$. The 1,000 $F^{(d)}_{y_m}(y_m)$ lay all within the area illustrated by the red patch. **(C)** Each of the 15 squares correspond to $\underset{d=1,\ldots,D}{\text{median}}\ \text{KS}(F^{(d)}_{y_m}(y_m), F_{y_m|x_n}(y_m|x_n \in \mathcal{I}_c))$.

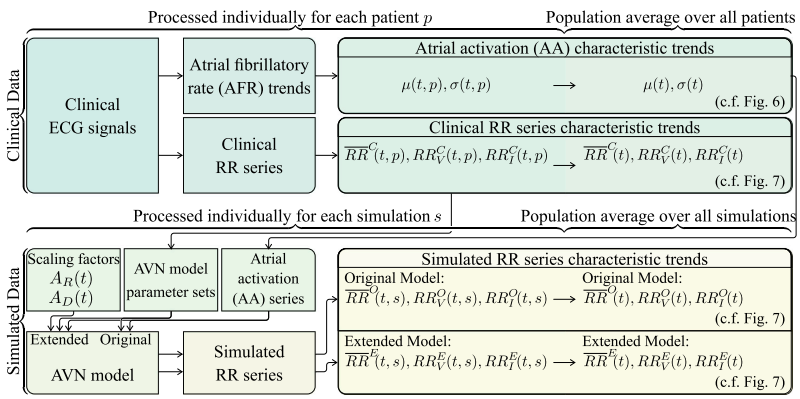

FIGURE 3
Schematic illustrating how the clinical and simulated RR series characteristic trends are computed.

series parameters have an influence on the RR series characteristics. Based on this, the AV node model described in Section 2.3 is extended to account for ANS-induced changes in the AA series by allowing $\mu(t)$ and $\sigma(t)$ of the Pearson Type IV distribution to vary over time. Moreover, the AV node model was extended by two scaling factors A_R and A_D, accounting for the effect of changes in autonomic tone on refractory period (A_R) and on conduction delay (A_D).

$$R^P(\Delta t_k, A_R) = A_R \cdot R^P(\Delta t_k) = A_R\left(R^P_{min} + \Delta R^P\left(1 - e^{-\Delta t_k / \tau^P_R}\right)\right) \tag{10}$$

$$D^P(\Delta t_k, A_D) = A_D \cdot D^P(\Delta t_k) = A_D\left(D^P_{min} + \Delta D^P e^{-\Delta t_k / \tau^P_D}\right) \tag{11}$$

The factors A_R and A_D model the combined effect of changes in sympathetic and parasympathetic activity and do not differ between the SP, FP and CN.

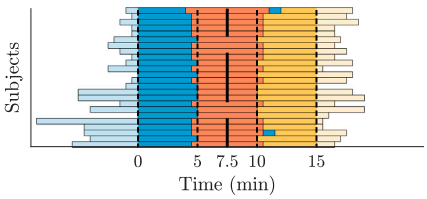

FIGURE 4
Tilt recordings of 24 patients divided into supine (blue), HDT (red) and HUT (yellow). The bars represent the length of the recorded ECG data. All recordings are centered along the middle of the HDT section.

2.6 Tilt-induced changes in extended atrioventricular node model

In this section, the extended AV node model proposed in Section 2.5 is investigated with respect to its ability to mimic tilt-induced changes in RR series characteristics.

The clinical ECG signals (cf. Section 2.1) are used to generate AA series for the AV node model input and to compare the characteristics of the simulated RR series to the clinical RR series (cf. Figure 3). For this purpose, a continuous 15-min ECG signal with 5 minutes per supine, HDT and HUT position was desired for each patient. In the clinical data, however, the length of the three tilt positions varied between patients with the supine position being between 5 and 13 min, HDT being between 5 and 7 min and HUT being between 5 and 9 min. For two patients, there was an additional minute in supine position between the HDT and HUT. The ECG signals were aligned to the middle of the HDT section and a 15-min long segment centered around the same midpoint was chosen for each patient (cf. Figure 4).

The clinical RR series characteristic trends $\overline{RR}^C(t,p)$, $RR_V^C(t,p)$ and $RR_I^C(t,p)$ for each patient p are computed from the RR intervals using a sliding window of length N according to Eqs. 1–3 (cf. Figure 3). For RR_V and RR_I, N is set to 200, because shorter RR interval series might lead to inaccuracies in the sample entropy computation (Yentes et al., 2013). For $\overline{RR}$, N is set to 100, as its computation is more robust than the computation of RR_V and RR_I and shorter RR interval series allow for a better temporal resolution. RR intervals in the clinical RR series preceding and following ectopic beats were excluded. For the computation of RR_I according to Eq. 3, vectors V_i^I with excluded RR intervals were omitted. The RR series characteristic trends of each patient $\overline{RR}^C(t,p)$, $RR_V^C(t,p)$ and $RR_I^C(t,p)$ were averaged over all 24 patients to obtain population-averaged clinical trends $\overline{RR}^C(t)$, $RR_V^C(t)$ and $RR_I^C(t)$ (cf. Figure 3).

TABLE 2 Ranges of the 240 model parameters used for the illustration (mean ± std).

Parameters	SP (ms)	FP (ms)	CN (ms)
$R_{\min}$	339 ± 77	493 ± 82	250 ± 0
ΔR	232 ± 112	369 ± 161	0 ± 0
τ_R	160 ± 77	162 ± 72	1 ± 0
$D_{\min}$	20 ± 7	7 ± 6	0 ± 0
ΔD	39 ± 20	23 ± 16	0 ± 0
τ_D	171 ± 71	163 ± 70	1 ± 0

For the generation of the AA series, first, an atrial fibrillatory rate (AFR) trend is estimated from each 15-min ECG segment (cf. Figure 3). The AFR is estimated by fitting a complex sinusoidal model to the f-waves of the ECG, following spatiotemporal QRST cancellation, as described in Henriksson et al. (2018). From each of the resulting AFR trends, the AA series parameters $\mu(t,p)$ and $\sigma(t,p)$ are estimated by the mean and standard deviation of 1/AFR using 1-min sliding windows; the resolution of the AFR trend is 0.02 s (cf. Figure 3). Then, $\mu(t,p)$ and $\sigma(t,p)$ are averaged over all 24 patients, resulting in the population-averaged trends $\mu(t)$ and $\sigma(t)$ (cf. Figure 3). Finally, the AA series is iteratively generated (cf. Figure 3). The first AA interval is drawn from the Pearson Type IV distribution with $\mu(0)$ and $\sigma(0)$, and each consecutive AA interval is drawn from the distribution with $\mu(t_i)$ and $\sigma(t_i)$ where t_i corresponds to the accumulated time of the previous AA intervals. The γ and κ of the Pearson Type IV distribution were kept fixed to 1 and 6, respectively.

For the simulations using the original and extended model, a set of 240 AV node model parameter vectors $\boldsymbol{x}' = [\boldsymbol{\theta}^{SP}, \boldsymbol{\theta}^{FP}, \boldsymbol{\theta}^{CN}]^{\mathsf{T}}$ were generated (cf. Figure 3). Ten parameter vectors per patient were selected from a set of randomly drawn parameter sets based on their ability to replicate the RR series characteristics of the 5-min long supine segment of the respective patient. A detailed description of the parameter sets and the selection process can be found in the Supplementary Section 1. The ranges of the model parameters in the 240 parameter sets are given in Table 2.

For the computation of simulated RR series characteristic trends using the original and the extended model, respectively, simulations were performed with each of the 240 parameter sets using 10 different realizations of the AA series generated from $\mu(t)$ and $\sigma(t)$. In the original model, the scaling factors A_R and A_D are not included, which is equivalent to the extended model using $A_R = 1$ and $A_D = 1$ (cf. Figure 3). In the extended model, A_R and A_D were allowed to change between supine and HDT and between HDT and HUT, respectively, but were assumed to remain constant within each position. Hence, for the extended model, A_R and A_D were set to 1 in the supine position, and different combinations of $A_R \in \{0.95, 1, 1.05\}$ and $A_D \in \{0.8, 1,$

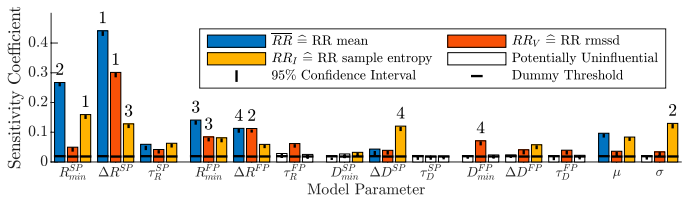

FIGURE 5
Distribution-based sensitivity indices describing the influence of changes in the 14 model parameters to changes in the three RR series characteristics. A model parameter is assumed to have influence on the RR series characteristics if the sensitivity coefficient is above the threshold of the dummy parameter (horizontal black line), otherwise it is not influential and illustrated with a white bar. The black vertical line illustrates the 95% confidence interval of the t bootstrapping iterations of the sensitivity coefficient. The ranking of the four most influential model parameters for each RR series characteristic is shown with the numbers above the bars.

1.2} were used for the simulations during HDT and HUT. For each simulation s, the mean RR interval trends $\overline{RR}^O(t,s)$ and $\overline{RR}^E(t,s)$ were computed from the RR interval series using a sliding window of length $N = 100$ (cf. Eq. 1). Whereas the RR variability and RR irregularity trends $RR_V^O(t,s)$ and $RR_I^O(t,s)$, as well as $RR_V^E(t,s)$ and $RR_I^E(t,s)$ were computed from the RR interval series using a sliding window of length $N = 200$ (cf. Eqs. 2 and 3). The simulated RR series characteristic trends were averaged over all parameter sets and realizations to obtain the population-averaged simulated trends $\overline{RR}^O(t)$, $RR_V^O(t)$ and $RR_I^O(t)$ for the original model and $\overline{RR}^E(t)$, $RR_V^E(t)$ and $RR_I^E(t)$ for the extended model (cf. Figure 3).

2.7 Statistical analysis

A Wilcoxon signed rank test was applied to determine if AFR, $\overline{RR}$, RR_V and RR_I differed significantly between supine, HDT and HUT. For the analysis, the AFR and RR series characteristics were computed for each patient and tilt position using the 5-min long ECG segments (cf. Figure 4). A p-value < 0.05 was considered significant.

3 Results

3.1 Sensitivity analysis

Results from the distribution-based sensitivity analysis (described in Section 2.4) with respect to the influence of the AV node model parameters on RR series characteristics are shown in Figure 5. Heart rate, quantified by $\overline{RR}$ is predominantly sensitive to changes in the refractory period parameters with the four largest contributors being the $R_{\min}$ and ΔR parameters of both pathways. In contrast, the changes in the conduction delay had little influence on the $\overline{RR}$, with ΔD^{SP} being the only conduction delay parameter that is slightly above the dummy threshold. Changes in the mean of the AA series μ were also influential on the $\overline{RR}$, while changes in the standard deviation σ of the AA series are not considered to have influence to changes in $\overline{RR}$.

For RR_V quantifying RR series variability, nearly all model parameters of the refractory period, conduction delay and AA series had sensitivity coefficients above the dummy threshold. The four largest contributors to changes in the RR_V were the ΔR parameters of both pathways, as well as the minimum refractory period and minimum conduction delay of the fast pathway, $R_{\min}^{FP}$ and $D_{\min}^{FP}$.

The RR_I quantifying RR series irregularity was also influenced by most model parameters of the refractory period, conduction delay and AA series. The four largest contributors were the minimum refractory period of the slow pathway $R_{\min}^{SP}$, the standard deviation σ of the AA series and the maximum prolongation of the refractory period and conduction delay of the slow pathway, ΔR^{SP} and ΔD^{SP}.

TABLE 3 Mean ± std of AFR and RR series characteristics of the 24 patients in the study population for each tilt position.

Tilt Position	Supine	HDT	HUT
AFR mean (Hz)	6.78 ± 0.64	6.62 ± 0.7**	6.84 ± 0.63*,†
$\overline{RR}$ (ms)	656 ± 126	642 ± 111*	613 ± 115**,†
RR_V (ms)	192 ± 54	182 ± 45	176 ± 51**
RR_I	2.09 ± 0.2	2.05 ± 0.28	1.95 ± 0.31**

HDT, head-down tilt; HUT, head-up tilt. *$p < 0.05$ vs Supine. **$p < 0.01$ vs Supine. †$p < 0.05$ vs HDT.

3.2 Clinical data

The AFR decreased significantly from the supine position to HDT and increased significantly from HDT to HUT, where the

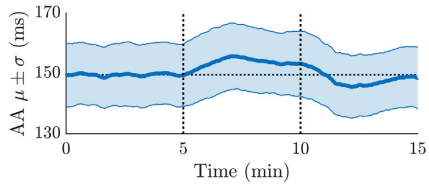

FIGURE 6
Averaged mean and standard deviation of the AA series estimated from ECG recordings of 24 patients. The first 5 min were during supine position, followed by 5 min of HDT and 5 min of HUT. The horizontal dotted line illustrates the average of the μ trend during the first 5 min.

AFR during HUT was significantly higher than during supine (Table 3). The heart rate increased during HDT and increased further during HUT (Table 3). The results align with the observations of Östenson et al. (2017). The variability and irregularity of the RR series decreased during HDT and decreased further during HUT (Table 3). For the variability and irregularity of the RR series, only the differences between supine and HUT were statistically significant.

3.3 Tilt-induced changes in atrioventricular node model

The average of $\mu(t)$ and $\sigma(t)$ over all 24 patients is illustrated in Figure 6. The $\mu(t)$ shows a clear variation during HDT and HUT, but not in supine position, where $\mu(t)$ was approximately constant around 150 ms. Compared to $\mu(t)$ during supine position, $\mu(t)$ increased during HDT and decreased during HUT (cf. Figure 6).

In Figure 7, the characteristics $\overline{RR}^C(t)$, $RR_V^C(t)$ and $RR_I^C(t)$ estimated from clinical data during tilt test are illustrated. It can be seen that $\overline{RR}^C(t)$, $RR_V^C(t)$ and $RR_I^C(t)$ are decreasing from supine to HDT and decreasing further from HDT to HUT. When performing the simulations with the original model, $\overline{RR}^O(t)$, $RR_V^O(t)$ and $RR_I^O(t)$ are decreasing from supine to HDT, but increasing from HDT to HUT. When performing the simulations with the extended model, $\overline{RR}^E(t)$, $RR_V^E(t)$ and $RR_I^E(t)$ are decreasing from supine to HDT and decreasing further from HDT to HUT. Comparing the clinical and simulated trends of $\overline{RR}(t)$ and $RR_V(t)$, it can be seen that the extended model accounting for ANS-induced changes can better replicate the observed changes to the clinical RR series characteristics compared to the original model. For $RR_I(t)$, both the original and extended model produce RR series that are more regular than the clinical RR series, as the irregularity quantified by the sample entropy is higher for the clinical RR series. For the simulated RR series characteristics of the extended model, the average of $\overline{RR}^E(t)$, $RR_V^E(t)$ and $RR_I^E(t)$ during the 5 min in HDT and HUT were illustrated for the nine different combinations of $A_R \in \{0.95, 1, 1.05\}$ and $A_D \in \{0.9, 1, 1.1\}$. For $\overline{RR}^E(t)$, $RR_V^E(t)$ and $RR_I^E(t)$, an increase in A_R causes an increase, and for $\overline{RR}^E(t)$ and $RR_V^E(t)$, an increase in A_D causes an increase. However, for $RR_I^E(t)$, an increase in A_D instead causes a decrease. The $\overline{RR}^E(t)$, $RR_V^E(t)$ and $RR_I^E(t)$ are obtained using $A_R = 1$ and $A_D = 0.9$ during HDT and $A_R = 0.95$ and $A_D = 0.9$ during HUT and are displayed in Figure 7; the scaling factors were chosen so that the resulting $\overline{RR}^E(t)$ and $RR_V^E(t)$ matches $\overline{RR}^C(t)$ and $RR_V^C(t)$.

4 Discussion

The aim of this study was to extend the AV node model (Wallman and Sandberg, 2018) to incorporate ANS-induced changes. The extension of the AV node model was guided by a distribution-based sensitivity analysis. The sensitivity analysis indicated that the refractory period and conduction delay parameters as well as the atrial impulse series had a significant influence on the heart rate as well as the variability and the irregularity of the RR series, while the most influential parameters were predominantly those describing the refractory period. Rather than modelling the effect of the sympathetic and parasympathetic activity separately, we describe the joint effects, i.e., the autonomic tone. We proposed an extension to the AV node model that accounts for the ANS-induced changes by introducing scaling factors for the refractory period and conduction delay. The capability of the extended AV node model to replicate ANS-induced changes was investigated by comparison to ECG data acquired during tilt test.

Our results (Figure 7) indicate that the extended model, but not the original, could replicate the observed changes in the clinical RR series characteristics during HUT and HDT, since the changes in RR series characteristics could not be explained by changes in atrial activity alone. The $\overline{RR}^E(t)$, $RR_V^E(t)$ and $RR_I^E(t)$ (Figure 7) show that a decrease in refractory period and conduction delay allow the model to replicate the decrease in $\overline{RR}^C(t)$, $RR_V^C(t)$ and $RR_I^C(t)$. Conversely, if the refractory period and conduction delay are kept fixed for $\overline{RR}^O(t)$, $RR_V^O(t)$ and $RR_I^O(t)$, all three RR series characteristics increase during HUT, which is the opposite direction of change of $\overline{RR}^C(t)$, $RR_V^C(t)$ and $RR_I^C(t)$. When comparing $RR_I^O(t)$ and $RR_I^E(t)$ with $RR_I^C(t)$, it can be seen that the sample entropy of the simulated RR series is lower than that of the clinical RR series. This highlights that the simulated RR series are more regular than the clinical RR series. One possible explanation for a lower irregularity in simulated RR series is the lack of short-term variations in AV node refractoriness and conduction delay. Such short-term variations may be induced by respiratory modulation in ANS activity. Thus, a natural next step in our model development will be to incorporate the respiratory modulation of the ANS, likely via periodical variations in the scaling factors A_R and A_D.

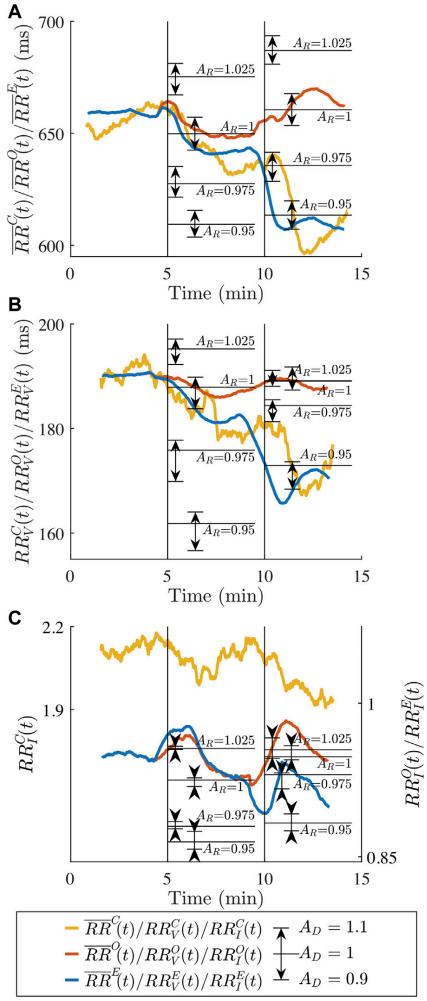

FIGURE 7
Average clinical RR series characteristics **(A)** $\overline{RR}^C(t)$ **(B)** $RR^C_V(t)$ and **(C)** $RR^C_I(t)$ (yellow) and average simulated RR series characteristics for the original model **(A)** $\overline{RR}^O(t)$ **(B)** $RR^O_V(t)$ and **(C)** $RR^O_I(t)$ (red) and average simulated RR series characteristics for the extended model **(A)** $\overline{RR}^E(t)$ **(B)** $RR^E_V(t)$ and **(C)** $RR^E_I(t)$ (blue). The dashed black lines mark the transition between the supine and HDT, and HDT and HUT, respectively. Horizontal black lines show 5-min averages of $\overline{RR}^C(t)$, $RR^E_V(t)$ and $RR^E_I(t)$ during HDT or HUT with A_R as indicated and A_D = 1. Arrows show the impact of perturbing A_D by +0.1 (arrow pointing up) or −0.1 (arrow pointing down).

Many electrophysiological (EP) studies have demonstrated that an increase in sympathetic activity is causing a decrease in the human AV nodal conduction delay (Lister et al., 1965; Dhingra et al., 1973; Morady et al., 1988; Cossú et al., 1997) and a decrease in the refractory period (Morady et al., 1988; Cossú et al., 1997). Moreover, a decrease in sympathetic activity in the human AV node is causing an increase in conduction delay and refractory period (Morady et al., 1988). Head-up tilt is associated with increased sympathetic tone, and it has been demonstrated that the AV nodal conduction delay and refractory period decrease when changing the posture from supine to standing (Hashimoto et al., 1991). The results in Figure 7 confirm that a reduction in the conduction delay using A_D = 0.9 and a reduction in the refractory period using A_R = 0.95 better replicate the observed changes in the clinical RR series characteristics than the original model during HUT. Decreases in refractory period and conduction delay of up to 30% in response to isoproterenol-induced increases in sympathetic activity have been reported (Lister et al., 1965; Dhingra et al., 1973; Cossú et al., 1997). However, when considering that the reported changes in heart rate due to the isoproterenol administration is larger than the observed changes in $\overline{RR}$ during tilt, the parameter choice of A_D = 0.9 and A_R = 0.95 are reasonable for the tilt test data used in this study.

Increased parasympathetic activity has been associated with an increased conduction delay (Martin, 1977); studies in dogs reported an increased conduction delay with acetylcholine administration (Priola et al., 1983; Bertrix et al., 1984) and vagal stimulation (Spear and Moore, 1973; Martin, 1975; Pirola and Potter, 1990). Moreover, there are indications that an increased parasympathetic activity is associated with an increased refractory period (Martin, 1977); experimental studies using rabbit hearts reported an increased AV-nodal refractory period (West and Toda, 1967) and occurrences of 2:1 AV nodal block (Cranefield et al., 1959) with acetylcholine administration, and studies in dogs reported occurrences of AV block with acetylcholine administration (Hageman et al., 1985) and vagal stimulation (Spear and Moore, 1973; Hageman et al., 1985).

It is unclear how the HDT affects the sympathetic and parasympathetic activity. The results in Figure 7 show that a reduction in the conduction delay using A_D = 0.9 and no modification of the refractory period using A_R = 1 better replicate the observed changes in the clinical RR series characteristics than the original model during HDT. These results are consistent with possible slight increase in sympathetic tone provoked by HDT. However, other interpretations are possible. Nagaya et al. (1995) postulated a diminished sympathetic activity in HDT. Under that hypothesis, the results in Figure 7 suggest a decrease in parasympathetic tone to revert the direction of change caused by a decreased sympathetic tone. It should be noted that the model presented here does not distinguish between these two possibilities, since

A_D and A_R are modelling the joint effect of changes in parasympathetic and sympathetic activity. Hence, the scale factor A_D = 0.9 during HDT could be reflecting either a slight increase in sympathetic activity, a slight decrease in parasympathetic activity, a larger increase in sympathetic activity combined with an increase in parasympathetic activity, or a large decrease in parasympathetic activity combined with a decrease in sympathetic activity.

The set of scaling factors A_R and A_D used to create $\overline{RR}^E(t)$, $RR_V^E(t)$ and $RR_I^E(t)$ in Figure 7 results in RR series characteristics similar to that observed during HDT and HUT. The results in Figure 7 show that a scaling factor A_R below 1, i.e., a decrease of the refractory period, causes a decrease in $\overline{RR}^E(t)$, $RR_V^E(t)$ and $RR_I^E(t)$. Conversely, a scaling factor A_R above 1, i.e., an increase of the refractory period, causes an increase in $\overline{RR}^E(t)$, $RR_V^E(t)$ and $RR_I^E(t)$. A scaling factor A_D below 1, i.e., a decrease in conduction delay, causes a decrease in $\overline{RR}^E(t)$, $RR_V^E(t)$ and vice versa. The opposite relationship can be seen for the RR series irregularity, where a scaling factor A_D below 1 causes an increase in $RR_I^E(t)$ and vice versa. Moreover, when considering one RR series characteristic at a time, it can be anticipated in Figure 7 that the same 5-min average value of the RR series characteristics can be achieved with different combinations of A_R and A_D. Hence, considering all three RR series characteristics simultaneously increases the likelihood of identifying a unique pair of scaling factors A_R and A_D that fits the observed data.

To reduce the complexity of the model, the refractoriness and conduction delay of the SP, FP and CN are modified with the same A_R and A_D. However, due to the structural and molecular heterogeneity of the different pathways, it is likely that the ANS-induced changes affect each pathway differently (George et al., 2017). In rabbit hearts, it was reported that acetylcholine strongly affects fibers of the atrionodal junction but does not show any effect in the lower part of the node or the bundle of His (Trautwein, 1963). In the description of the AV node model, the CN is merging the impulses from the SP and FP and its refractory period and conduction delay is independent of Δt_k. In contrast to Karlsson et al. (2021), $R_{\min}^{CN}$ was set to the minimum of the bounded uniform distributions for the $R_{\min}^{SP}$ and the $R_{\min}^{FP}$ given in Table 1. Further, the conduction delay of the CN was set to 0, as other choices of a constant conduction delay would not have changed the resulting RR series. In previous work on the network model (Wallman and Sandberg, 2018; Karlsson et al., 2021), the AA interval series was modelled as a Poisson process. However, based on results of Climent et al. (2011a), a Pearson Type IV distribution better reproduces the statistical properties of the AA interval series during AF and was therefore chosen in the present study. The mean and standard deviation of the Pearson Type IV distribution were determined from the mean and standard deviation of the AFR. However, the skewness and kurtosis were fixed, as their sensitivity coefficients were uninfluential (data not shown) and since there is no straight-forward way to estimate these parameters from the f-waves of the ECG.

In the present study, the ability of the extended model to mimic tilt-induced changes was investigated using data from a previous study (Östenson et al., 2017), with tilt angles fixed to -30° in HDT and 60° in HUT, respectively. Different tilt angles of the tilt, i.e., different magnitude of the orthostatic stimulus, may affect the ANS response and hence the resulting RR series characteristics. Previous results from patients in normal sinus rhythm show that the sample entropy of the RR series was decreasing during HUT from 0° to 60° but remained roughly constant from 60° to 90° (Porta et al., 2007). Based on these results, we assume that the tilt angle of 60° is sufficiently large to induce changes in autonomic tone. Access to data from patients with AF during other tilt-inclinations could potentially be used to refine the model to take the degree on inclination into account. The tilt-induced changes in RR series irregularity observed in the present study are in line with the results in Patel et al. (2018), where a decrease in RR sample entropy in response to HUT in patients with AF was reported. The tilt-induced changes in RR series irregularity observed in the present study are also in line with the changes reported for patients in normal sinus rhythm during HUT (Porta et al., 2007). Results from previous studies suggest that the RR series irregularity during normal sinus rhythm increase in response to HDT (Porta et al., 2015), whereas a slight but not significant decrease was observed in the present study with patients in AF. However, it should be noted that origin of RR series variability and irregularity during AF differs from that during normal sinus rhythm and hence, the interpretation of the results with respect to autonomic tone may be different.

The effect of the ANS-induced activity was investigated with respect to its ability to mimic the population-averaged changes observed during tilt test. The RMSSD and sample entropy were used to quantify RR series variability and irregularity, respectively, since these statistical measures have been used in previous studies to assess changes in RR series characteristics during AF in response to drugs (Corino et al., 2015) and tilt-test (Patel et al., 2018). Population-averaged trends were chosen over the trends of individual patients to reduce the uncertainty in the estimation of the clinical RR_V and RR_I trends. The parameter sets used for the simulations in Section 2.6 were selected to be representative of the patients in the present study based on their ability to replicate RR series characteristics observed during supine position. However, it should be noted that fitting of the model to individual patients is outside the scope of the present study. Due to the short measurement duration of the clinical data, a robust estimation of individual model parameters is not to be expected with the present methodology (Karlsson et al., 2021). Longer measurements from more patients will allow model development and evaluation on a patient-specific basis, forming an attractive next step.

A distribution-based sensitivity analysis was chosen over a variance-based method, because the distributions of the

simulated RR series characteristics are highly-skewed and multimodal. Hence, variance alone cannot adequately represent the uncertainty (Pianosi and Wagener, 2018). Instead, a distribution-based method characterizes the uncertainty and sensitivity by investigating the entire distribution of the model outputs (Pianosi and Wagener, 2018). The results of the sensitivity analysis in Figure 5 indicate that τ_D^{SP} is the only model parameter that is uninfluential, since the sensitivity coefficients for all three RR series characteristics are below the dummy threshold. One important outcome of the sensitivity analysis therefore is that the refractory period and conduction delay of the AV node as well as the atrial input are influencing the RR series characteristics. For simplicity, we are proposing a linear scaling of refractory period and conduction delay parameters, but it would be interesting to refine this model description in the light of additional clinical data. It should be noted that the sensitivity coefficients $\mathcal{S}_{n,m}$ are quantifying sensitivity on a global scale, and that there may be large local variations. As a result, the extent of variation in $\overline{RR}(t)$, $RR_V(t)$ and $RR_I(t)$ for a set of scaling factors A_R and A_D depend on the model parameters. For example, in Figure 7, it is clear that the scaling factor A_D affects $\overline{RR}(t)$, while the sensitivity analysis (Figure 5) indicates that the influence of changes in conduction delay on $\overline{RR}(t)$ is very limited on a global scale.

In the present study, the estimates in $RR_V^E(t)$ and $RR_I^E(t)$ were based on sliding windows of $N = 200$ RR intervals. The choice of N is a tradeoff between estimation accuracy and time resolution. The sample entropy estimation is expected to stabilize with greater N and a minimum of $N \geq 200$ was recommended by Yentes et al. (2013). In the present study, N was chosen as short as possible in favour of time resolution to investigate the ANS-induced changes in the RR series characteristics during tilt. To accommodate the estimation uncertainty resulting from a small N, the simulated RR series characteristics trends were averaged over 10 repeated simulations for 240 different parameter sets. For the sensitivity analysis, N was chosen to be 4,000 in favour of estimation accuracy since the simulation was stationary.

While ANS modulation has been extensively studied during normal sinus rhythm (Porta et al., 2007; Porta et al., 2015; Sassi et al., 2015; Patel et al., 2018), no attempts have been made towards the estimation of ANS modulation during persistent AF. The present study is a first step towards developing a model of the AV node that will ultimately be used to quantify ANS modulation on a patient specific basis by fitting to RR interval series and information on atrial electrical activity obtained from clinical ECG recordings. The results (Figure 7) show that the proposed extended model of the AV node accounting for changes in autonomic tone can better replicate changes in RR series characteristics observed during tilt-test than the original model, implying that this is a viable approach to take. Further developments are needed to incorporate ANS modulation in the model and methodology for robust estimation of such modulation from clinical data.

5 Conclusion

We present an extended AV node model that incorporates ANS-induced changes. The extension was guided by a distribution-based sensitivity analysis showing that changes in refractoriness and conduction delay of the AV node as well as changes in atrial activity significantly influence the RR series characteristics. We demonstrate that the model extension is needed to replicate the changes in heart rate and RR series variability and irregularity observed during head-up and head-down tilt.

Data availability statement

The data analyzed in this study is subject to the following licenses/restrictions: The data is owned by the Department of Cardiology, Clinical Sciences, Lund University, Sweden. Requests to access these datasets should be directed to pyotr.platonov@med.lu.se. The code for the extended model together with a user example can be found in the Supplementary Material.

Ethics statement

The studies involving human participants were reviewed and approved by Regionala Etikprövningsnämnden i Lund. The patients/participants provided their written informed consent to participate in this study.

Author contributions

FP, MW, PP, and FS contributed to conception and design of the study. SÖ was responsible for the tilt test experiment. MA and FS were responsible for ECG processing. FP performed the distribution-based sensitivity analysis, designed and evaluated the extended AV node model, wrote the original draft of the manuscript and produced the figures, with supervision from MW and FS. MW, PP and FS contributed to the funding acquisition. PP and SÖ contributed to the clinical interpretation of the results. All authors contributed to manuscript revision, read, and approved the submitted version.

Funding

The research was supported by the Swedish Research Council (grant VR 2019–04272) and the Crafoord Foundation (grant 20200605).

Conflict of interest

The authors declare that the research was conducted in the absence of any commercial or financial relationships that could be construed as a potential conflict of interest.

Publisher's note

All claims expressed in this article are solely those of the authors and do not necessarily represent those of their affiliated organizations, or those of the publisher, the editors and the reviewers. Any product that may be evaluated in this article, or claim that may be made by its manufacturer, is not guaranteed or endorsed by the publisher.

Supplementary material

The Supplementary Material for this article can be found online at: https://www.frontiersin.org/articles/10.3389/fphys.2022.976468/full#supplementary-material

References

Bertrix, L., Bouzouita, K., Lang, J., Lakhal, M., Chah, Q. T., and Faucon, G. (1984). Potentiation by hypokalemia of the effects of acetylcholine on the canine heart *in situ*. *Naunyn. Schmiedeb. Arch. Pharmacol.* 326, 169–174. doi:10.1007/BF00517315

Billette, J., and Tadros, R. (2019). An integrated overview of av node physiology. *Pacing Clin. Electrophysiol.* 42, 805–820. doi:10.1111/pace.13734

Climent, A. M., Atienza, F., Millet, J., and Guillem, M. S. (2011a). Generation of realistic atrial to atrial interval series during atrial fibrillation. *Med. Biol. Eng. Comput.* 49, 1261–1268. doi:10.1007/s11517-011-0823-2

Climent, A. M., Guillem, M. S., Zhang, Y., Millet, J., and Mazgalev, T. N. (2011b). Functional mathematical model of dual pathway av nodal conduction. *Am. J. Physiol. Heart Circ. Physiol.* 300, 1393–1401. doi:10.1152/ajpheart.01175.2010

Cohen, R. J., Berger, R. D., and Dushane, T. E. (1983). A quantitative model for the ventricular response during atrial fibrillation. *IEEE Trans. Biomed. Eng.* 30, 769–781. doi:10.1109/TBME.1983.325077

Corino, V. D., Sandberg, F., Mainardi, L. T., and Sörnmo, L. (2011). An atrioventricular node model for analysis of the ventricular response during atrial fibrillation. *IEEE Trans. Biomed. Eng.* 58, 3386–3395. doi:10.1109/TBME.2011.2166262

Corino, V. D., Ulimoen, S. R., Enger, S., Mainardi, L. T., Tveit, A., and Platonov, P. G. (2015). Rate-control drugs affect variability and irregularity measures of RR intervals in patients with permanent atrial fibrillation. *J. Cardiovasc. Electrophysiol.* 26, 137–141. doi:10.1111/jce.12580

Cossú, S. F., Rothman, S. A., Chmielewski, I. L., Hsia, H. H., Vogel, R. L., Miller, J. M., et al. (1997). The effects of isoproterenol on the cardiac conduction system: Site-specific dose dependence. *J. Cardiovasc. Electrophysiol.* 8, 847–853. doi:10.1111/j.1540-8167.1997.tb00845.x

Cranefield, P. F., Hoffman, B. F., and Paes de Carvalho, A. (1959). Effects of acetylcholine on single fibers of the atrioventricular node. *Circ. Res.* 7, 19–23. doi:10.1161/01.RES.7.1.19

Denes, P., Wu, D., Dhingra, R., Pietras, R. J., and Rosen, K. M. (1974). The effects of cycle length on cardiac refractory periods in man. *Circulation* 49, 32–41. doi:10.1161/01.CIR.49.1.32

Dhingra, R. C., Winslow, E., Pouget, J. M., Rahimtoola, S. H., and Rosen, K. M. (1973). The effect of isoproterenol on atrioventricular and intraventricular conduction. *Am. J. Cardiol.* 32, 629–636. doi:10.1016/S0002-9149(73)80055-4

George, S. A., Faye, N. R., Murillo-Berlioz, A., Lee, K. B., Trachiotis, G. D., and Efimov, I. R. (2017). At the atrioventricular crossroads: Dual pathway electrophysiology in the atrioventricular node and its underlying heterogeneities. *Arrhythm. Electrophysiol. Rev.* 6, 179–185. doi:10.15420/aer.2017.30.1

Hageman, G. R., Neely, B. H., Urthaler, F., and James, T. N. (1985). Negative chronotropic and parasympatholytic effects of alinidine on canine sinus node and AV junction. *Am. J. Physiol.* 248, 324–330. doi:10.1152/ajpheart.1985.248.3.H324

Hashimoto, T., Fukatani, M., Mori, M., and Hashiba, K. (1991). Effects of standing on the induction of paroxysmal supraventricular tachycardia. *J. Am. Coll. Cardiol.* 17, 690–695. doi:10.1016/S0735-1097(10)80185-8

Henriksson, M., Corino, V. D., Sörnmo, L., and Sandberg, F. (2016). A statistical atrioventricular node model accounting for pathway switching during atrial fibrillation. *IEEE Trans. Biomed. Eng.* 63, 1842–1849. doi:10.1109/TBME.2015.2503562

Henriksson, M., Marozas, V., Sandberg, F., and Sörnmo, L. (2018). PetrnasModel-based assessment of f-wave signal quality in patients with atrial fibrillation. *IEEE Trans. Biomed. Eng.* 65, 2600–2611. doi:10.1109/TBME.2018.2810508

Hindricks, G., Potpara, T., Dagres, N., Arbelo, E., Bax, J. J., Blomström-Lundqvist, C., et al. (2020). 2020 ESC Guidelines for the diagnosis and management of atrial fibrillation developed in collaboration with the European Association for Cardio-Thoracic Surgery (EACTS): The Task Force for the diagnosis and management of atrial fibrillation of the European Society of Cardiology (ESC) Developed with the special contribution of the European Heart Rhythm Association (EHRA) of the ESC. *Eur. Heart J.* 42, 373–498. doi:10.1093/eurheartj/ehaa612

Inada, S., Shibata, N., Iwata, M., Haraguchi, R., Ashihara, T., Ikeda, T., et al. (2017). Simulation of ventricular rate control during atrial fibrillation using ionic channel blockers. *J. Arrhythm.* 33, 302–309. doi:10.1016/j.joa.2016.12.002

Jørgensen, P., Schäfer, C., Guerra, P. G., Talajic, M., Nattel, S., and Glass, L. (2002). A mathematical model of human atrioventricular nodal function incorporating concealed conduction. *Bull. Math. Biol.* 64, 1083–1099. doi:10.1006/bulm.2002.0313

Karlsson, M., Sandberg, F., Ulimoen, S. R., and Wallman, M. (2021). Non-invasive characterization of human AV-nodal conduction delay and refractory period during atrial fibrillation. *Front. Physiol.* 12, 728955. doi:10.3389/fphys.2021.728955

Lian, J., Müssig, D., and Lang, V. (2006). Computer modeling of ventricular rhythm during atrial fibrillation and ventricular pacing. *IEEE Trans. Biomed. Eng.* 53, 1512–1520. doi:10.1109/TBME.2006.876627

Lister, J. W., Stein, E., Kosowsky, B. D., Lau, S. H., and Damato, A. N. (1965). Atrioventricular conduction in man: Effect of rate, exercise, isoproterenol and atropine on the p-r interval. *Am. J. Cardiol.* 16, 516–523. doi:10.1016/0002-9149(65)90028-7

Lombardi, F., Tarricone, D., Tundo, F., Colombo, F., Belletti, S., and Fiorentini, C. (2004). Autonomic nervous system and paroxysmal atrial fibrillation: A study based on the analysis of RR interval changes before, during and after paroxysmal atrial fibrillation. *Eur. Heart J.* 25, 1242–1248. doi:10.1016/j.ehj.2004.05.016

Mangin, L., Vinet, A., Pagé, P., and Glass, L. (2005). Effects of antiarrhythmic drug therapy on atrioventricular nodal function during atrial fibrillation in humans. *Europace* 7, S71–S82. doi:10.1016/j.eupc.2005.03.016

Martin, P. (1975). Dynamic vagal control of atrial-ventricular condition: Theoretical and experimental studies. *Ann. Biomed. Eng.* 3, 275–295. doi:10.1007/BF02390973

Martin, P. (1977). The influence of the parasympathetic nervous system on atrioventricular conduction. *Circ. Res.* 41, 593–599. doi:10.1161/01.RES.41.5.593

Morady, F., Nelson, S. D., Kou, W. H., Pratley, R., Schmaltz, S., De Buitleir, M., et al. (1988). Electrophysiologic effects of epinephrine in humans. *J. Am. Coll. Cardiol.* 11, 1235–1244. doi:10.1016/0735-1097(88)90287-2

Nagaya, K., Wada, F., Nakamitsu, S., Sagawa, S., and Shiraki, K. (1995). Responses of the circulatory system and muscle sympathetic nerve activity to head-down tilt in humans. *Am. J. Physiol.* 268, R1289–R1294. doi:10.1152/ajpregu.1995.268.5.R1289

Östenson, S., Corino, V. D., Carlsson, J., and Platonov, P. G. (2017). Autonomic influence on atrial fibrillatory process: Head-up and head-down tilting. *Ann. Noninvasive Electrocardiol.* 22, e12405. doi:10.1111/anec.12405

Patel, H. C., Hayward, C., Wardle, A. J., Middleton, L., Lyon, A. R., Di Mario, C., et al. (2018). The effect of head-up tilt upon markers of heart rate variability in patients with atrial fibrillation. *Ann. Noninvasive Electrocardiol.* 23, e12511. doi:10.1111/anec.12511

Pianosi, F., and Wagener, T. (2018). Distribution-based sensitivity analysis from a generic input-output sample. *Environ. Model. Softw.* 108, 197–207. doi:10.1016/j.envsoft.2018.07.019

Pirola, F. T., and Potter, E. K. (1990). Vagal action on atrioventricular conduction and its inhibition by sympathetic stimulation and neuropeptide y in anaesthetised dogs. *J. Auton. Nerv. Syst.* 31, 1–12. doi:10.1016/0165-1838(90)90166-g

Porta, A., Gnecchi-Ruscone, T., Tobaldini, E., Guzzetti, S., Furlan, R., and Montano, N. (2007). Progressive decrease of heart period variability entropy-based complexity during graded head-up tilt. *J. Appl. Physiol.* 103, 1143–1149. doi:10.1152/japplphysiol.00293.2007

Porta, A., Faes, L., Marchi, A., Bari, V., De Maria, B., Guzzetti, S., et al. (2015). Disentangling cardiovascular control mechanisms during head-down tilt via joint transfer entropy and self-entropy decompositions. *Front. Physiol.* 6, 301. doi:10.3389/fphys.2015.00301

Priola, D. V., Curtis, M. B., Anagnostelis, C., and Martinez, E. (1983). Altered nicotinic sensitivity of AV node in surgically denervated canine hearts. *Am. J. Physiol.* 245, 27–32. doi:10.1152/ajpheart.1983.245.1.H27

Rashidi, A., and Khodarahmi, I. (2005). Nonlinear modeling of the atrioventricular node physiology in atrial fibrillation. *J. Theor. Biol.* 232, 545–549. doi:10.1016/j.jtbi.2004.08.033

Richman, J. S., and Moorman, J. R. (2000). Physiological time-series analysis using approximate entropy and sample entropy. *Am. J. Physiol. Heart Circ. Physiol.* 278, 2039–2049. doi:10.1152/ajpheart.2000.278.6.H2039

Sassi, R., Cerutti, S., Lombardi, F., Malik, M., Huikuri, H. V., Peng, C.-K., et al. (2015). Advances in heart rate variability signal analysis: Joint position statement by the e-cardiology ESC working group and the European heart rhythm association co-endorsed by the asia pacific heart rhythm society. *Europace* 17, 1341–1353. doi:10.1093/europace/euv015

Shen, M. J., and Zipes, D. P. (2014). Role of the autonomic nervous system in modulating cardiac arrhythmias. *Circ. Res.* 114, 1004–1021. doi:10.1161/CIRCRESAHA.113.302549

Spear, J. F., and Moore, E. N. (1973). Influence of brief vagal and stellate nerve stimulation on pacemaker activity and conduction within the atrioventricular conduction system of the dog. *Circ. Res.* 32, 27–41. doi:10.1161/01.RES.32.1.27

Trautwein, W. (1963). Generation and conduction of impulses in the heart as affected by drugs. *Pharmacol. Rev.* 15, 277–332.

Wallman, M., and Sandberg, F. (2018). Characterisation of human AV-nodal properties using a network model. *Med. Biol. Eng. Comput.* 56, 247–259. doi:10.1007/s11517-017-1684-0

West, T. C., and Toda, N. (1967). Response of the A-V node of the rabbit to stimulation of intracardiac cholinergic nerves. *Circ. Res.* 20, 18–31. doi:10.1161/01.res.20.1.18

Yentes, J. M., Hunt, N., Schmid, K. K., Kaipust, J. P., McGrath, D., and Stergiou, N. (2013). The appropriate use of approximate entropy and sample entropy with short data sets. *Ann. Biomed. Eng.* 41, 349–365. doi:10.1007/s10439-012-0668-3

Paper II

ECG-based estimation of respiration-induced autonomic modulation of AV nodal conduction during atrial fibrillation.

Felix Plappert, Gunnar Engström, Pyotr G Platonov, Mikael Wallman, Frida Sandberg

Published in: Frontiers in Physiology, vol. 15, 1281343, 2024

frontiers | Frontiers in Physiology

TYPE Original Research
PUBLISHED 08 May 2024
DOI 10.3389/fphys.2024.1281343

OPEN ACCESS

EDITED BY
Fernando Soares Schlindwein,
University of Leicester, United Kingdom

REVIEWED BY
Julien Oster,
Institut National de la Santé et de la Recherche Médicale (INSERM), France
Cees A. Swenne,
Leiden University Medical Center (LUMC), Netherlands

*CORRESPONDENCE
Felix Plappert,
felix.plappert@bme.lth.se

†These authors share last authorship

RECEIVED 22 August 2023
ACCEPTED 08 April 2024
PUBLISHED 08 May 2024

CITATION
Plappert F, Engström G, Platonov PG, Wallman M and Sandberg F (2024), ECG-based estimation of respiration-induced autonomic modulation of AV nodal conduction during atrial fibrillation. *Front. Physiol.* 15:1281343. doi: 10.3389/fphys.2024.1281343

ECG-based estimation of respiration-induced autonomic modulation of AV nodal conduction during atrial fibrillation

Felix Plappert[1]*, Gunnar Engström[2], Pyotr G. Platonov[3], Mikael Wallman[4†] and Frida Sandberg[1†]

[1]Department of Biomedical Engineering, Lund University, Lund, Sweden, [2]Department of Clinical Sciences, Cardiovascular Research–Epidemiology, Malmö, Sweden, [3]Department of Cardiology, Clinical Sciences, Lund University, Lund, Sweden, [4]Fraunhofer-Chalmers Centre, Department of Systems and Data Analysis, Gothenburg, Sweden

Introduction: Information about autonomic nervous system (ANS) activity may offer insights about atrial fibrillation (AF) progression and support personalized AF treatment but is not easily accessible from the ECG. In this study, we propose a new approach for ECG-based assessment of respiratory modulation in atrioventricular (AV) nodal refractory period and conduction delay.

Methods: A 1-dimensional convolutional neural network (1D-CNN) was trained to estimate respiratory modulation of AV nodal conduction properties from 1-minute segments of RR series, respiration signals, and atrial fibrillatory rates (AFR) using synthetic data that replicates clinical ECG-derived data. The synthetic data were generated using a network model of the AV node and 4 million unique model parameter sets. The 1D-CNN was then used to analyze respiratory modulation in clinical deep breathing test data of 28 patients in AF, where an ECG-derived respiration signal was extracted using a novel approach based on periodic component analysis.

Results: We demonstrated using synthetic data that the 1D-CNN can estimate the respiratory modulation from RR series alone with a Pearson sample correlation of $r = 0.805$ and that the addition of either respiration signal ($r = 0.830$), AFR ($r = 0.837$), or both ($r = 0.855$) improves the estimation.

Discussion: Initial results from analysis of ECG data suggest that our proposed estimate of respiration-induced autonomic modulation, a_{resp}, is reproducible and sufficiently sensitive to monitor changes and detect individual differences. However, further studies are needed to verify the reproducibility, sensitivity, and clinical significance of a_{resp}.

KEYWORDS

atrial fibrillation, atrioventricular node, autonomic nervous system dysfunction, respiration-induced autonomic modulation, convolutional neural network, deep breathing test, network model, ECG

1 Introduction

Atrial fibrillation (AF) is the most common supraventricular tachyarrhythmia (Hindricks et al., 2020). Characteristic of AF is an uncoordinated atrial electrical activation that results in increased and irregular ventricular activity. Atrial fibrillation poses a significant burden to patients, physicians, and healthcare systems globally, and is associated with substantial morbidity and mortality. The recently updated guideline for the diagnosis and management of AF emphasizes that AF is a progressive disease that requires a variety of strategies at different stages, from prevention, lifestyle and risk factor modification, screening and therapy (Joglar et al., 2023). In this context, monitoring of pathophysiological changes associated with AF progression in individual patients can be valuable for the management of persistent AF.

There is a bidirectional relationship between AF and autonomic nervous system (ANS) dysfunction (Linz et al., 2019; Malik et al., 2022). The ANS contributes to the maintenance of AF (Shen and Zipes, 2014; Joglar et al., 2023) and the presence of AF promotes atrial neural remodeling and deficiencies in autonomic afferent reflexes (Wasmund et al., 2003; Yu et al., 2014; Malik et al., 2022). For example, AF patients have shown impaired sensitivity in the arterial baroreceptor reflex, a mechanism that buffers acute changes in arterial blood pressure by modulating both the parasympathetic and sympathetic nervous systems (van den Berg et al., 2001; Miyoshi et al., 2020; Ferreira et al., 2023). Conversely, the restoration of sinus rhythm has been shown to improve the baroreceptor sensitivity (Field et al., 2016), and baroreceptor activation therapy has restored sinus rhythm in a recent case study (Wang et al., 2023).

In normal sinus rhythm (NSR), autonomic dysfunction can be assessed by measuring the heart rate variability (Sassi et al., 2015; Shaffer and Ginsberg, 2017), quantifying autonomic modulation of the sinoatrial (SA) node. However, during AF, the heart rate is instead determined by the rate of fibrillation and the subsequent atrioventricular (AV) nodal modulation, raising the need for alternative approaches to assess autonomic dysfunction. Since the AV node, much like the SA node, is densely innervated by the ANS (George et al., 2017; Hanna et al., 2021), it is an attractive substitute for the assessment of autonomic function under AF. However, the relation between cardiac ANS modulation and AV nodal function under AF is far more complex than that between ANS modulation and SA node function during NSR. This calls for more sophisticated, model-based methods of analysis.

The AV node is characterized by its dual-pathway physiology allowing for parallel conduction of impulses where the two pathways have different electrophysiological properties (George et al., 2017). The fast pathway (FP) exhibits a shorter conduction delay and longer refractory period compared to the slow pathway (SP) (George et al., 2017). The AV nodal refractory period and conduction delay are influenced by the previous activity of conducted and blocked impulses (George et al., 2017; Billette and Tadros, 2019). There have been several AV node models proposed that describe different characteristics of the AV nodal structure and electrophysiology (Cohen et al., 1983; Mangin et al., 2005; Rashidi and Khodarahmi, 2005; Lian et al., 2006; Climent et al., 2011b; Masè et al., 2015; Henriksson et al., 2016; Inada et al., 2017; Wallman and Sandberg, 2018; Karlsson et al., 2021), but our previously proposed model (Plappert et al., 2022) is the first to address autonomic modulation of the AV nodal refractory period and conduction delay. We showed that ANS-induced changes during tilt could be better replicated when scaling the refractory period and conduction delay with a constant factor. Because respiration is a powerful modulator of the reflex control systems, to a large extent via effects on the baroreflex (Piepoli et al., 1997), abnormal respiration-induced autonomic modulation is often an early sign of autonomic dysfunction (Bernardi et al., 2001). For the monitoring of cardiac autonomic modulation in AF patients, the assessment of respiration-induced autonomic modulation seems well-suited because respiration is always present and can be extracted from ECG signals (Varon et al., 2020). Building on the previous AV node model extension, the respiration-induced autonomic modulation could be incorporated by time-varying changes in the modulation of AV nodal refractory period and conduction delay.

Machine learning is vibrant in the field of cardiac electrophysiology with a rapidly growing number of applications (Trayanova et al., 2021). However, one main challenge is the acquirement of large amounts of data for proper training and validation. In recent years, a few studies have been performed in which synthetic data has been generated for the training of neural networks which are then used on clinical data. For example, synthetic images were generated to train neural networks to track cardiac motion and calculate cardiac strain (Loecher et al., 2021), estimate tensors from free-breathing cardiac diffusion tensor imaging (Weine et al., 2022), and predict end-diastole volume, end-systole volume, and ejection fraction (Gheorghita et al., 2022). Furthermore, synthetic photoplethysmography (PPG) signals were generated to detect bradycardia and tachycardia (Sološenko et al., 2022), and synthetic electrocardiogram (ECG) signals were generated to detect r-waves during different physical activities and atrial fibrillation (Kaisti et al., 2023), and to predict the ventricular origin in outflow tract ventricular arrhythmias (Doste et al., 2022).

This study aims to develop and evaluate a method to extract respiration-induced autonomic modulation in the AV node conduction properties from ECG data in AF. We present a novel approach to extract respiration signals from several ECG leads based on the periodic component analysis (Sameni et al., 2008). In addition, we present a novel extension to our previously proposed AV node network model accounting for respiration-induced autonomic modulation of AV nodal refractory period and conduction delay. Furthermore, we estimate the magnitude of respiration-induced autonomic modulation using a 1-dimensional convolutional neural network that was trained on synthetic 1-min segments of RR series, respiration signals, and average atrial fibrillatory rate which replicate clinical data. The trained network was used to analyze data from 28 AF patients performing a deep breathing task including slow metronome breathing at a respiration rate of 6 breaths/min. During NSR, slower breathing causes an increased respiration-induced autonomic modulation with a maximum HRV response typically observed at a respiration rate of 6 breaths/min (Russo et al., 2017). Hence, we hypothesize that the respiration-induced autonomic modulation in the AV

node conduction properties is strengthened during the deep breathing task.

2 Materials and methods

First, the clinical deep breathing test data from patients in atrial fibrillation is described in Section 2.1. In Section 2.2, the extraction of RR series and atrial fibrillatory rate (AFR) from ECG are described. Moreover, Section 2.2 covers the extraction of ECG-derived respiration (EDR) signals using a novel approach based on periodic component analysis. A description of the extended AV network model accounting for respiration-induced autonomic modulation is given in Section 2.3, as well as a description of how the simulated datasets are generated. In Section 2.4, the architecture of a 1-dimensional convolutional neural network (1D-CNN) that is used to estimate the magnitude of respiratory modulation from ECG recordings is described together with the training and testing of the neural network. Finally, the CNN is used to estimate the respiration-induced autonomic modulation from the clinical ECG-derived features and the estimates are analyzed.

2.1 ECG data

The dataset of the clinical deep breathing test consisted of 12-lead ECG recordings with a sampling rate of 500 Hz from individuals with AF participating in the SCAPIS study (Bergström et al., 2015). The participants in the SCAPIS study were from the Swedish general population aged 50–64 years. A subset of the SCAPIS cohort (5136 participants) performed a deep breathing test (Engström et al., 2022). Of this subset, 28 participants with complete data were in AF at the time of recording (Abdollahpur et al., 2022). The clinical characteristics of that subset are listed in Table 1. The deep breathing test started with the participants resting in a supine position while breathing normally for 5 minutes. Following this, the participants performed slow metronome breathing at a respiration rate of 0.1 Hz for 1 minute. During the slow metronome breathing, a nurse guided the participants to inhale for 5 seconds and exhale for 5 seconds, for a total of six breathing cycles.

TABLE 1 Clinical characteristics of study population.

	Number
Age	60.1 ± 4.0 [50.1-64.9]
Men	23 (82%)
BMI	31.8 ± 7.2 [18.8-50.8]
Systolic BP	124 ± 23 [90-188]
Diastolic BP	79.9 ± 11 [61-104]
Hypertension *	17 (61%)
Diabetes	2 (7%)
Never smokers	9 (32%)
Heart failure	2 (7%)
Previous AMI or angina	2 (7%)
Beta blocker	15 (54%)
Ca-antagonist	6 (21%)
Antiarrhythmic drug	4 (14%)

* ≥140/90 mmHg or treatment for hypertension. Values are given in the following formats: number, mean ± SD, [range]; BP, blood pressure.

2.2 ECG data processing

2.2.1 Extraction of RR series

ECG preprocessing and QRS complex detection were performed using the CardioLund ECG parser (www.cardiolund.com). The CardioLund ECG parser classified QRS complexes based on their QRS morphology. Only QRS complexes with dominant QRS morphology were considered in the computation of the RR series.

The RR series were computed from intervals between R-peaks taken from consecutive QRS complexes with dominant QRS morphology, and the time of each RR interval was set to the time of the first R-peak in each interval. The resulting non-uniformly sampled RR series were interpolated to a uniform sampling rate of 4 Hz using piecewise cubic Hermite polynomials as implemented in MATLAB ('pchip', version R2023a, RRID:SCR_001622).

2.2.2 Estimation of atrial fibrillatory rate

The AFR was used to obtain information about the atrial arrival process. Briefly, the estimation of the AFR involved the extraction of an f-wave signal by means of spatiotemporal QRST-cancellation (Stridh and Sörnmo, 2001) and estimation of an f-wave frequency trend by fitting two complex exponential functions to the extracted f-wave signal from ECG lead V1 as proposed in (Henriksson et al., 2018). The two exponential functions were characterized by a fundamental frequency f and its second harmonic, respectively; f was fitted within the range $f_{max}^{Welch} \pm 1.5$ Hz, where f_{max}^{Welch} denotes the maximum of the Welch periodogram of ECG lead V1 in the range 4–12 Hz. The results for the deep breathing data have been previously presented in (Abdollahpur et al., 2022). The estimated AFR signal has a sampling rate of 50 Hz.

2.2.3 Extraction of lead-specific EDR signals

All steps of the extraction algorithm that are described in the following were applied to 1-min segments of the lead-specific EDR signals taken from a 1-min running window. The lead-specific EDR signals were computed with the slope range method (Kontaxis et al., 2020) for the eight ECG leads V1-V6, I, and II. Only eight out of 12 ECG leads were used, because the information in the leads III, aVF, aVL, and aVR can also be derived from lead I and II. The slope range method uses the peak-to-peak difference in the first derivative of the QRS complex to quantify the variations in the QRS morphology that are assumed to reflect the respiratory activity and are caused, for example, by periodic changes in electrode positions relative to the heart.

Only QRS complexes with dominant QRS morphology (cf. Section 2.2.1) were considered when applying the slope-range method. Further, a QRS complex was excluded as an outlier from analysis if the slope range value of any of the leads was outside the mean ± 3 std of the slope range values of that lead. The lead-specific non-uniformly sampled EDR signals were interpolated to a uniform sampling rate of 4 Hz using the modified Akima algorithm as implemented in MATLAB ('makima', version R2023a, RRID:SCR_001622). A matrix containing the resampled lead-specific EDR signals $\mathbf{X}' = [\mathbf{x}'_1, \ldots, \mathbf{x}'_8]^T$ of dimension $8 \times N$ was constructed, where $N = 240$ corresponds to the length of the 1-min segment. To remove baseline-wander in $\mathbf{X}'$, a Butterworth highpass filter of order 4 with a cut-off frequency of 0.08 Hz was applied separately for each lead $\mathbf{x}'$. The filtered $\mathbf{X}'$ was normalized to zero-mean and signals shorter than 1 min were zero-padded to create $\mathbf{X}$ containing 1-min segments. A set $\mathcal{S}_{seg}$ was created containing all $\mathbf{X}_i$, where $i = 1, \ldots, I$ denotes all I possible choices of 1-min segments of the lead-specific EDR signals from one recording.

2.2.4 Extraction of joint-lead EDR signals

The joint-lead EDR signal was extracted from $\mathbf{X}$ using a modified version of the periodic component analysis (πCA) (Sameni et al., 2008), summarized in Algorithm 1. The matrix $\mathbf{X}$ was whitened for its elements to be uncorrelated and to have unit variance. The whitened lead-specific EDR signals $\mathbf{Z}$ were computed as

$$\mathbf{Z} = \mathbf{D}^{-1/2}\mathbf{E}^{\mathrm{T}}\mathbf{X}, \tag{1}$$

for all $\mathbf{X}_i$ in $\mathcal{S}_{seg}$ **do**
  $\mathbf{X}_i$ is whitened according to Eq. 1 to obtain $\mathbf{Z}_i$
  for all $\tau_j \in [10, 40]$ **do**
    obtain $\mathbf{w}_j$ by solving the generalized eigenvalue problem of matrix pair $(\overline{\mathbf{C}}_{\mathbf{z}}(\tau_j), \overline{\mathbf{C}}_{\mathbf{z}}(0))$
    compute $\epsilon(\mathbf{w}_j, \tau_j, \mathbf{Z}_i)$ according to Eq. 2
  end for
end for
compute $\tau^* = \min_{\tau_j}\left(\sum_{\mathcal{S}_{seg}} \epsilon(\mathbf{w}_j, \tau_j, \mathbf{Z}_i)\right)$
for all $\mathbf{Z}_i$ in $\mathcal{S}_{seg}$ **do**
  $\mathcal{S}_\tau = \emptyset$
  for all $\tau_j \in [10, 40]$ **do**
    if $\epsilon(\mathbf{w}_j, \tau_j, \mathbf{Z}_i) \leq \epsilon(\mathbf{w}_j, \tau_{j-1}, \mathbf{Z}_i) \vee \tau_j == 10$ **then**
      if $\epsilon(\mathbf{w}_j, \tau_j, \mathbf{Z}_i) \leq \epsilon(\mathbf{w}_j, \tau_{j+1}, \mathbf{Z}_i) \vee \tau_j == 40$ **then**
        add τ_j to $\mathcal{S}_\tau$
      end if
    end if
  end for
  set τ_{resp} as value in $\mathcal{S}_\tau$ closest to τ^*
  obtain $\mathbf{w}_{resp}$ by solving the generalized eigenvalue problem of matrix pair $(\overline{\mathbf{C}}_{\mathbf{z}}(\tau_{resp}), \overline{\mathbf{C}}_{\mathbf{z}}(0))$
  $\mathbf{s}^*_i = \mathbf{w}^T_{resp}\mathbf{Z}_i \cdot \mathrm{sign}\left(\sum \mathbf{w}_{resp}\right)$
  $f_{resp,\,i} = f_s/\tau_{resp}$
end for

Algorithm 1. Extraction of joint-lead EDR signals.

where $\mathbf{D}$ is the diagonal matrix of eigenvalues of the covariance matrix $\mathbf{C}_{\mathbf{X}} = E\{\mathbf{X}\mathbf{X}^{\mathrm{T}}\}$, and the columns of the matrix $\mathbf{E}$ are the unit-norm eigenvectors of $\mathbf{C}_{\mathbf{X}}$.

The outputs of the πCA are a joint-lead EDR signal $\mathbf{s}$ of dimension $1 \times N$ and its corresponding lag τ. The assumption of the πCA is that $\mathbf{s} = \mathbf{w}^{\mathrm{T}}\mathbf{Z}$ is a linear mixture of the whitened lead-specific EDR signals. The aim is to find a solution for $\mathbf{s}$ with a maximal periodic structure. The periodic structure of $\mathbf{s}$ is characterized by $\epsilon(\mathbf{w}, \tau, \mathbf{Z})$, which quantifies non-periodicity (Sameni et al., 2008) and is defined as

$$\epsilon(\mathbf{w}, \tau, \mathbf{Z}) = \frac{\sum_n |s(n+\tau) - s(n)|^2}{\sum_n |s(n)|^2} = 2\left[1 - \frac{\mathbf{w}^{\mathrm{T}}\overline{\mathbf{C}}_{\mathbf{z}}(\tau)\,\mathbf{w}}{\mathbf{w}^{\mathrm{T}}\overline{\mathbf{C}}_{\mathbf{z}}(0)\,\mathbf{w}}\right], \tag{2}$$

where $s(n)$ is the n:th element of $\mathbf{s}$. We solved the generalized eigenvalue problem (GEP) of the lag-dependent matrix pair $(\overline{\mathbf{C}}_{\mathbf{z}}(\tau), \overline{\mathbf{C}}_{\mathbf{z}}(0))$ to obtain a full matrix $\mathbf{V}$ whose columns correspond to the right eigenvectors and a diagonal matrix $\mathbf{U}$ of generalized eigenvalues so that $\overline{\mathbf{C}}_{\mathbf{z}}(\tau)\mathbf{V} = \overline{\mathbf{C}}_{\mathbf{z}}(0)\mathbf{V}\mathbf{U}$ (Sameni et al., 2008). Here, $\overline{\mathbf{C}}_{\mathbf{z}}(\tau) = [\mathbf{C}_{\mathbf{z}}(\tau) + (\mathbf{C}_{\mathbf{z}}(\tau))^{\mathrm{T}} + \mathbf{C}_{\mathbf{z}}(-\tau) + (\mathbf{C}_{\mathbf{z}}(-\tau))^{\mathrm{T}}]/4$ for some lag τ is a modified lagged covariance matrix, which is always symmetric, unlike the time lagged covariance matrix $\mathbf{C}_{\mathbf{z}}(\tau) = E_n\{\mathbf{z}(n)\mathbf{z}(n-\tau)^{\mathrm{T}}\}$, where $\mathbf{z}(n)$ is the n:th column of $\mathbf{Z}$ and $E_n\{\cdot\}$ indicates averaging over n. The weight vector $\mathbf{w} = [w_1, \ldots, w_8]^{\mathrm{T}}$ that minimizes $\epsilon(\mathbf{w}, \tau, \mathbf{Z})$ is obtained as the first column of $\mathbf{V}$ (Sameni et al., 2008). In the present study, $\epsilon(\mathbf{w}, \tau, \mathbf{Z})$ is also used to quantify signal quality, where a lower value of $\epsilon(\mathbf{w}, \tau, \mathbf{Z})$ corresponds to a more periodic signal assumed to have a higher SNR.

As τ is unknown, $\epsilon(\mathbf{w}, \tau, \mathbf{Z})$ was minimized for all integer values of τ between 10 and 40, corresponding to respiration rates between 0.1 and 0.4 Hz. To improve the robustness of the πCA for signals with low quality, a τ^* was determined in an intermediate step that corresponds to a global minimum of $\epsilon(\mathbf{w}, \tau, \mathbf{Z})$ over all 1-min segments in $\mathcal{S}_{seg}$. It was assumed that there were no significant transient changes in respiration frequency in the clinical data and we determined two different τ^* for each subject; one for normal breathing and one for deep breathing. Then, for each 1-min segment separately, a τ_{resp} was estimated as the local minimum of $\epsilon(\mathbf{w}, \tau, \mathbf{Z})$ closest to τ^*. The respiration frequency estimate $\widehat{f}_{resp} = f_s/\hat{\tau}_{resp}$ results from the estimate $\hat{\tau}_{resp}$ and the sampling rate $f_s = 4$ Hz and is in the range $\widehat{f}_{resp} \in [0.1, 0.4]$ Hz corresponding to the limits set by τ. Finally, the weight vector $\mathbf{w}_{resp}$ for the respiration signal extraction was obtained by solving the GEP of the matrix pair $(\overline{\mathbf{C}}_{\mathbf{z}}(\tau_{resp}), \overline{\mathbf{C}}_{\mathbf{z}}(0))$. The extracted $\mathbf{s} = \mathbf{w}^T_{resp}\mathbf{Z}$ was normalized to unit variance. An ambiguity of πCA is that the sign of $\mathbf{s}$ is undetermined. The sign of the joint-lead EDR signal was selected as $\mathbf{s}^* = \mathbf{s} \cdot \mathrm{sign}\left(\sum \mathbf{w}_{resp}\right)$, where $\Sigma\mathbf{w}_{resp}$ denotes the sum of the elements in the vector $\mathbf{w}_{resp}$. This was done under the assumption that all lead-specific EDR signals are in phase.

2.2.5 Estimates from clinical data

The joint-lead EDR signal extraction from Section 2.2.4 was applied to all 1-min segments $\mathbf{X}$ in $\mathcal{S}_{seg}$ for each patient and recording. Segments $\mathbf{X}$ were excluded from further analysis if they do not satisfy the following three criteria, for which a valid QRS complex has a dominant QRS morphology and is not classified as outlier based on its slope range values: *i*) the maximum distance between valid QRS complexes is 2 s; *ii*) the minimum number of

valid QRS complexes in a 1-min segment is 48; *iii*) the minimum number of valid QRS complexes in a 1-min segment is 80% of the normal-to-normal average heart rate of the 1-min segment. After exclusion, several sets of non-overlapping 1-min segments could be created from the remaining $\mathbf{X}$. Out of these, the set $\mathcal{S}^*_{seg}$ that resulted in the smallest sum of $\epsilon(\mathbf{w}_{resp}, \tau_{resp}, \mathbf{Z})$ was chosen, and used to produce joint-lead EDR signals $\mathcal{X}^{Clin}_{Resp}$ of dimension $1 \times N$ as described in Section 2.2.4. In addition, the corresponding 1-min RR series $\mathcal{X}^{Clin}_{RR}$ of dimension $1 \times N$ was extracted from the RR series obtained in Section 2.2.1. We estimated the mean arrival rate of atrial impulses to the AV node $\hat{\mu}$ as $1000/\overline{AFR}$, where $\overline{AFR}$ is the average AFR-trend within each of the selected 1-min windows as described in Section 2.2.2. To match the dimensions of $\mathcal{X}^{Clin}_{RR}$ and $\mathcal{X}^{Clin}_{Resp}$, $\hat{\mu}$ was then repeated N times to produce $\mathcal{X}^{Clin}_{AFR}$ of dimension $1 \times N$. From the clinical data, a maximum of five non-overlapping 1-min long segments in normal breathing and one segment in deep breathing was obtained for $\mathcal{X}^{Clin}_{RR}$, $\mathcal{X}^{Clin}_{Resp}$ and $\mathcal{X}^{Clin}_{AFR}$.

2.3 Simulated data

2.3.1 Network model of the human atrioventricular node

The atrioventricular node is modeled by a network of 21 nodes (cf. Figure 1). The presented AV node model was initially proposed in (Wallman and Sandberg, 2018), updated with minor modifications in (Karlsson et al., 2021), and extended using constant scaling factors A_R and A_D for the refractory period and conduction delay to account for the effect of changes in autonomic modulation in (Plappert et al., 2022). The slow pathway (SP) and fast pathway (FP) are described by two chains of 10 nodes each, which are only connected at their last nodes. Impulses enter the AV node model simultaneously at the first node of each pathway. Within the pathways and between their last nodes, the impulses are conducted bidirectionally to allow for retrograde conduction. The last nodes of the two pathways are connected to an additional coupling node (CN), through which the impulses leave the model.

Each node represents a section of the AV node and is characterized by an individual refractory period $R^P(\Delta t_k, A^P(t), \boldsymbol{\theta}^P_R)$ and conduction delay $D^P(\Delta t_k, A^P(t), \boldsymbol{\theta}^P_D)$ defined as

$$R^P\left(\Delta t_k, A^P(t), \boldsymbol{\theta}^P_R\right) = A^P(t)\left(R^P_{min} + \Delta R^P\left(1 - e^{-\Delta t_k/\tau^P_R}\right)\right) \quad (3)$$

$$D^P\left(\Delta t_k, A^P(t), \boldsymbol{\theta}^P_D\right) = A^P(t)\left(D^P_{min} + \Delta D^P e^{-\Delta t_k/\tau^P_D}\right) \quad (4)$$

Where $P \in \{SP, FP, CN\}$ denotes the pathway. The refractory period and conduction delay are defined by fixed model parameters for the refractory period $\boldsymbol{\theta}^P_R$ and conduction delay $\boldsymbol{\theta}^P_D$ as well as model states for the diastolic interval Δt_k and respiratory modulation $A^P(t)$. Each pathway has a separate set of fixed model parameters for the refractory period $\boldsymbol{\theta}^P_R = [R^P_{min}, \Delta R^P, \tau^P_R]$ and conduction delay $\boldsymbol{\theta}^P_D = [D^P_{min}, \Delta D^P, \tau^P_D]$, where R^P_{min} is the minimum refractory period, ΔR^P is the maximum prolongation of the refractory period, τ^P_R is a time constant, D^P_{min} is the minimum conduction delay, ΔD^P is the maximum prolongation of the conduction delay and τ^P_D is a time constant. For clarity, the notation of $R^P(\cdot, A^P(t), \cdot)$ and $D^P(\cdot, A^P(t), \cdot)$ are specified with dots when the replaced parameters or model states are currently not discussed.

The scaling factor $A^P(t)$ accounts for the effect of changes in autonomic modulation on the refractory period $R^P(\cdot, A^P(t), \cdot)$ and the conduction delay $D^P(\cdot, A^P(t), \cdot)$. The time-varying scaling factor $A^P(t)$ is common between the SP and FP, defined in Eq. 5 as

$$A^{SP}(t) = A^{FP}(t) = 1 + \frac{a_{resp}}{2}\sin\left(2\pi t f_{resp}\right), \quad (5)$$

with a constant respiratory frequency f_{resp} and peak-to-peak amplitude a_{resp}. The scaling factor of the refractory period and conduction delay of the CN is described by $A^{CN} = 1$ and not modulated by respiration.

The electrical excitation propagation through the AV node is modeled as a series of impulses that can either be conducted or blocked by a node. An impulse is conducted to all adjacent nodes, if the interval Δt_k between the k:th impulse arrival time t_k and the end of the (k–1):th refractory period, computed as

$$\Delta t_k = t_k - t_{k-1} - R^P(\Delta t_{k-1}, \cdot, \cdot) \quad (6)$$

is positive. Then, the time delay between the arrival of an impulse at a node and its transmission to all adjacent nodes is given by the conduction delay $D^P(\Delta t_k, \cdot, \cdot)$. If Δt_k is negative, the impulse is blocked due to the ongoing refractory period $R^P(\Delta t_{k-1}, \cdot, \cdot)$. After an impulse is conducted, $R^P(\Delta t_k, \cdot, \cdot)$ and $D^P(\Delta t_k, \cdot, \cdot)$ of the current node are updated according to Eqs 3, 4, 6. Details about how the impulses are processed chronologically and node by node, using a priority queue of nodes and sorted by impulse arrival time, can be found in (Wallman and Sandberg, 2018).

The input to the AV node mode is a series of atrial impulses during AF, with inter-arrival times modeled according to a Pearson Type IV distribution (Climent et al., 2011a). The AA series is generated with a point process with independent inter-arrival times and is completely characterized by the four parameters of the Pearson Type IV distribution, namely, the mean μ, standard deviation σ, skewness γ and kurtosis κ.

The output of the AV node model is a series of ventricular impulses, where t^V_q denotes the time of the q:th ventricular impulse. As the refractory period $R^P(\Delta t_k, \cdot, \cdot)$ and conduction delay $D^P(\Delta t_k, \cdot, \cdot)$ are history-dependent, the first 1,000 ventricular impulses leaving the AV node model are excluded from analysis to avoid transient effects.

2.3.2 Simulation of AV nodal conduction

For the training and validation, a dataset with 2 million unique parameter sets was generated. This dataset was divided into 20 datasets with 100,000 parameter sets each, where a dataset was either used for training or validation of one of ten realizations of the convolutional neural network (CNN) that is described in Section 2.4.2. Simulations were performed with each parameter set using the AV node model described in Section 2.3.1. For each simulation, a series of 11,000 AA intervals was generated using the Pearson Type IV distribution, defined by the four parameters μ, σ, γ, and κ. The parameter μ was randomly drawn from $\mathcal{U}[100, 250]$ ms and σ was randomly drawn from $\mathcal{U}[15, 30]$ ms. The parameters γ and κ were kept fixed at 1 and 6, respectively, since they cannot be estimated from the f-waves of the ECG (Plappert et al., 2022). Negative AA intervals were excluded from the impulse series. The model parameters for the refractory period $\boldsymbol{\theta}^P_R$ and conduction delay $\boldsymbol{\theta}^P_D$ of the SP and FP were drawn from bounded uniform

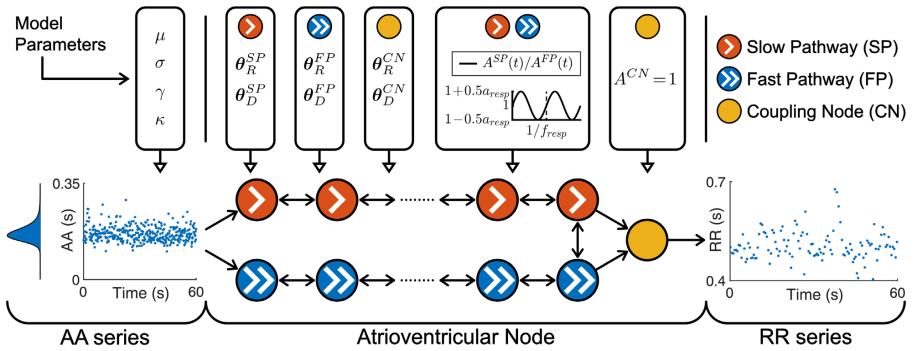

FIGURE 1
A schematic representation of the AV node model. Retrograde conduction was possible within the AV node model. For simplicity, only a subset of the ten nodes in each pathway is shown. Note that the atrioventricular node used different θ_R^P and θ_D^P for the three different pathways, the same time-varying $A^P(t)$ for SP and FP and a constant A^{CN} = for CN.

TABLE 2 AV Node model parameters used for simulated data.

Parameters		P ≡SP (ms)	P ≡FP (ms)	P ≡CN (ms)
θ_R^P	R_{min}^P	$\mathcal{U}[250,600]$	$\mathcal{U}[250,600]$	250
	ΔR^P	$\mathcal{U}[0,600]$	$\mathcal{U}[0,600]$	0
	τ_R^P	$\mathcal{U}[50,300]$	$\mathcal{U}[50,300]$	1
θ_D^P	D_{min}^P	$\mathcal{U}[0,30]$	$\mathcal{U}[0,30]$	0
	ΔD^P	$\mathcal{U}[0,75]$	$\mathcal{U}[0,75]$	0
	τ_D^P	$\mathcal{U}[50,300]$	$\mathcal{U}[50,300]$	1

distributions and the model parameters of the CN were kept fixed according to Table 2. The given ranges were in line with our previous work (Plappert et al., 2022). The model parameters for the respiration-induced autonomic modulation and simulated respiration signal that are used in Section 2.3.3 were also drawn from bounded uniform distributions, with a_{resp} randomly drawn from $\mathcal{U}[-0.1,0.5]$, f_{resp} randomly drawn from $\mathcal{U}[0.1,0.4]$ Hz and η randomly drawn from $\mathcal{U}[0.2,4]$. For testing, another dataset with 2 million unique parameter sets was generated using the same ranges listed above, except for a_{resp}, which was randomly drawn from $\mathcal{U}[0,0.4]$.

When sampling, initially a value for a_{resp} was drawn from a uniform distribution. To exclude non-physiological parameter sets from the dataset, we resampled the rest of the parameters until the following five selection criteria were met: 1) the slow pathway in every parameter set must have a higher conduction delay $D^{SP}(\Delta t_k,\cdot,\cdot) > D^{FP}(\Delta t_k,\cdot,\cdot)$ and lower refractory period $R^{SP}(\Delta t_k,\cdot,\cdot) < R^{FP}(\Delta t_k,\cdot,\cdot)$ than the fast pathway for all Δt_k; 2) the resulting average RR interval has to fall within the range of 300 ms–1,000 ms, which corresponds to heart rates between 60 bpm and 200 bpm; 3) the resulting root mean square of successive RR interval differences (RR RMSSD) has to be above 100 ms; 4) the resulting sample entropy of the RR series has to be above 1; 5) the relative contribution of the respiration frequency in the frequency spectrum of the RR series with zero-mean $F_{RR}(f_{resp})/\Sigma_f F_{RR}(f)$ has to be below 7% to exclude RR series with visible periodicity. Note that the frequency spectrum is computed from the RR series with 240 samples and the sampling rate of 4 Hz.

Similar to the clinical data described in Section 2.2.1, RR series were computed from intervals between the simulated ventricular impulses, and the time of each RR interval sample was set to the time of the first ventricular impulse. The resulting non-uniformly sampled RR series were interpolated to a uniform sampling rate of 4 Hz using piecewise cubic hermite interpolating polynomials as implemented in MATLAB ('pchip', version R2023a, RRID:SCR_001622). The simulated RR series were cut into 1-min segments of length $N = 240$, resulting in RR series $\mathcal{X}_{RR}^{Sim}$ of dimension $1 \times N$. For each RR series, μ was repeated N times to form a vector $\mathcal{X}_{AFR}^{Sim}$ of dimension $1 \times N$, corresponding to the mean atrial arrival rate.

2.3.3 Modelling respiratory signals

For the modeling of the respiratory signals resembling joint-lead EDR signals (cf. Section 2.2.4), we start with the underlying assumption that respiration can be described according to $m(t) = \sin(2\pi t f_{resp})$, i.e., by a sine wave oscillating at the respiratory frequency f_{resp}. Eight identical lead-specific EDR signals $m_p'(t)$ with $p = 1,\ldots,8$ were created, composed of non-uniform samples of $m(t)$ at the times of the ventricular impulses t_q^V generated by the AV node model. To emulate lead-specific EDR signals, Gaussian noise with standard deviation η was added to all samples of $m_p'(t)$, making them non-identical.

Next, $m_p'(t)$ were processed in five steps to mimic the processing steps for the clinical ECG-derived features (cf. Sections 2.2.3 and 2.2.4): 1) using the same criteria as for the outlier exclusion in the

clinical data, all samples in $m'_p(t)$ for the same ventricular impulse were excluded as outliers, if the value in one of the eight leads was outside the mean ± 3 std, computed for each lead within a 1-min running window; 2) as for the clinical lead-specific EDR signals, the simulated signals $m'_p(t)$ were interpolated to a uniform sampling rate of 4 Hz using the modified Akima algorithm as implemented in MATLAB ('makima', version R2023a, RRID:SCR_001622), resulting in $m'_p(n)$; 3) $m'_p(n)$ were cut into 1-min segments of length $N = 240$ and had the dimension $8 \times N$; 4) the resampled and cut signals are filtered with a Butterworth highpass filter of order 4 with the cut-off frequency 0.08 Hz to remove baseline-wander; 5) a joint-lead EDR signal $\mathcal{X}^{Sim}_{Resp}$ with dimension $1 \times N$ was extracted from $m'_p(n)$ using the periodic component analysis described in Section 2.2.4.

2.4 Estimation of respiratory modulation

2.4.1 Training and estimation using a linear regression model

A linear regression model is used here to estimate the peak-to-peak amplitude of respiration-induced autonomic modulation a_{resp}. The linear regression model $\mathcal{L}_{RR,Resp,AFR}$ was trained using a training dataset $\boldsymbol{\mathcal{X}}^{Sim,Train}$ with the format $\boldsymbol{\mathcal{X}} = [\mathcal{X}^{Sim}_{RR}; \mathcal{X}^{Sim}_{Resp}; \mathcal{X}^{Sim}_{AFR}]$ containing 100,000 parameter sets, as described in Section 2.3.2. The performance of $\mathcal{L}_{RR,Resp,AFR}$ on simulated data was assessed using the testing dataset $\boldsymbol{\mathcal{X}}^{Sim,Test}$ containing 2 million parameter sets, as described in Section 2.3.2. The performance on $\boldsymbol{\mathcal{X}}^{Sim,Test}$ was assessed using the RMSE, Pearson correlation, and coefficient of determination R^2 between the true a_{resp} and estimated $\hat{a}_{resp}$.

2.4.2 Architecture of 1-dimensional convolutional neural network

To estimate the peak-to-peak amplitude of the respiration-induced autonomic modulation, a_{resp}, a 1D-CNN architecture was used as illustrated in Figure 2. The CNN architecture consists of five convolution layers, where each layer l was composed of 100 1D-CNN filters with kernel size $k_{\mathcal{C}} = 3$, stride $s_{\mathcal{C}} = 1$ and dilation factor $d_{\mathcal{C}} = 2^{l-1}$, followed by a rectified linear unit (RELU) and a batch normalization layer. After the five convolution layers, the data passed through a global average pooling layer and dense layer, the output of which is an estimation $\hat{a}_{resp}$. To assess the performance of the CNN with or without the RR series, respiration signal, and mean μ of the AA series, seven versions of the CNN were trained. The respective CNNs and their input data are given as follows: the CNN $\mathcal{C}_{RR}$ was trained on the input data with the format $\boldsymbol{\mathcal{X}} = \mathcal{X}^{Sim}_{RR}$; $\mathcal{C}_{Resp}$ was trained on $\boldsymbol{\mathcal{X}} = \mathcal{X}^{Sim}_{Resp}$; $\mathcal{C}_{AFR}$ was trained on $\boldsymbol{\mathcal{X}} = \mathcal{X}^{Sim}_{AFR}$; $\mathcal{C}_{RR,Resp}$ was trained on $\boldsymbol{\mathcal{X}} = [\mathcal{X}^{Sim}_{RR}; \mathcal{X}^{Sim}_{Resp}]$; $\mathcal{C}_{RR,AFR}$ was trained on $\boldsymbol{\mathcal{X}} = [\mathcal{X}^{Sim}_{RR}; \mathcal{X}^{Sim}_{AFR}]$; $\mathcal{C}_{Resp,AFR}$ was trained on $\boldsymbol{\mathcal{X}} = [\mathcal{X}^{Sim}_{Resp}; \mathcal{X}^{Sim}_{AFR}]$; and $\mathcal{C}_{RR,Resp,AFR}$ was trained on $\boldsymbol{\mathcal{X}} = [\mathcal{X}^{Sim}_{RR}; \mathcal{X}^{Sim}_{Resp}; \mathcal{X}^{Sim}_{AFR}]$.

2.4.3 Training the convolutional neural network

For each CNN version, i.e., $\mathcal{C}_{RR}$, $\mathcal{C}_{Resp}$, $\mathcal{C}_{AFR}$, $\mathcal{C}_{RR,Resp}$, $\mathcal{C}_{RR,AFR}$, $\mathcal{C}_{Resp,AFR}$ and $\mathcal{C}_{RR,Resp,AFR}$, described in Section 2.4.2, ten realizations were trained with unique training and validation datasets, $\boldsymbol{\mathcal{X}}^{Sim,Train}$ and $\boldsymbol{\mathcal{X}}^{Sim,Val}$, respectively, containing 100,000 parameter sets each, as described in Section 2.3.2. The CNNs were trained to estimate the a_{resp} and the weights of the CNN were updated during backpropagation based on the root-mean-square error (RMSE) of the residuals. Every epoch, $\boldsymbol{\mathcal{X}}^{Sim,Train}$ was randomly divided into 20 mini-batches, each containing input data for 5,000 different parameter sets. A cyclical learning rate was set for the training, where the learning rate started at $5 \cdot 10^{-3}$ and was increased and decreased in a 'zig-zag' between $[2 \cdot 10^{-3}, 3 \cdot 10^{-3}, 5 \cdot 10^{-3}, 8 \cdot 10^{-3}, 10 \cdot 10^{-3}]$ every time the RMSE of $\boldsymbol{\mathcal{X}}^{Sim,Val}$ did not improve for 50 epochs (Smith, 2017). The initial learning rate and the minimum and maximum boundary values of the cyclical learning rates were determined using the 'learning rate range test', described in (Smith, 2017). The network was validated after every epoch. The CNN was trained until the RMSE of $\boldsymbol{\mathcal{X}}^{Sim,Val}$ did not improve for 50 epochs for each of the five learning rates, and the network weights giving the lowest validation RMSE was chosen. The estimate $\hat{a}_{resp}$ was computed as the average of the individual estimates of each of the ten CNN realizations.

2.4.4 Estimation of respiratory modulation in simulated data

The performance of the CNN on simulated data was assessed for $\mathcal{C}_{RR}$, $\mathcal{C}_{Resp}$, $\mathcal{C}_{AFR}$, $\mathcal{C}_{RR,Resp}$, $\mathcal{C}_{RR,AFR}$, $\mathcal{C}_{Resp,AFR}$ and $\mathcal{C}_{RR,Resp,AFR}$, using the testing dataset $\boldsymbol{\mathcal{X}}^{Sim,Test}$ described in Section 2.3.2. The total performance on $\boldsymbol{\mathcal{X}}^{Sim,Test}$ was assessed using the RMSE, Pearson sample correlation, and coefficient of determination R^2 between the true a_{resp} and estimated $\hat{a}_{resp}$.

In addition, the performance was assessed over a range of respiration frequencies f_{resp} and characteristics of non-periodicity in the respiration signal $\epsilon(\mathbf{w}, \tau, \mathbf{Z})$, here denoted ϵ. To produce local RMSE estimates $\sigma(f'_{resp}, \epsilon')$ for specific values f'_{resp} and ϵ', the following three steps were applied: 1) a squared difference $\left(a_{resp} - \hat{a}_{resp}\right)^2$ was computed for each of the 2 million parameter sets in $\boldsymbol{\mathcal{X}}^{Sim,Test}$; 2) a weighted average of the 2 million squared differences was computed using a Gaussian kernel centered at f'_{resp} and ϵ' with the standard deviation of 0.015 Hz and 0.075 for the f_{resp} and ϵ, respectively; 3) the square root of the weighted average resulted in $\sigma(f'_{resp}, \epsilon')$.

In the present study, all versions of the CNN were trained and tested using 1-min segments, with one exception: An additional CNN $\mathcal{C}^{2.5min}_{RR,Resp,AFR}$ was trained and tested using $\boldsymbol{\mathcal{X}}^* = [\mathcal{X}^{Sim,2.5}_{RR}; \mathcal{X}^{Sim,2.5}_{Resp}; \mathcal{X}^{Sim,2.5}_{AFR}]$ containing 2.5-minute-long segments to investigate the impact of segment length on the RMSE. For $\mathcal{C}^{2.5min}_{RR,Resp,AFR}$, ten realizations were trained with additional unique training and validation datasets, $\boldsymbol{\mathcal{X}}^{*Sim,Train}$ and $\boldsymbol{\mathcal{X}}^{Sim,Val}$, respectively, containing 100,000 parameter sets each. Apart from the different segment lengths, the additional datasets were generated as described in Section 2.3.2.

2.4.5 Estimation of respiratory modulation in clinical data

The CNN $\mathcal{C}_{RR,Resp,AFR}$ was used for estimating a_{resp} in the clinical deep breathing test data, described in Section 2.1. The clinical estimates were used to investigate differences in $\hat{a}_{resp}$ between deep breathing and normal breathing using Monte Carlo sampling. Using these samples, the probabilities of the following three scenarios were computed for each patient: 1) the highest $\hat{a}_{resp}$ was achieved for deep breathing, 2) the lowest $\hat{a}_{resp}$ was achieved for deep breathing and 3) the highest and lowest $\hat{a}_{resp}$ did not correspond to deep breathing. To draw the samples for each 1-min segment in $\boldsymbol{\mathcal{X}}^{Clin,Test}$, the estimate $\hat{a}_{resp}$ was determined

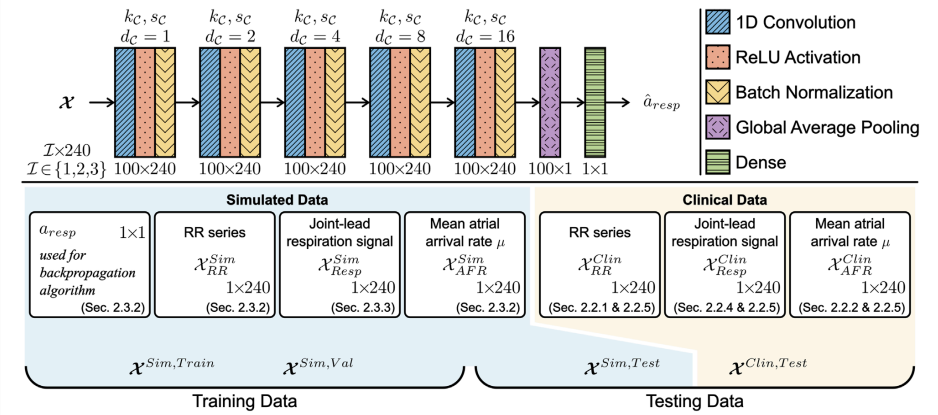

FIGURE 2
The CNN was composed of five 1D convolution layers with 100 filters each. The convolution layers had a kernel size $k_\mathcal{C}$, stride $s_\mathcal{C}$ and dilation factor $d_\mathcal{C}$. Training datasets $\mathcal{X}^{Sim,Train}$, validation datasets $\mathcal{X}^{Sim,Val}$, and testing datasets $\mathcal{X}^{Sim,Test}$ were constructed from the simulated data $\mathcal{X}^{Sim}_{RR}$, $\mathcal{X}^{Sim}_{Resp}$ and $\mathcal{X}^{Sim}_{AFR}$. A testing dataset $\mathcal{X}^{Clin,Test}$ was constructed from the clinical ECG-derived features $\mathcal{X}^{Clin}_{RR}$, $\mathcal{X}^{Clin}_{Resp}$ and $\mathcal{X}^{Clin}_{AFR}$.

using the CNN $\mathcal{C}_{RR,Resp,AFR}$, while the f'_{resp} and ϵ' were estimated by the $\widehat{f}_{resp}$ and $\epsilon(\mathbf{w},\tau,\mathbf{Z})$ described in Section 2.2.4. Next, values of $\hat{a}_{resp}$ were resampled 100,000 times for each 1-min segment in $\mathcal{S}^*_{seg}$. The samples were drawn from Gaussian distributions with $\hat{a}_{resp}$ as mean and $\sigma(f'_{resp},\epsilon')$ described in Section 2.4.4 as standard deviation.

3 Results

3.1 Analysis of clinical data

The length of the interpolated RR series varied between patients depending on the duration of the recordings; during normal breathing, the length of the RR series was in the range between 288 s and 328 s; during deep breathing, the length of the RR series was in the range between 57 s and 72 s. Statistics quantifying the clinical dataset are shown in Table 3. In accordance with the exclusion criteria defined in Section 2.2.5, 98 out of 120 non-overlapping 1-min segments remained in the normal breathing data and 22 out of 28 1-min segments remained in the deep breathing data. Typical examples of a clinical ECG-derived RR series $\mathcal{X}^{Clin}_{RR}$ and joint-lead respiration signal $\mathcal{X}^{Clin}_{Resp}$ during normal breathing and deep breathing, respectively, are shown in Figure 3. The characteristics of these signals, listed in Table 4 are within 1 standard deviation of the population mean (cf. Table 3). Fluctuations in the clinical RR series matching the respiration frequencies were not clearly visible and $F_{RR}(f_{resp})/\Sigma_f F_{RR}(f)$ was always below 7%. The respiration signals estimated from clinical data had $\epsilon(\mathbf{w},\tau,\mathbf{Z})$ ranging between 0.198 and 1.485. The clinical value pairs of $\epsilon(\mathbf{w},\tau,\mathbf{Z})$ and respiration frequency $\widehat{f}_{resp}$ are shown in Figure 4. There was a statistically significant weak negative correlation between $\widehat{f}_{resp}$ and $\epsilon(\mathbf{w},\tau,\mathbf{Z})$ in the clinical data during normal breathing ($r = -.217, p = 0.032$), but no significant correlation during deep breathing.

3.2 Simulated RR series and respiration signals

The statistics quantifying $\mathcal{X}^{Sim,Train}$, $\mathcal{X}^{Sim,Val}$ and $\mathcal{X}^{Sim,Test}$ are shown in Table 3 together with $\mathcal{X}^{Clin,Test}$. The simulated datasets were created according to the description in Section 2.3 and compared to the clinical data using the unpaired t-test. It should be noted that although there are significant differences between the characteristics of the clinical and simulated data, the distributions of the simulated data cover the distribution of the clinical data. The heart rate was on average slightly faster and more regular in $\mathcal{X}^{Sim}$ than in $\mathcal{X}^{Clin}$, as indicated by the differences in RR mean, RR RMSSD, and RR sample entropy. Further, the RR series in $\mathcal{X}^{Sim}$ showed on average more visible fluctuations matching the respiration frequency compared to the RR series in $\mathcal{X}^{Clin}$, as indicated by the difference in $F_{RR}(f_{resp})/\Sigma_f F_{RR}(f)$. The $\overline{AFR}$ was on average slightly lower in $\mathcal{X}^{Sim}$ than in $\mathcal{X}^{Clin}$, whereas f_{resp} was slightly higher. In normal breathing, ϵ in $\mathcal{X}^{Clin}$ was comparable to $\mathcal{X}^{Sim}$; however, in deep breathing, ϵ was lower in $\mathcal{X}^{Clin}$ than in $\mathcal{X}^{Sim}$.

Examples of a simulated RR series $\mathcal{X}^{Sim}_{RR}$ and joint-lead respiration signal $\mathcal{X}^{Sim}_{Resp}$ resembling clinical signals during normal breathing and deep breathing, respectively, are shown in Figure 3. The signals were chosen based on similarities to the clinical ECG-derived signals in the RR series characteristics and respiration signal morphology. The characteristics of these signals are listed in Table 4. Note, that while the peak-to-peak amplitude of

TABLE 3 Characteristics of clinical and simulated data.

	Clinical data $\mathcal{X}^{Clin,Test}$		Simulated data	
	Normal breathing	Deep breathing	Training Data $[\mathcal{X}^{Sim,Train}; \mathcal{X}^{Sim,Val}]$	Testing Data $\mathcal{X}^{Sim,Test}$
Number of $\boldsymbol{\mathcal{X}}$	98	22	$10 \cdot 2 \cdot 100{,}000$	2,000,000
RR mean (ms)	763 ± 173	747 ± 162	$676 \pm 164^{\dagger}$	$676 \pm 164^{\dagger}$
RR RMSSD (ms)	262 ± 100	230 ± 60	$188 \pm 60^{\dagger,\ddagger}$	$185 \pm 58^{\dagger,\ddagger}$
RR sample entropy	2.08 ± 0.49	2.18 ± 0.63	$1.53 \pm 0.39^{\dagger,\ddagger}$	$1.52 \pm 0.38^{\dagger,\ddagger}$
$F_{RR}(f_{resp})/\Sigma_f F_{RR}(f)(\%)$	2.5 ± 1.3	1.1 ± 0.8	$3.4 \pm 1.8^{\dagger,\ddagger}$	$3.3 \pm 1.7^{\dagger,\ddagger}$
$\overline{AFR}$(Hz)	6.99 ± 0.7	6.95 ± 0.71	$5.97 \pm 1.57^{\dagger,\ddagger}$	$5.96 \pm 1.57^{\dagger,\ddagger}$
f_{resp}(Hz)	0.220 ± 0.067	0.107 ± 0.015	$0.263 \pm 0.085^{\dagger,\ddagger}$	$0.261 \pm 0.085^{\dagger,\ddagger}$
ϵ	0.66 ± 0.25	0.44 ± 0.15	$0.64 \pm 0.27^{\ddagger}$	$0.64 \pm 0.27^{\ddagger}$
a_{resp}	0.282 ± 0.101	0.285 ± 0.131	$0.200 \pm 0.173^{\dagger,\ddagger}$	$0.200 \pm 0.115^{\dagger,\ddagger}$

$^{\dagger}p < 0.05$ vs. normal breathing. $^{\ddagger}p < 0.05$ vs. deep breathing. The training data is divided into 20 datasets with equal size to train the 10 realizations of the CNN with unique $\boldsymbol{\mathcal{X}}^{Sim,Train}$ and $\boldsymbol{\mathcal{X}}^{Sim,Val}$. The variables $\overline{AFR}$, f_{resp}, and a_{resp} characterize estimates in the clinical data and model parameters in the simulated data.

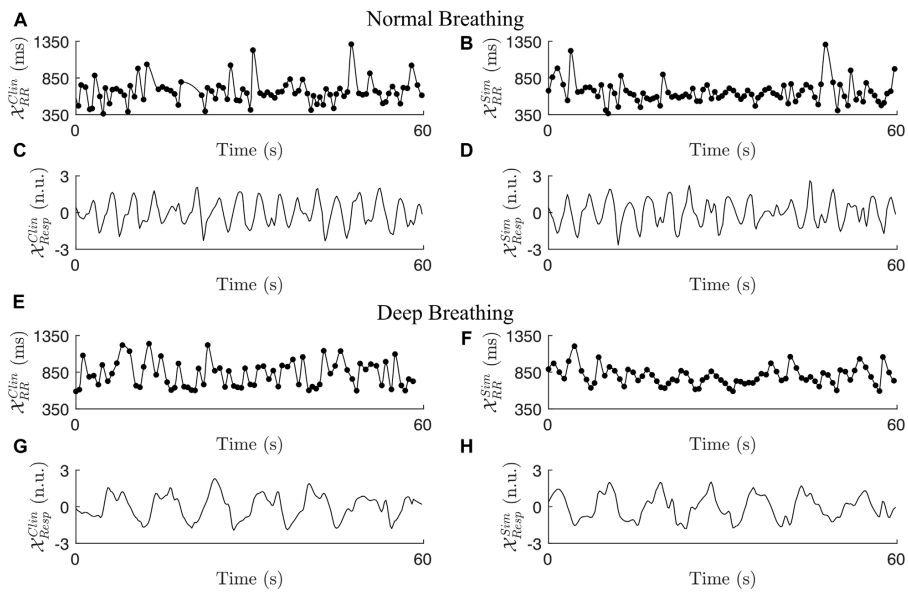

FIGURE 3
Two examples of clinical RR series (A + E), simulated RR series (B + F), clinical respiration signals (C + G), and simulated respiration signals (D + H) during normal breathing **(A–D)** and deep breathing **(E–H)**.

TABLE 4 Characteristics of the clinical and simulated examples shown in Figure 3.

Signals	RR mean (ms)	RR RMSSD (ms)	RR sample entropy	a_{resp}	f_{resp} (Hz)	η	$\epsilon(\mathbf{w},\tau,\mathbf{Z})$
A/C	661	250	1.85	-	0.286	-	0.47
B/D	651	204	1.91	0.36	0.288	2.48	0.76
E/G	818	251	2.28	-	0.118	-	0.44
F/H	792	138	1.97	0.05	0.116	1.46	0.45

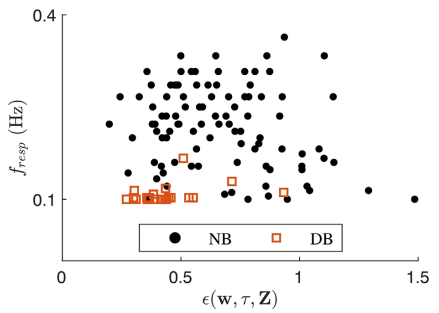

FIGURE 4
Scatter plot showing $\epsilon(\mathbf{w},\tau,\mathbf{Z})$ over $\hat{f}_{resp}$ for each 1-min segment during normal breathing (NB) and deep breathing (DB).

respiration-induced autonomic modulation a_{resp} is high during normal breathing and low during deep breathing in this example, a general conclusion about the a_{resp} values of the clinical signals can not be drawn from this comparison and is not intended. When emulating lead-specific EDR signals and adding Gaussian noise with standard deviation η, the simulated data showed a strong correlation between η and ϵ ($r = 0.89$, $p < 10^{-5}$). The examples in Figure 3 are representative of this correlation with the η and ϵ listed in Table 4, where $\mathcal{X}^{Sim}_{Resp}$ in Figure 3D was generated with a higher η and showed a higher ϵ compared to $\mathcal{X}^{Sim}_{Resp}$ in Figure 3H.

3.3 Accuracy of convolutional neural network

All CNNs $\mathcal{C}_{RR}$, $\mathcal{C}_{Resp}$, $\mathcal{C}_{AFR}$, $\mathcal{C}_{RR,Resp}$, $\mathcal{C}_{RR,AFR}$, $\mathcal{C}_{Resp,AFR}$ and $\mathcal{C}_{RR,Resp,AFR}$, described in Section 2.4.2 and trained according to Section 2.4.3, were tested using $\boldsymbol{\mathcal{X}}^{Sim,Test}$ described in Section 2.3.2. The resulting distribution of estimated $\hat{a}_{resp}$ over true a_{resp} for $\mathcal{C}_{RR,Resp,AFR}$ is shown in Figure 5. Also displayed in Figure 5 for comparison is the corresponding distribution for estimation using linear regression $\mathcal{L}_{RR,Resp,AFR}$ based on the same data $\boldsymbol{\mathcal{X}} = [\mathcal{X}^{Sim}_{RR}; \mathcal{X}^{Sim}_{Resp}; \mathcal{X}^{Sim}_{AFR}]$. The RMSE, Pearson sample correlation and R^2 are listed for the seven CNN versions and $\mathcal{L}_{RR,Resp,AFR}$ in Table 5. The $\mathcal{C}_{RR,Resp,AFR}$ resulted in the lowest RMSE and highest correlation and R^2. The CNNs $\mathcal{C}_{AFR}$, $\mathcal{C}_{Resp}$ and $\mathcal{C}_{Resp,AFR}$ without RR series in the input data performed poorly. The $\mathcal{C}_{RR}$ estimated $\hat{a}_{resp}$ with an RMSE of 0.074, where the addition of $\mathcal{X}^{Sim}_{Resp}$ or $\mathcal{X}^{Sim}_{AFR}$ to the input improved the accuracy of the $\hat{a}_{resp}$ estimation slightly.

For $\mathcal{C}_{RR}$, $\mathcal{C}_{RR,AFR}$, $\mathcal{C}_{RR,Resp}$ and $\mathcal{C}_{RR,Resp,AFR}$, the local RMSE of $\hat{a}_{resp}$ for specific f'_{resp} and ϵ' were computed according to Section 2.4.4 and illustrated in Figure 6. It can be seen in all four contour plots that the RMSE is dependent on f'_{resp} and ϵ'. The CNNs produce more accurate estimations for data with a high f'_{resp} and low ϵ', however, the RMSE is more sensitive to changes in f'_{resp}. Adding $\mathcal{X}^{Sim}_{AFR}$ to the input improves the RMSE for all values of f'_{resp} and ϵ. While the addition of $\mathcal{X}^{Sim}_{Resp}$ to the input improves the RMSE for most f'_{resp} and ϵ', it worsens the RMSE for high ϵ' and low f'_{resp} as indicated in Figure 6. Within the indicated region, the accuracy of $\hat{a}_{resp}$ is higher without $\mathcal{X}^{Sim}_{Resp}$ in the input data.

The accuracy of the CNN improves with longer input data, indicated by the fact that the RMSE of $\mathcal{C}^{2.5min}_{RR,Resp,AFR}$ was 0.050. The RMSE, Pearson sample correlation and R^2 is listed for $\mathcal{C}^{2.5min}_{RR,Resp,AFR}$ in Table 5. The RMSE improved for all values of ϵ' and f'_{resp}, whereas the local RMSE improved especially at lower f'_{resp} (data not shown).

3.4 Estimation of respiration-induced autonomic modulation in clinical data

The CNN $\mathcal{C}_{RR,Resp,AFR}$ was used to obtain $\hat{a}_{resp}$ from the clinical ECG-derived features in $\boldsymbol{\mathcal{X}} = [\mathcal{X}^{Clin}_{RR}; \mathcal{X}^{Clin}_{Resp}; \mathcal{X}^{Clin}_{AFR}]$. The resulting $\hat{a}_{resp}$ for 1-min segments during normal breathing and deep breathing are shown in Figure 7. There was high interpatient variability in $\hat{a}_{resp}$ in the study population and no clear relation was found between $\hat{a}_{resp}$ during normal breathing and deep breathing. No significant correlation was found between a change in respiration frequency $\hat{f}^{DB}_{resp} - \hat{f}^{NB}_{resp}$ and a change in respiration-induced autonomic modulation $\hat{a}^{DB}_{resp} - \hat{a}^{NB}_{resp}$.

The vertical lines around $\hat{a}_{resp}$ in Figure 7A correspond to $\pm\sigma(f_{resp},\epsilon)$, described in Section 2.4.4 and is used for the Monte Carlo sampling described in Section 2.4.5. For 20 subjects, $\hat{a}_{resp}$ was available for at least one segment during normal breathing and one segment during deep breathing (cf. exclusion criteria in Section 2.2.5). For those 20 subjects, Monte Carlo sampling was used to investigate whether $\hat{a}_{resp}$ is larger during deep breathing than during normal breathing as described in Section 2.4.5. As illustrated

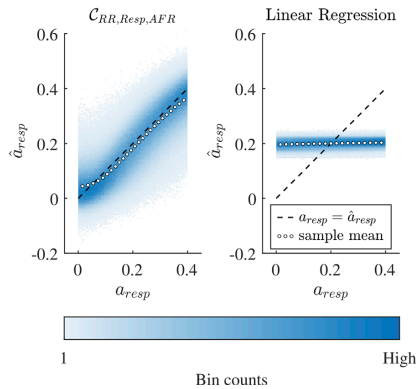

FIGURE 5
Binned scatter plot of estimated $\hat{a}_{resp}$ versus true a_{resp} for the CNN $\mathcal{C}_{RR,Resp,AFR}$ and linear regression $\mathcal{L}_{RR,Resp,AFR}$, where both were based on the same input data $\boldsymbol{\mathcal{X}} = [\mathcal{X}_{RR}^{Sim}; \mathcal{X}_{Resp}^{Sim}; \mathcal{X}_{AFR}^{Sim}]$. The black dotted line shows where $\hat{a}_{resp}$ is equal to a_{resp}. The white dotted line shows the sample mean of the $\hat{a}_{resp}$ estimation.

TABLE 5 RMSE, Pearson sample correlation and R^2 of the seven CNN versions and linear regression $\mathcal{L}_{RR,Resp,AFR}$ using 1-min segments, and $\mathcal{C}_{RR,Resp,AFR}^{2.5min}$ using 2.5-min segments.

	RMSE	Pearson correlation r	R^2
$\mathcal{C}_{RR,Resp,AFR}^{2.5min}$	0.050	0.923	0.816
$\mathcal{C}_{RR,Resp,AFR}$	0.066	0.855	0.674
$\mathcal{C}_{RR,Resp}$	0.070	0.830	0.636
$\mathcal{C}_{RR,AFR}$	0.070	0.837	0.630
$\mathcal{C}_{RR}$	0.074	0.805	0.585
$\mathcal{C}_{Resp,AFR}$	0.098	0.583	0.284
$\mathcal{C}_{Resp}$	0.101	0.513	0.231
$\mathcal{C}_{AFR}$	0.115	0.073	0.001
$\mathcal{L}_{RR,Resp,AFR}$	0.119	0.037	−0.068

in Figure 7B: it was most likely for 5 patients that the highest a_{resp} was achieved for deep breathing; it was most likely for 5 patients that the lowest a_{resp} was achieved for deep breathing; and it was most likely for 10 patients that neither the highest nor lowest a_{resp} corresponded to deep breathing.

4 Discussion

To address the need for assessing autonomic dysfunction in patients with persistent AF, we developed a method to extract respiration-induced autonomic modulation in the AV node conduction properties from ECG data in AF. We focused on respiration-induced autonomic modulation because respiration is always present, respiration can be extracted from ECG signals, and abnormal respiration-induced autonomic modulation is often an early sign of autonomic dysfunction (Bernardi et al., 2001). To achieve this we extended our AV node model (Plappert et al., 2022) to account for respiration-induced autonomic modulation by including a time-varying scaling factor in the formulations of the AV nodal refractory period and conduction delay. We trained a 1D-CNN on simulated 1-min segments of RR series, respiration signals, and mean arrival rate of atrial impulses which replicate clinical data to estimate the peak-to-peak amplitude of respiration-induced autonomic modulation a_{resp}. We evaluated the network on simulated data and the results indicated that a_{resp} can be estimated with an RMSE of 0.066, corresponding to a sixth of the expected range for a_{resp} between 0 and 0.4. Previous studies indicate that AF progression is linked to impaired baroreflex sensitivity (van den Berg et al., 2001; Field et al., 2016; Miyoshi et al., 2020; Ferreira et al., 2023; Wang et al., 2023). Additionally, in healthy subjects, the baroreflex is a major contributor to respiration-induced autonomic modulation (Piepoli et al., 1997). Together, this suggests that our proposed estimate for respiration-induced autonomic modulation, a_{resp}, holds potential as a marker for AF progression. However, further studies are needed to confirm this relationship.

Initial results from analysis of clinical ECG data from patients in AF (cf. Figure 7A) indicate that during normal breathing, $\hat{a}_{resp}$ is often consistent between consecutive 1-min segments from the same patient, and displays a systematic difference between patients, suggesting that $\hat{a}_{resp}$ is reproducible and sensitive. During controlled breathing at 0.1 Hz, $\hat{a}_{resp}$ displayed a large interpatient variability (cf. Figure 7A) and represented the most extreme value in 10 of 20 patients (cf. Figure 7B), further supporting an adequate sensitivity. However, further studies with a larger study population and repeated tests with multiple fixed respiration rates are needed to verify reproducibility and sensitivity. The respiration rate of 0.1 Hz is associated with a maximized HRV response and baroreflex sensitivity in NSR (Russo et al., 2017), and hence we expected an increase in $\hat{a}_{resp}$ during deep breathing. However, results from the Monte Carlo sampling showed that $\hat{a}_{resp}$ increased in response to deep breathing in 5 patients, decreased in 5 patients, and remained the same in 10 patients. There are several possible reasons for this, e.g., the differences in respiration rate during normal breathing (cf. Figure 4), individual variation in the cardiorespiratory system resonance frequency (Russo et al., 2017), and differences in autonomic remodeling. It should be noted that the individual differences cannot be entirely attributed to the differences in respiration rates, since there was no correlation between changes in respiration rate and changes in a_{resp}. Due to the small patient group and lack of ground truth data in this study, future work with access to ground truth data is required to investigate if there is a correlation between a_{resp} and baroreflex sensitivity, and whether a_{resp} is a diagnostic marker for autonomic dysfunction. A re-evaluation of 50% of the SCAPIS population is currently underway within the SCAPIS2 study, and the data could allow for the investigation of whether the a_{resp} estimates decrease over time in the same AF patients, which would indicate a progression in autonomic remodeling. Furthermore, the collected data could be used for

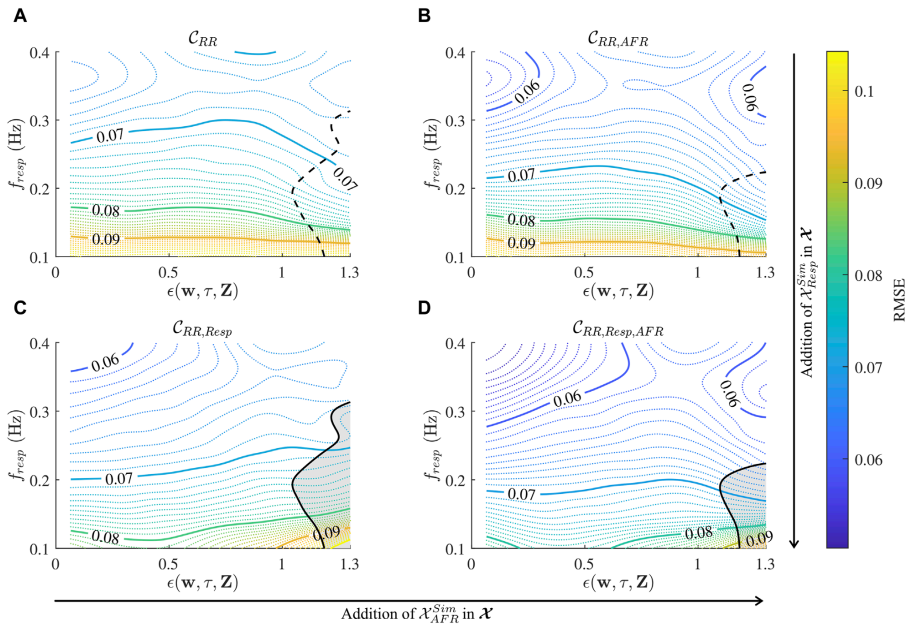

FIGURE 6
Contour plot of local RMSE estimates over a range of f_{resp}' and ϵ' for $\mathcal{C}_{RR}$ **(A)**, $\mathcal{C}_{RR,AFR}$ **(B)**, $\mathcal{C}_{RR,Resp}$ **(C)** and $\mathcal{C}_{RR,Resp,AFR}$ **(D)**. Except for the grey region, the CNNs in **(C, D)** have a higher accuracy than the CNNs in **(A,B)** respectively.

phenotyping the relation between respiration-induced autonomic modulation, autonomic dysfunction, and AF progression.

In our previous model formulation, we accounted for the autonomic modulation by introducing constant scaling factors for the refractory period and conduction delay (Plappert et al., 2022). With the scaling of AV nodal conduction properties, it was shown that the incorporation of ANS-induced changes in the model allowed better replication of several statistical properties of clinical RR series obtained from tilt tests. In the present study, this approach was further developed by using a time-varying scaling factor $A^P(t)$ to account for respiration-induced autonomic modulation in AV nodal conduction properties based on the assumption that some degree of respiration-induced autonomic modulation generally influences RR series characteristics during AF. We model respiration-induced autonomic modulation as a joint increase in AV nodal refractoriness and conduction delay in response to exhalation and a joint decrease in AV nodal refractoriness and conduction delay in response to inhalation. It is known that respiration modulates the parasympathetic activity, where inspiration decreases vagal activity and expiration increases vagal activity (Katona et al., 1970; Russo et al., 2017). Many electrophysiological (EP) studies have demonstrated that an increase in parasympathetic activity causes an increase in AV nodal conduction delay; studies in dogs reported an increased conduction delay with vagal stimulation (Irisawa et al., 1971; Spear and Moore, 1973; Martin, 1975; Nayebpour et al., 1990; Pirola and Potter, 1990; Goldberger et al., 1999) and acetylcholine administration (Priola et al., 1983). Furthermore, an increase in parasympathetic activity with vagal stimulation in dogs has been demonstrated to increase the AV nodal refractory period (Spear and Moore, 1973; Nayebpour et al., 1990; Goldberger et al., 1999). For a decrease in parasympathetic activity with atropine, EP studies demonstrate that the AV nodal conduction delay decreases in dogs (Irisawa et al., 1971) and humans (Lister et al., 1965; Akhtar et al., 1974), and the AV nodal refractory period also decreases in humans (Akhtar et al., 1974).

The assumption that some degree of respiration-induced autonomic modulation generally influences the RR series characteristics during AF is also indicated by the fact that some AF patients display clear fluctuations in their RR series matching their respiration frequency (Rawles et al., 1989; Chandler and Trewby, 1994; Nagayoshi et al., 1997). Such fluctuations could also be seen in simulated RR series for some AV node model parameter sets. During model development, we noticed that an increase in a_{resp} leads to an increase in the relative contribution of the respiration frequency in the frequency spectrum of the RR series with zero-mean $F_{RR}(f_{resp})/\Sigma_f F_{RR}(f)$ and an increase in the sample entropy of the RR series. We also noticed that an increase in f_{resp} leads to a decrease in $F_{RR}(f_{resp})/\Sigma_f F_{RR}(f)$ and an increase in the sample entropy of the RR series. When averaging over several realizations of RR series (data not shown), $F_{RR}(f_{resp})/\Sigma_f F_{RR}(f)$ could

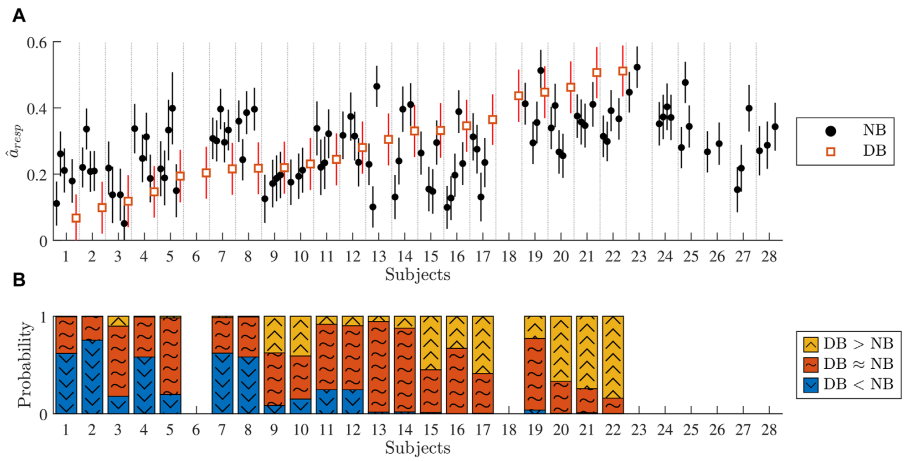

FIGURE 7
(A) Black dots correspond to the estimated $\hat{a}_{resp}$ of 1-min segments during normal breathing (NB) and red squares correspond to $\hat{a}_{resp}$ of 1-min segments during deep breathing (DB). The vertical lines correspond to $\pm\sigma(f_{resp},\epsilon)$, where the local RMSE $\sigma(f_{resp},\epsilon)$ is taken from Figure 6D. **(B)** Probabilities of a_{resp} being higher in DB than in NB (yellow, arrow-up), similar in DB and NB (red, tilde), and lower in DB than in NB (blue, arrow-down).

be clearly seen for most of the parameter sets but is usually masked in individual RR series segments by the irregularity of the RR series. Using cross-spectral analysis, no simple linear relationship has been found between respiration signal and RR series in AF patients, but a linear relationship was shown in NSR (Pitzalis et al., 1999). A possible reason for this is that the relationship between the RR series and respiration-induced autonomic modulation in AV nodal conduction properties during AF is complex and non-linear, emphasizing the need for a model-based approach. Besides some indications of fluctuations in the RR series, for most of the patients reported in (Rawles et al., 1989; Chandler and Trewby, 1994; Nagayoshi et al., 1997; Pitzalis et al., 1999; Pacchia et al., 2011) and also for the clinical data used in this study, no fluctuations in the RR series matching their respiration frequency were found. To match $F_{RR}(f_{resp})/\Sigma_f F_{RR}(f)$ in the clinical data which was always below 7%, parameter sets with a higher relative peak spectral energy were excluded from the simulated data (criterion 5 in Section 2.3.2). The RR series characteristics of the simulated data differed significantly from both the normal breathing and deep breathing data (cf. Table 3). Simulated data with RR series characteristics more similar to the clinical data could be generated by imposing stricter exclusion criteria, e.g., increasing the lower bounds for irregularity and variability set by criteria 3 and 4 in Section 2.3.2. However, the simulated data still included signals resembling the clinical data, and the wider range of characteristics likely improved the CNN training by facilitating generalization across a broader range of RR-series. Nevertheless, it is assumed that by the sheer size of the simulated datasets and the conservative model parameter ranges, there will be simulated RR series in the dataset that resemble the clinical data.

The lead-specific respiration signals were computed using the slope range method which was designed for ECG data during AF (Kontaxis et al., 2020) and found to be one of the best performing and simplest methods for lead-specific respiration signal extraction (Varon et al., 2020). The result of the lead-specific respiration signal extraction can be improved when combining respiration signals from multiple ECG leads with a joint-lead respiration signal. Previously, the principal component analysis (PCA) has been used to extract joint-lead respiration signals from the clinical data used in this study (Abdollahpur et al., 2022). However, the principal components were sensitive to high variance noise as the PCA is based on second-order statistics. To address this issue, we developed a novel approach for robust fusion of lead-specific respiration signals based on the πCA (Sameni et al., 2008). Under the assumption that the respiration signal has a periodic structure where the respiration frequency and volume between breaths are constant, the πCA is more suitable for the extraction of joint-lead respiration signals compared to other blind-source separation methods, such as the PCA and basic independent component analysis (ICA). This is because the πCA finds the linear mixture of lead-specific respiration signals with maximal periodic structure, whereas the PCA and basic ICA are based on second-order and fourth-order statistics, respectively. We assume that the respiration frequency and volume between breaths do not vary much in 1-min segments, making the πCA a suitable approach for the extraction of short joint-lead respiration signals. However, considering that the CNN $\mathcal{C}^{2.5min}_{RR,Resp,AFR}$ performs better when using 2.5-min segments instead of 1-min segments, another method may be required for the extraction of longer joint-lead respiration signals.

The comparison between the CNN $\mathcal{C}_{RR,Resp,AFR}$ and the linear regression $\mathcal{L}_{RR,Resp,AFR}$ shown in Figure 5 demonstrates that the relation between the ECG-derived features, i.e., RR series, respiration signal and mean atrial arrival rate to a_{resp} is complex

and nonlinear. The $\mathcal{L}_{RR,Resp,AFR}$ was unable to estimate a_{resp} (Pearson sample correlation $r = 0.037$) and performed clearly worse in estimating a_{resp} than the investigated CNN $\mathcal{C}_{RR,Resp,AFR}$ ($r = 0.855$). It should be noted that the purpose of this comparison is to exclude the possibility that there is a simple and linear relationship between the ECG-derived features and a_{resp}. We also investigated the performance of a Gaussian kernel support vector machine for estimating a_{resp}, representing a classical non-linear algorithm. Results were slightly better than for the linear model ($r = 0.254$, details in Supplementary Section 1), but still clearly worse than for the CNN. The advantage of the CNN over the less flexible models might be partially due to its ability to implicitly extract more complex features from the respiration signal and RR series in the early layers. While no such set of features is currently known for this problem, this leads us to speculate that some type of additional, pre-defined feature extraction step might improve the performance of also the simpler models. However, this task is far from trivial and lies outside the scope of the present study, but may nevertheless offer an interesting avenue for future work, e.g., by investigating statistical properties of the RR series based on RMS of successive RR interval differences or entropy measures.

In this study, we only investigate the performance of one basic CNN architecture. While some variations on this were tested during the neural network development, no extensive investigation has been performed and there is always the possibility that alternative architectures or algorithms may further increase the performance for the present task. For instance, a recent study suggests that combining the regression loss with a classification loss during training might improve regression results on imbalanced data (Pintea et al., 2023). The CNN described in this study requires the RR series for the estimation of a_{resp} and the mean atrial arrival rate always improved the estimation. In this evaluation, however, μ was set to the correct value; we did not account for estimation errors that are most likely present in real data since AFR provides a crude estimate of the atrial arrival rate. Moreover, the addition of the respiration signal only improves the estimation when of sufficient quality as quantified by ϵ. The linear dependence between η and ϵ supports our assumption of ϵ as a marker of respiration signal quality (cf. Section 3.2). Whereas the addition of the respiration signal and mean atrial arrival rate can improve the estimation of $\widehat{a}_{resp}$, a method based on RR series only is less sensitive to noise in the recordings. Potentially, the RR series could be extracted from pulse watch data, allowing for continuous monitoring of a_{resp} in a wide range of applications.

The performance of the CNN is dependent on f_{resp} and ϵ (cf. Figure 6), where f_{resp} appears to have a larger impact on the performance than ϵ. The marker of respiration signal quality ϵ was not used as an exclusion criterion for 1-min segments, because the addition of $\mathcal{X}^{Sim}_{Resp}$ to the input only slightly improved the accuracy of the $\widehat{a}_{resp}$ estimation and the influence of ϵ on the RMSE compared to f_{resp} was small. Instead, ϵ was used to choose the best combination of non-overlapping 1-min segments. Interestingly, the performance of the CNNs $\mathcal{C}_{RR}$, $\mathcal{C}_{AFR}$, $\mathcal{C}_{RR,AFR}$ still show a slight dependence on ϵ although this parameter quantifies the non-periodicity and signal quality of $\mathcal{X}^{Sim}_{Resp}$ (cf. Figure 6). This suggests that ϵ carries information about the RR interval series, and may indicate that the distribution of AV node model parameters varies over different ϵ and that different subsets of model parameters result in different local RMSEs. One possible explanation why the impact of f_{resp} on the performance is prominent may be that there are fewer respiratory cycles in the 1-min segment at lower f_{resp}. When using 2.5-min segments in the input data, the performance of the CNN $\mathcal{C}^{2.5min}_{RR,Resp,AFR}$ improved overall, especially at lower f_{resp}. The segment length was set to 1 min in this study due to the recording length of 1 min during deep breathing.

There are several limitations of the present study. We assume for simplicity that the variations in AV nodal refractoriness are similar to the variations in AV nodal conduction delay. We also assume that the variations in AV nodal refractoriness and conduction delay are similar between SP and FP. Moreover, the model does not include phase shifts between the RR series and respiration signal for different respiration frequencies (Angelone and Coulter, 1964), or effects of respiration volume (Grossman and Taylor, 2007). Hence, a different scaling for the refractory period and conduction delay, a different scaling for the SP and FP, a phase shift between the RR series and respiration signal, and an inclusion of respiration volume might form interesting directions for future model improvements. We did not account for respiration-induced modulation in the AA series, because the modulation is small during AF (Celotto et al., 2020; Abdollahpur et al., 2022). When choosing the bounded uniform distribution of a_{resp} for the training and testing dataset, we made a tradeoff between bias and variance. The reason why a_{resp} was randomly drawn from $\mathcal{U}[-0.1, 0.5]$ in the training data and randomly drawn from $\mathcal{U}[0, 0.4]$ in the testing data of the CNN is to reduce the bias in the $\widehat{a}_{resp}$ estimation (cf. Figure 5). Without extending the range of a_{resp} in the training data, the sample mean of the $\widehat{a}_{resp}$ diverged more from a_{resp} at values close to 0 and 0.4. However, the accuracy of the CNNs decreased by extending the range of a_{resp} in the training data. While plenty of simulated data with a_{resp} ground truth can be generated using the AV node model, there was no a_{resp} ground truth available for the clinical dataset and its size was limited. A viable approach to obtain a_{resp} ground truth may be through measurements of vagal nerve activity, which were previously collected in a large number of experimental studies, e.g., to assess the relationship to HRV during sinus rhythm in rat models (Marmerstein et al., 2021) and to assess the relationship to paroxysmal AF episodes in canine models (Tan et al., 2008). Furthermore, ultrasound-guided microneurography was proposed to obtain *in vivo* recordings from the human vagus nerve (Ottaviani et al., 2020) and results from analysis of intraneural recordings from cervical nerve in awake humans suggest that cardiac and respiration-induced autonomic modulation during normal sinus rhythm can be identified (Patros et al., 2022). Another possibility would be indirect quantification of respiration-induced autonomic modulation via acetylcholine concentration (Świt et al., 2023), but we are not aware of any procedure or method that would produce the required time resolution.

5 Conclusion

We presented an extended AV node model that accounts for respiration-induced autonomic modulation in conduction delay and refractory period. We trained a 1D-CNN to estimate the respiration-induced autonomic modulation in the AV node with simulated RR series, respiration signal, and mean atrial arrival rate which

replicates clinical ECG-derived data. Using simulated data, we demonstrated that the respiration-induced autonomic modulation can be estimated using the 1D-CNN from RR series alone and that the estimation is improved when adding a respiration signal and AFR. Initial results from analysis of ECG data from 20 patients performing a deep breathing task suggest that our proposed estimate of respiration-induced autonomic modulation a_{resp}, is reproducible and sufficiently sensitive to monitor changes and to detect individual differences. A reduced estimate of a_{resp} may possibly indicate some degree of autonomic dysfunction. However, further studies are needed to verify the reproducibility, sensitivity, and clinical significance of a_{resp}.

Data availability statement

The datasets presented in this article are not readily available because they are owned by SCAPIS. Requests to access the datasets should be directed to info@scapis.org (www.scapis.org/data-access/). The code for the model together with a user example can be found at https://github.com/PlappertF/ECG-based_estimation_of_respiration-induced_autonomic_modulation_of_AV_nodal_conduction_ during_AF.

Ethics statement

The studies involving humans were approved by the ethics committee at Lund University (2016/1031). The studies were conducted in accordance with the local legislation and institutional requirements. The participants provided their written informed consent to participate in this study.

Author contributions

FP: Conceptualization, Data curation, Formal Analysis, Investigation, Methodology, Software, Validation, Visualization, Writing–original draft, Writing–review and editing. GE: Writing–review and editing, Data curation. PP: Writing–review and editing, Conceptualization, Funding acquisition, Methodology. MW: Conceptualization, Funding acquisition, Methodology, Writing–review and editing, Formal Analysis, Investigation, Project administration, Supervision, Validation, Writing–original draft. FS: Conceptualization, Formal Analysis, Funding acquisition, Investigation, Methodology, Project administration, Resources, Supervision, Validation, Writing–original draft, Writing–review and editing.

Funding

The author(s) declare that financial support was received for the research, authorship, and/or publication of this article. The research was supported by the Swedish Research Council (grant VR 2019–04272), the Crafoord Foundation (grant 20200605), and the Swedish Heart-Lung foundation (no 2020-0173). The computations were enabled by resources provided by the National Academic Infrastructure for Supercomputing in Sweden (NAISS) and the Swedish National Infrastructure for Computing (SNIC) at Lund University partially funded by the Swedish Research Council through grant agreements no. 2022-06725 and no. 2018-05973. The Swedish Heart and Lung foundation was the main funding body of the SCAPIS cohort. SCAPIS was also supported by grants from the Knut and Alice Wallenberg Foundation, the Swedish Research Council, and Sweden's Innovation agency.

Conflict of interest

The authors declare that the research was conducted in the absence of any commercial or financial relationships that could be construed as a potential conflict of interest.

Publisher's note

Supplementary material

The Supplementary Material for this article can be found online at: https://www.frontiersin.org/articles/10.3389/fphys.2024.1281343/full#supplementary-material

References

Abdollahpur, M., Engström, G., Platonov, P. G., and Sandberg, F. (2022). A subspace projection approach to quantify respiratory variations in the f-wave frequency trend. *Front. Physiol.* 13, 976925. doi:10.3389/fphys.2022.976925

Akhtar, M., Damato, A. N., Caracta, A. R., Batsford, W. P., Josephson, M. E., and Lau, S. H. (1974). Electrophysiologic effects of atropine on atrioventricular conduction studied by his bundle electrogram. *Am. J. Cardiol.* 33, 333–343. doi:10.1016/0002-9149(74)90313-0

Angelone, A., and Coulter, N. A. (1964). Respiratory sinus arrhythmia: a frequency dependent phenomenon. *J. Appl. Physiol.* 19, 479–482. doi:10.1152/jappl.1964.19.3.479

Bergström, G., Berglund, G., Blomberg, A., Brandberg, J., Engström, G., Engvall, J., et al. (2015). The Swedish CArdioPulmonary BioImage Study: objectives and design. *J. Intern. Med.* 278, 645–659. doi:10.1111/joim.12384

Bernardi, L., Porta, C., Gabutti, A., Spicuzza, L., and Sleight, P. (2001). Modulatory effects of respiration. *Auton. Neurosci.* 90, 47–56. doi:10.1016/S1566-0702(01)00267-3

Billette, J., and Tadros, R. (2019). An integrated overview of AV node physiology. *Pacing Clin. Electrophysiol.* 42, 805–820. doi:10.1111/pace.13734

Celotto, C., Sánchez, C., Mountris, K. A., Abdollahpur, M., Sandberg, F., Laguna, P., et al. (2020). Relationship between atrial oscillatory acetylcholine release pattern

and f-wave frequency modulation: a computational and experimental study. *Comput. Cardiol.*, 1–4. doi:10.22489/CinC.2020.303

Chandler, S. T., and Trewby, P. N. (1994). Is respiratory sinus arrhythmia present in atrial fibrillation? a study using two quantitative methods. *Med. Eng. Phys.* 16, 334–337. doi:10.1016/1350-4533(94)90061-2

Climent, A. M., Atienza, F., Millet, J., and Guillem, M. S. (2011a). Generation of realistic atrial to atrial interval series during atrial fibrillation. *Med. Biol. Eng. Comput.* 49, 1261–1268. doi:10.1007/s11517-011-0823-2

Climent, A. M., Guillem, M. S., Zhang, Y., Millet, J., and Mazgalev, T. N. (2011b). Functional mathematical model of dual pathway AV nodal conduction. *Am. J. Physiol. Heart Circ. Physiol.* 300, 1393–1401. doi:10.1152/ajpheart.01175.2010

Cohen, R. J., Berger, R. D., and Dushane, T. E. (1983). A quantitative model for the ventricular response during atrial fibrillation. *IEEE Trans. Biomed. Eng.* 30, 769–781. doi:10.1109/TBME.1983.325077

Doste, R., Lozano, M., Jimenez-Perez, G., Mont, L., Berruezo, A., Penela, D., et al. (2022). Training machine learning models with synthetic data improves the prediction of ventricular origin in outflow tract ventricular arrhythmias. *Front. Physiol.* 12, 909372. doi:10.3389/fphys.2022.909372

Engström, G., Hamrefors, V., Fedorowski, A., Persson, A., Johansson, M. E., Ostenfeld, E., et al. (2022). Cardiovagal function measured by the deep breathing test: relationships with coronary atherosclerosis. *J. Am. Heart Assoc.* 11, e024053. doi:10.1161/JAHA.121.024053

Ferreira, M., Laranjo, S., Cunha, P., Geraldes, V., Oliveira, M., and Rocha, I. (2023). Orthostatic stress and baroreflex sensitivity: a window into autonomic dysfunction in lone paroxysmal atrial fibrillation. *J. Clin. Med.* 12, 5857. doi:10.3390/jcm12185857

Field, M. E., Wasmund, S. L., Page, R. L., and Hamdan, M. H. (2016). Restoring sinus rhythm improves baroreflex function in patients with persistent atrial fibrillation. *J. Am. Hear. Assoc.* 5, e002997. doi:10.1161/jaha.115.002997

George, S. A., Faye, N. R., Murillo-Berlioz, A., Lee, K. B., Trachiotis, G. D., and Efimov, I. R. (2017). At the atrioventricular crossroads: dual pathway electrophysiology in the atrioventricular node and its underlying heterogeneities. *Arrhythm. Electrophysiol. Rev.* 6, 179–185. doi:10.15420/aer.2017.30.1

Gheorghita, B. A., Itu, L. M., Sharma, P., Suciu, C., Wetzl, J., Geppert, C., et al. (2022). Improving robustness of automatic cardiac function quantification from cine magnetic resonance imaging using synthetic image data. *Sci. Rep.* 12, 2391. doi:10.1038/s41598-022-06315-3

Goldberger, J. J., Kadish, A. H., Johnson, D., and Qi, X. (1999). New technique for vagal nerve stimulation. *J. Neurosci. Methods.* 91, 109–114. doi:10.1016/S0165-0270(99)00085-0

Grossman, P., and Taylor, E. W. (2007). Toward understanding respiratory sinus arrhythmia: relations to cardiac vagal tone, evolution and biobehavioral functions. *Biol. Psychol.* 74, 263–285. doi:10.1016/j.biopsycho.2005.11.014

Hanna, P., Dacey, M. J., Brennan, J., Moss, A., Robbins, S., Achanta, S., et al. (2021). Innervation and neuronal control of the mammalian sinoatrial node a comprehensive atlas. *Circ. Res.* 128, 1279–1296. doi:10.1161/CIRCRESAHA.120.318458

Henriksson, M., Corino, V. D., Sörnmo, L., and Sandberg, F. (2016). A statistical atrioventricular node model accounting for pathway switching during atrial fibrillation. *IEEE Trans. Biomed. Eng.* 63, 1842–1849. doi:10.1109/TBME.2015.2503562

Henriksson, M., Petrėnas, A., Marozas, V., Sandberg, F., and Sörnmo, L. (2018). Model-based assessment of f-wave signal quality in patients with atrial fibrillation. *IEEE Trans. Biomed. Eng.* 65, 2600–2611. doi:10.1109/TBME.2018.2810508

Hindricks, G., Potpara, T., Dagres, N., Arbelo, E., Bax, J. J., Blomström-Lundqvist, C., et al. (2020). 2020 ESC Guidelines for the diagnosis and management of atrial fibrillation developed in collaboration with the European Association for Cardio-Thoracic Surgery (EACTS): the Task Force for the diagnosis and management of atrial fibrillation of the European Society of Cardiology (ESC) Developed with the special contribution of the European Heart Rhythm Association (EHRA) of the ESC. *Eur. Heart J.* 42, 373–498. doi:10.1093/eurheartj/ehaa612

Inada, S., Shibata, N., Iwata, M., Haraguchi, R., Ashihara, T., Ikeda, T., et al. (2017). Simulation of ventricular rate control during atrial fibrillation using ionic channel blockers. *J. Arrhythm.* 33, 302–309. doi:10.1016/j.joa.2016.12.002

Irisawa, H., Caldwell, W. M., and Wilson, M. F. (1971). Neural regulation of atrioventricular conduction. *Jpn. J. Physiol.* 21, 15–25. doi:10.2170/jjphysiol.21.15

Joglar, J. A., Chung, M. K., Armbruster, A. L., Benjamin, E. J., Chyou, J. Y., Cronin, E. M., et al. (2023). 2023 ACC/AHA/ACCP/HRS guideline for the diagnosis and management of atrial fibrillation A report of the American college of cardiology/American heart association joint committee on clinical practice guidelines. *J. Am. Coll. Cardiol.* 83, 109–279. doi:10.1016/j.jacc.2023.08.017

Kaisti, M., Laitala, J., Wong, D., and Airola, A. (2023). Domain randomization using synthetic electrocardiograms for training neural networks. *Artif. Intell. Med.* 143, 102583. doi:10.1016/j.artmed.2023.102583

Karlsson, M., Sandberg, F., Ulimoen, S. R., and Wallman, M. (2021). Non-invasive characterization of human AV-Nodal conduction delay and refractory period during atrial fibrillation. *Front. Physiol.* 12, 728955. doi:10.3389/fphys.2021.728955

Katona, P. G., Poitras, J. W., Barnett, G. O., and Terry, B. S. (1970). Cardiac vagal efferent activity and heart period in the carotid sinus reflex. *Am. J. Physiol.* 218, 1030–1037. doi:10.1152/ajplegacy.1970.218.4.1030

Kontaxis, S., Lázaro, J., Corino, V. D., Sandberg, F., Bailón, R., Laguna, P., et al. (2020). ECG-derived respiratory rate in atrial fibrillation. *IEEE Trans. Biomed. Eng.* 67, 905–914. doi:10.1109/TBME.2019.2923587

Lian, J., Müssig, D., and Lang, V. (2006). Computer modeling of ventricular rhythm during atrial fibrillation and ventricular pacing. *IEEE Trans. Biomed. Eng.* 53, 1512–1520. doi:10.1109/TBME.2006.876627

Linz, D., Elliott, A. D., Hohl, M., Malik, V., Schotten, U., Dobrev, D., et al. (2019). Role of autonomic nervous system in atrial fibrillation. *Int. J. Cardiol.* 287, 181–188. doi:10.1016/j.ijcard.2018.11.091

Lister, J. W., Stein, E., Kosowsky, B. D., Lau, S. H., and Damato, A. N. (1965). Atrioventricular conduction in man: effect of rate, exercise, isoproterenol and atropine on the P-R interval. *Am. J. Cardiol.* 16, 516–523. doi:10.1016/0002-9149(65)90028-7

Loecher, M., Perotti, L. E., and Ennis, D. B. (2021). Using synthetic data generation to train a cardiac motion tag tracking neural network. *Med. Image Anal.* 74, 102223. doi:10.1016/j.media.2021.102223

Malik, V., Elliott, A. D., Thomas, G., Mishima, R. S., Pitman, B., Middeldorp, M. E., et al. (2022). Autonomic afferent dysregulation in atrial fibrillation. *JACC Clin. Electrophysiol.* 8, 152–164. doi:10.1016/j.jacep.2021.10.010

Mangin, L., Vinet, A., Pagé, P., and Glass, L. (2005). Effects of antiarrhythmic drug therapy on atrioventricular nodal function during atrial fibrillation in humans. *Europace* 7, S71–S82. doi:10.1016/j.eupc.2005.03.016

Marmerstein, J. T., McCallum, G. A., and Durand, D. M. (2021). Direct measurement of vagal tone in rats does not show correlation to HRV. *Sci. Rep.* 11, 1210. doi:10.1038/s41598-020-79808-8

Martin, P. (1975). Dynamic vagal control of atrial-ventricular condition: theoretical and experimental studies. *Ann. Biomed. Eng.* 3, 275–295. doi:10.1007/BF02390973

Masè, M., Marini, M., Disertori, M., and Ravelli, F. (2015). Dynamics of AV coupling during human atrial fibrillation: role of atrial rate. *Am. J. Physiol. Heart Circ. Physiol.* 309, H198–H205. doi:10.1152/ajpheart.00726.2014

Miyoshi, M., Kondo, H., Ishii, Y., Shinohara, T., Yonezu, K., Harada, T., et al. (2020). Baroreflex sensitivity in patients with atrial fibrillation. *J. Am. Hear. Assoc.* 9, e018019. doi:10.1161/jaha.120.018019

Nagayoshi, H., Janota, T., Hnatkova, K., Camm, A. J., and Malik, M. (1997). Autonomic modulation of ventricular rate in atrial fibrillation. *Am. J. Physiol. Heart Circ. Physiol.* 272, H1643–H1649. doi:10.1152/ajpheart.1997.272.4.H1643

Nayebpour, M., Talajic, M., Villemaire, C., and Nattel, S. (1990). Vagal modulation of the rate-dependent properties of the atrioventricular node. *Circ. Res.* 67, 1152–1166. doi:10.1161/01.RES.67.5.1152

Ottaviani, M. M., Wright, L., Dawood, T., and Macefield, V. G. (2020). *In vivo* recordings from the human vagus nerve using ultrasound-guided microneurography. *J. Physiol.* 598, 3569–3576. doi:10.1113/JP280077

Pacchia, C. F., Kline, G. P., Hamdan, M. H., Clark, K. G., Clark, M. G., and Smith, M. L. (2011). Oscillatory vagal maneuvers produce ventricular entrainment in patients with atrial fibrillation. *Clin. Auton. Res.* 21, 325–332. doi:10.1007/s10286-011-0117-7

Patros, M., Ottaviani, M. M., Wright, L., Dawood, T., and Macefield, V. G. (2022). Quantification of cardiac and respiratory modulation of axonal activity in the human vagus nerve. *J. Physiol.* 600, 3113–3126. doi:10.1113/JP282994

Piepoli, M., Sleight, P., Leuzzi, S., Valle, F., Spadacini, G., Passino, C., et al. (1997). Origin of respiratory sinus arrhythmia in conscious humans. An important role for arterial carotid baroreceptors. *Circ* 95, 1813–1821. doi:10.1161/01.CIR.95.7.1813

Pintea, S. L., Lin, Y., Dijkstra, J., and van Gemert, J. C. (2023). A step towards understanding why classification helps regression. *2023 IEEE/CVF Int. Conf. Comput. Vis. (ICCV)*, 19915–19924. doi:10.1109/ICCV51070.2023.01828

Pirola, F. T., and Potter, E. K. (1990). Vagal action on atrioventricular conduction and its inhibition by sympathetic stimulation and neuropeptide Y in anaesthetised dogs. *J. Auton. Nerv. Syst.* 31, 1–12. doi:10.1016/0165-1838(90)90166-g

Pitzalis, M. V., Massari, F., Forleo, C., Fioretti, A., Colombo, R., Balducci, C., et al. (1999). Respiratory systolic pressure variability during atrial fibrillation and sinus rhythm. *Hypertension* 34, 1060–1065. doi:10.1161/01.HYP.34.5.1060

Plappert, F., Wallman, M., Abdollahpur, M., Platonov, P. G., Östenson, S., and Sandberg, F. (2022). An atrioventricular node model incorporating autonomic tone. *Front. Physiol.* 13, 976468. doi:10.3389/fphys.2022.976468

Priola, D. V., Curtis, M. B., Anagnostelis, C., and Martinez, E. (1983). Altered nicotinic sensitivity of AV node in surgically denervated canine hearts. *Am. J. Physiol.* 245, 27–32. doi:10.1152/ajpheart.1983.245.1.H27

Rashidi, A., and Khodarahmi, I. (2005). Nonlinear modeling of the atrioventricular node physiology in atrial fibrillation. *J. Theor. Biol.* 232, 545–549. doi:10.1016/j.jtbi.2004.08.033

Rawles, J. M., Pai, G. R., and Reid, S. R. (1989). Paradoxical effect of respiration on ventricular rate in atrial fibrillation. *Clin. Sci.* 76, 109–112. doi:10.1042/cs0760109

Russo, M. A., Santarelli, D. M., and O'Rourke, D. (2017). The physiological effects of slow breathing in the healthy human. *Breathe (Sheff)* 13, 298–309. doi:10.1183/20734735.009817

Sameni, R., Jutten, C., and Shamsollahi, M. B. (2008). Multichannel electrocardiogram decomposition using periodic component analysis. *IEEE Trans. Biomed. Eng.* 55, 1935–1940. doi:10.1109/TBME.2008.919714

Sassi, R., Cerutti, S., Lombardi, F., Malik, M., Huikuri, H. V., Peng, C.-K., et al. (2015). Advances in heart rate variability signal analysis: joint position statement by the e-cardiology ESC working group and the European heart rhythm association co-endorsed by the asia pacific heart rhythm society. *Europace* 17, 1341–1353. doi:10.1093/europace/euv015

Shaffer, F., and Ginsberg, J. P. (2017). An overview of heart rate variability metrics and norms. *Front. Public Health* 5, 258. doi:10.3389/fpubh.2017.00258

Shen, M. J., and Zipes, D. P. (2014). Role of the autonomic nervous system in modulating cardiac arrhythmias. *Circ. Res.* 114, 1004–1021. doi:10.1161/CIRCRESAHA.113.302549

Smith, L. N. (2017). Cyclical learning rates for training neural networks. *2017 IEEE Winter Conf. Appl. Comput. Vis. (WACV)*, 464–472. doi:10.1109/WACV.2017.58

Sološenko, A., Paliakaitė, B., Marozas, V., and Sörnmo, L. (2022). Training convolutional neural networks on simulated photoplethysmography data: application to bradycardia and tachycardia detection. *Front. Physiol.* 13, 928098. doi:10.3389/fphys.2022.928098

Spear, J. F., and Moore, E. N. (1973). Influence of brief vagal and stellate nerve stimulation on pacemaker activity and conduction within the atrioventricular conduction system of the dog. *Circ. Res.* 32, 27–41. doi:10.1161/01.RES.32.1.27

Stridh, M., and Sörnmo, L. (2001). Spatiotemporal QRST cancellation techniques for analysis of atrial fibrillation. *Ieee. Trans. Biomed. Eng.* 48, 105–111. doi:10.1109/10.900266

Świt, P., Pollap, A., and Orzeł, J. (2023). Spectroscopic determination of acetylcholine (ACh): a representative review. *Top. Curr. Chem.* 381, 16. doi:10.1007/s41061-023-00426-9

Tan, A. Y., Zhou, S., Ogawa, M., Song, J., Chu, M., Li, H., et al. (2008). Neural mechanisms of paroxysmal atrial fibrillation and paroxysmal atrial tachycardia in ambulatory canines. *Circ* 118, 916–925. doi:10.1161/CIRCULATIONAHA.108.776203

Trayanova, N. A., Popescu, D. M., and Shade, J. K. (2021). Machine learning in arrhythmia and electrophysiology. *Circ. Res.* 128, 544–566. doi:10.1161/CIRCRESAHA.120.317872

van den Berg, M. P., Hassink, R. J., Tuinenburg, A. E., van Sonderen, E. F. L. P., Lefrandt, J. D., de Kam, P. J., et al. (2001). Quality of life in patients with paroxysmal atrial fibrillation and its predictors: importance of the autonomic nervous system. *Eur. Hear. J.* 22, 247–253. doi:10.1053/euhj.2001.2180

Varon, C., Morales, J., Lázaro, J., Orini, M., Deviaene, M., Kontaxis, S., et al. (2020). A comparative study of ECG-derived respiration in ambulatory monitoring using the single-lead ECG. *Sci. Rep.* 10, 5704. doi:10.1038/s41598-020-62624-5

Wallman, M., and Sandberg, F. (2018). Characterisation of human AV-nodal properties using a network model. *Med. Biol. Eng. Comput.* 56, 247–259. doi:10.1007/s11517-017-1684-0

Wang, D., Veltmann, C., Bauersachs, J., and Duncker, D. (2023). Antiarrhythmic effects of baroreceptor activation therapy in chronic heart failure: a case report. *Eur. Hear. J. - Case Rep.* 7, ytad520. doi:10.1093/ehjcr/ytad520

Wasmund, S. L., Li, J.-M., Page, R. L., Joglar, J. A., Kowal, R. C., Smith, M. L., et al. (2003). Effect of atrial fibrillation and an irregular ventricular response on sympathetic nerve activity in human subjects. *Circ* 107, 2011–2015. doi:10.1161/01.cir.0000064900.76674.cc

Weine, J., van Gorkum, R. J., Stoeck, C. T., Vishnevskiy, V., and Kozerke, S. (2022). Synthetically trained convolutional neural networks for improved tensor estimation from free-breathing cardiac DTI. *Comput. Med. Imaging Graph.* 99, 102075. doi:10.1016/j.compmedimag.2022.102075

Yu, Y., Wei, C., Liu, L., Lian, A. L., Qu, X. F., and Yu, G. (2014). Atrial fibrillation increases sympathetic and parasympathetic neurons in the intrinsic cardiac nervous system. *Pacing Clin. Electrophysiol.* 37, 1462–1469. doi:10.1111/pace.12450

Paper III

A computational model to study hemodynamics during atrial fibrillation.
Felix Plappert, Pim JA Oomen, Clara E Jones, Emmanouil Charitakis, Lars O Karlsson, Pyotr G Platonov, Mikael Wallman, Frida Sandberg
Manuscript

A COMPUTATIONAL MODEL TO STUDY HEMODYNAMICS DURING ATRIAL FIBRILLATION

MANUSCRIPT

Felix Plappert[1⋆], **Pim J.A. Oomen**[2,3], **Clara E. Jones**[2,3], **Emmanouil Charitakis**[4,5], **Lars O. Karlsson**[5,6], **Pyotr G. Platonov**[7], **Mikael Wallman**[8†], **Frida Sandberg**[1†]

[1]Department of Biomedical Engineering, Lund University, Lund, Sweden
[2]Department of Biomedical Engineering, University of California, Irvine, CA, USA
[3]Edwards Lifesciences Foundation Cardiovascular, University of California, Irvine, CA, USA
[4]Department of Cardiology, Karolinska University Hospital, Stockholm, Sweden
[5]Department of Cardiology, Linköping University Hospital and Linköping University, Linköping, Sweden
[6]Department of Health, Medicine and Caring Sciences, Linköping University, Linköping, Sweden
[7]Department of Cardiology, Clinical Sciences, Lund University, Lund, Sweden
[8]Fraunhofer-Chalmers Centre, Department of Systems and Data Analysis, Gothenburg, Sweden
[†]These authors share last authorship
[⋆]felix.plappert@bme.lth.se

Abstract

Atrial fibrillation (AF) is associated with reduced cardiac output, which is correlated with an increase in symptomatic burden and a decline in quality of life. Predicting the hemodynamic effects of AF remains challenging due to the complex interplay of multiple contributing mechanisms. Computational modeling offers a valuable tool for simulating hemodynamics. However, models that are both capable of replicating beat-to-beat hemodynamic variations during AF and well suited for fitting to clinical data are largely lacking. In this study, we present a computational model comprising an electrical subsystem that produces the atrial and ventricular activation times characteristic for AF and a mechanical subsystem describing the cardiovascular mechanics. The model was fitted to replicate individual hemodynamic measurements of 17 patients from the SMURF study

in normal sinus rhythm (NSR) and AF. The fitted model replicated systolic and diastolic blood pressure and intracardiac pressure measurements in both NSR and AF with an absolute simulation error below 8.1 mmHg in a large majority of simulated patients (75%). Furthermore, the fitted model replicated left atrial and left ventricular ejection fraction measurements in NSR in a large majority of simulated patients with an absolute simulation error below 8.6%. In NSR, the right ventricular diastolic pressure was consistently underestimated, whereas in AF, the right ventricular systolic pressure and mean left atrial pressure were consistently overestimated. When comparing the simulated hemodynamic trends during AF across three models of atrial contraction, a model dividing the atria into multiple patches with independent and irregular mechanical activation times best replicated atrial and ventricular pressure and volume trends during AF within physiological ranges.

Keywords computational modeling · hemodynamics · atrial fibrillation · SMURF · RR series characteristics · atrioventricular node

Open Access of this manuscript

The full manuscript will be available for open access after publication in a peer-reviewed journal.

Paper IV

Prognostic value of ECG-derived f-wave characteristics from implantable LOOP recorder: Analysis from the LOOP study.

Felix Plappert*, Søren Zöga Diederichsen*, Claus Graff, Lucas Yixi Xing, Ketil Jørgen Haugan, Søren Højberg, Derk Krieger, Axel Brandes, Lars Køber, Fredrik Holmqvist, Mikael Wallman, Frida Sandberg, Jesper Hastrup Svendsen, Pyotr G Platonov

Manuscript

PROGNOSTIC VALUE OF ECG-DERIVED F-WAVE CHARACTERISTICS FROM IMPLANTABLE LOOP RECORDER: ANALYSIS FROM THE LOOP STUDY

MANUSCRIPT

Felix Plappert[1†], **Søren Zöga Diederichsen**[2†], **Claus Graff**[3], **Lucas Yixi Xing**[2], **Ketil Jørgen Haugan**[4], **Søren Højberg**[5], **Derk Krieger**[6,7], **Axel Brandes**[8], **Lars Køber**[2,9], **Fredrik Holmqvist**[10], **Mikael Wallman**[11], **Frida Sandberg**[1], **Jesper Hastrup Svendsen**[2,9‡], **Pyotr G. Platonov**[10‡]

[1]Department of Biomedical Engineering, Lund University, Lund, Sweden
[2]Department of Cardiology, Copenhagen University Hospital – Rigshospitalet, Copenhagen, Denmark
[3]Department of Health Science and Technology, Aalborg University, Aalborg, Denmark
[4]Department of Cardiology, Copenhagen University Hospital – Zealand University Hospital Roskilde, Roskilde, Denmark
[5]Department of Cardiology, Copenhagen University Hospital – Bispebjerg and Frederiksberg, Copenhagen, Denmark
[6]Department of Neurology, Mediclinic City Hospital, Dubai, United Arabic Emirates
[7]Department of Neuroscience, Mohammed Bin Rashid University of Medicine and Health Science, Dubai, United Arabic Emirates
[8]Department of Regional Health Research, University of Southern Denmark, Esbjerg, Denmark
[9]Department of Clinical Medicine, University of Copenhagen, Copenhagen, Denmark
[10]Department of Cardiology, Clinical Sciences, Lund University, Lund, Sweden
[11]Fraunhofer-Chalmers Centre, Department of Systems and Data Analysis, Gothenburg, Sweden
[†]These authors share first authorship
[‡]These authors share last authorship
[*]felix.plappert@bme.lth.se

Abstract

Background: Atrial fibrillation (AF) is characterized by uncoordinated atrial activation and is recognized as a progressive disease requiring different management strategies at various stages. ECG-derived indices of atrial remodeling have demon-

strated predictive value in established AF. These indices include atrial fibrillatory rate (AFR), average amplitude of the f-wave envelope (Amp), and the organization index derived from the signals spectral characteristics (ExpDec). However, their utility in early-stage AF remains unexplored.

Methods: The study comprised 1 411 participants (758 men, median age 73 years) without previously documented AF who participated in the LOOP study and received implantable loop recorders (ILR) for continuous monitoring. ECG signals from detected AF episodes were analyzed using the Cardiolund AFR Tracker software to extract AFR, ExpDec, and Amp indices. Two patient subgroups were formed based on AF episodes within the first year after ILR implantation: patients with AF episodes $\geq$6 minutes (n=231) and $\geq$60 minutes (n=96). For each subgroup, a reference group was formed from patients without AF episodes meeting the respective duration threshold. AFR, Amp and ExpDec from AF episodes recorded within one year after ILR implantation were considered baseline and tested for association with the outcome during the remaining duration of follow-up. Cox regression analysis, adjusted for clinical risk factors, was used to assess the relationship between f-wave indices and total mortality (primary endpoint), cardiovascular mortality or heart failure admission (secondary endpoint), and ischemic stroke or transitory ischemic attack (secondary endpoint).

Results: In patients with AF episodes $\geq$60 minutes, lower values of AFR (<317 fpm), ExpDec (<1.25), and Amp (<97.25) were significantly associated with increased risk of total mortality (Hazard ratio (HR): 2.5, 2.8, and 2.7, respectively) and increased risk of the composite endpoint of cardiovascular mortality or heart failure (HR: 4.0, 3.7, and non-significant, respectively). In patients with AF episodes $\geq$6 minutes, higher AFR was significantly associated with increased risk of total mortality (HR: 1.7). Moreover, lower AFR but higher ExpDec and Amp values were significantly associated with increased risk of the composite endpoint of cardiovascular mortality or heart failure (HR: 2.4, 2.6, and 2.5, respectively). Importantly, none of the f-wave indices demonstrated prognostic value for the composite endpoint of ischemic stroke or transitory ischemic attack in the early stages of AF.

Conclusions: ECG-derived indices of atrial remodeling, particularly AFR, ExpDec, and Amp, demonstrate significant predictive value for total mortality and the composite endpoint of cardiovascular mortality or heart failure in patients with early-stage AF episodes, suggesting their potential utility as risk stratification tools in early AF management.

Keywords Atrial fibrillatory rate · f-wave characteristics · LOOP study

Additional Contributions

We thank Christian Kronborg, MSc, PhD (University of Southern Denmark), for participating in the studys steering committee, which designed, followed and oversaw the original study and collected the data.

Open Access of this manuscript

The full manuscript will be available for open access after publication in a peer-reviewed journal.